UCL Université catholique de Louvain

École polytechnique de Louvain (EPL)

Parametrical Study of a Hybrid Electric Vehicle's Performances According to Its Use

Authors:
Christophe Michel
Thomas Mond

Thesis Director:
Pr. Paul Fisette

Readers:
Pr. Hervé Jeanmart
Aubain Verlé

Master [120] in Mechanical and Electromechanical Engineering **2015 - 2016**

Abstract

"Hybrid vehicles are a transition before the tomorrow (electric) car." Although everyone knows more or less why, only a few could explain it rigorously, and almost nobody has already attempted to optimize one (except manufacturers who keep well their precious secrets).

This master thesis proposes a global and rather complete modeling of the principle organs of a typical hybrid electric vehicle : from the electric traction motor, and the internal combustion engine to the wheels, passing by the transmission and energy supply systems. Coupled with a multibody system simulator (performed with the *Robotran*© suite), the behaviour and the performances of such a vehicle can be characterized and one can observe their variations with respect to key parameters modifications.

Furthermore, this work is interested in the genetic optimization (with the CMA-ES) of a fully hybrid electric car according to its use. The results rejoin the intuition that an energetically economical car has to be equipped with a larger electric motor to be able to recover more energy whereas a larger internal combustion engine is preferred in sportive applications to take advantage of a smaller mass-to-power ratio.

Acknowledgements

I would like to address my very best regards to our thesis director Pr. Fisette for his contagious passion for mechanics.

My sincere thanks to the Pr. Jeanmart for accepting the task as reader but also for being a source of admiration and knowledge regarding the great subject of Energy.

And to the Pr. Dehez who took time to redirect us on the good path even though he was not at first concerned by our realization.

Furthermore, I would like especially to express my deep gratitude towards Aubain Verlé for its continuous support and great sense of the presentation.

Also to my mentor in Liège, the Pr. Duysinx for its great understanding of the automotive industry and warmest welcome.

Evidently, this work would not have been the same without the presence and help of Christophe who particularly impressed me with his quick localisation of problems in excessively complex models.

Last but not least, I would like to thank my family and friends for their support and all the great moments during those quite hard studies.

Thomas Mond

Come to the end of this thesis, I would want to express my gratitude to the academic actors who allowed us to complete this great work : Aubain Verlé, our supervisor and second reader, for his availability, his patience (especially what concerns debugging), his advice and to have kept us on the right way; Pr. Fisette, our thesis director, to have granted us the opportunity of such a project despite the numerous candidate teams and to have been so enthusiastic considering the first developments of our work; Pr. Jeanmart, to be our third reader and whose last year course and homework were very useful for the thermal engine modeling; Pr. Dehez, for his precious advice about electric propulsion.

I wish also to offer a special thank to Thomas, who pushed me further in the details, who wrote a very big part of the present report, whose experience and passion for automobiles were a great help to achieve our models, and with whom I established a productive partnership.

Finally, I acknowledge I appreciated the constant presence and support of my family, who ensured that I missed nothing during my exile in Louvain-la-Neuve, and of my roommates, who re-motivated me when I was getting tired.

Christophe Michel

Contents

List of Abbreviations

ABS	Anti-lock Braking System
A-ECMS	Adaptative ECMS
BMS	Battery Management System
CG	Centre of Gravity
CM	Centre of Mass
CMA-ES	Covariance Matrix Adaptation Evolution Strategy
dof	Degrees of Freedom
DP	Dynamic Programming
HEV	Hybrid Electric Vehicle
ECMS	Equivalent Consumption Minimization Strategy
EGR	Exhaust Gas Recirculation
emf	Eletromotive Force
EPA	US Environment Protection Agency
ESP	Electronic Stability Program
ETM	Electric Traction Motor
FPGA	Field-Programmable Gate Array
ICE	Internal Combustion Engine
IGBT	Insulated-Gate Bipolar Transistor
IM	Induction Machine
IPM	Interior Permanent Magnet
KERS	Kinetic Energy Recovery System
LSD	Limited Slip Differential
mbs	Multibody System
NEDC	New European Driving Cycle
PET	Program Execution Time
PM	Permanent Magnet
PMSM	PM Synchronous Machine
PSD	Power Split Device
PWM	Pulse Width Modulation
RMSE	Root-Mean Square Error
SOC	State Of Charge
SRM	Switched Reluctance Motor
VFS	Variable Frequency Supply
VSI	Voltage Source Inverter
VVT	Variable Valve Timing
WLTC	Worldwide harmonized Light Vehicle Test Cycle

Table 1: Commonly used abbreviations

List of Notations

a	[m/s^2]	Acceleration
A_b	[m^2]	Contact area between pad and disc brake
A_{ag}	[m^2]	ETM air-gap cylindrical surface
A_{nt}	[m^2]	ICE valve ozzle throat surface
A^*_{nt}	[m^2]	Corrected ICE valve nozzle throat surface
AR	[-]	Aspect ratio
α	[°]	Road slope
α_{air}	[m^2/s]	Air thermal diffusivity
α_{F_O}	[-]	Objective function criteria bias
b	[m]	Distance from center of gravity to front wheel
B	[m]	ICE cylinders' bore
B_{ag}	[T]	ETM air gap magnetic B-field
B_{PM}	[T]	ETM PM-induced magnetic B-field
b_{is}	[m]	ETM stator slots' inner base width
b_{ms}	[m]	ETM stator slots' outer base width
B_r	[T]	ETM PM's remanence
β	[-]	rod length / crank radius ratio
c	[m]	Distance from center of gravity to rear wheel
C	[m]	ICE cylinders' stroke
C_b	[Nm]	Braking torque
$C_{b,e}$	[Nm]	Regenerative electric braking torque
C_{bus}	[F]	DC bus capacitor
c_d	[-]	Discharge coefficient
c_{drag}	[-]	Drag compressibility
C_e	[Nm]	Electric path output torque
C_{em}	[Nm]	Electromagnetic torque
C_{etm}	[Nm]	Electric motor output torque
$C_{f,diff,\gamma}$	[Nm]	LSD's clutch pack friction torque
c_i	[m/s]	Sonic speed of gas in thermodynamic state i
C_{ice}	[Nm]	Internal combustion engine torque
C_{hev}	[Nm]	Hybrid powertrain output torque
c_p	[J/(kg · K]	Heat capacity at constant pressure
C_{sh}	[Nm]	Torque transmitted to the motor shaft
C_t	[Nm]	Thermal path output torque
c_v	[J/(kg · K]	Heat capacity at constant volume
C_w	[Nm]	Torque transmitted to the wheel axle
C_x	[-]	Aerodynamic drag coefficient
$C_{x,add}$	[-]	Aerodynamic add-on drag coefficient
C_y	[-]	Lateral aerodynamic force coefficient
C_z	[-]	Aerodynamic lift coefficient
$C_{z,add}$	[-]	Aerodynamic add-on lift coefficient
γ	[-]	Heat capacity ratio
γ_{long}	[-]	Longitudinal slip
D	[m]	Valve seat diameter
D_{aero}	[N]	Aerodynamic drag
D_m	[m]	Mean valve seat diameter
D_p	[m]	Valve port diameter
D_s	[m]	Valve stem diameter
D_v	[m]	Valve head diameter
δ	[°]	Direction of the drag (rotation according to Z axis)
ΔC_b	[Nm]	ESP additional individual wheel braking torque

Δk_b	[-]	ESP supplementary demand of braking torque
ΔE_e	[kWh/km]	Electric energy consumption
Δp_{in}	[Pa]	Pressure losses in the intake manifold
Δ_{rp}	[m]	Rack and pinion steering gear displacement
ΔV_ϕ	[l/100km]	Fuel consumption
$\delta_{w,f,l}$	[°]	Front left wheel steering angle
e_{ag}	[m]	Air gap width
E_{bat}	[J]	Electrical capacity of the battery
E_e	[J]	Electrical path energy use
e_{PM}	[m]	ETM permanent magnet thickness
e_{Osw}	[-]	Aerodynamic add-on Oswald efficiency
E_t	[J]	Thermal path energy use
E_w	[J]	Energy required at the wheels
E_0	[V]	Back-emf in stator windings
ϵ	[-]	ETM power ratio
ϵ_{sc}	[m]	Trajectory error
f_c	[-]	Fraction of smoke inside one ICE cylinder
f_e	[-]	Fraction of smoke in the exhaust manifold
f_i	[-]	Fraction of smoke in the intake manifold
F_b	[N]	Braking force
F_{lat}	[N]	Lateral wheel to ground contact force
F_{long}	[N]	Longitudinal wheel to ground contact force
F_O	[s]	Global optimization objective function
$\mathbf{F_{red}}$	[N]	Reduced matrix of the forces in the mbs
F_{vert}	[N]	Vertical wheel to ground contact force
F_x	[N]	Propulsion or traction force
g	[m/s^2]	Gravitational acceleration
ζ_w	[°]	Camber angle
H	[J/kg]	Enthalpy
$\mathbf{h}$	[various]	Constraints in the mbs
h	[m]	Centre of gravity's height
H_{ag}	[A/m]	ETM air gap magnetic H-field
H_c	[A/m]	ETM PM coercitivity
H_{PM}	[A/m]	ETM PM-induced magnetic H-field
h_{wa}	[W/(°C · m^2]	Convection coefficient between stator end winding and adjoining air
η_{box}	[-]	Gearbox transmission efficiency
η_c	[-]	Battery coulombic efficiency
η_{diff}	[-]	Differential transmission efficiency
η_{etm}	[-]	ETM's efficiency
η_{gb}	[-]	Gearbox efficiency
η_{ti}	[-]	Internal thermodynamic efficiency
θ	[°]	Crank angle
θ_b	[°]	Combustion angular duration
$\theta_{i,o}$	[°]	Inlet valve opening timing
θ_c	[°]	Inlet valve closure timing
$\theta_{e,o}$	[°]	Exhaust valve opening timing
$\theta_{e,c}$	[°]	Exhaust valve closure timing
θ_s	[°]	Ignition timing
ϑ	[-]	Unburnt coefficient
i_{diff}	[-]	Differential's reduction ratio
i_g	[-]	Gear ratio
I	[A]	Electric current intensity at the ETM
I_{bat}	[A]	Electric current intensity at the battery
I_{bus}	[A]	Electric current intensity at the DC bus
I_c	[A]	Electric current intensity in one battery cell
I_{ph}	[A]	Electric current intensity in the ETM phases
$\mathbf{J}$	[various]	Jacobian matrix of constraints in the mbs
J	[kg$_{fuel}$/s]	ECMS cost function
k	[-]	Accelerator < pedal > load

$K_{w,rad}$	[N/m]	Tire's radial stiffness
k_a	[-]	Accelerating throttle slope
k_b	[-]	Braking < pedal > load
k_e	[-]	Load distribution to the ETM
$k_{I,bb}$	[-]	Buck-boost controller proportional tuning parameter
$k_{P,bb}$	[-]	Buck-boost controller integral tuning parameter
$k_{P,psd}$	[-]	PSD controller proportional tuning parameter
k_t	[-]	Load distribution to the ICE
k_{secu}	[-]	Tuning parameter for security braking
k_{turn}	[m]	Tuning parameter regarding turn's curvature
k_v	[1/s]	Tuning parameter for approach speed of a corner
κ_{air}	[W/(°C · m]	Air thermal conductivity
κ_{Fe}	[W/(°C · m]	Electrical steel thermal conductivity
κ_{PM}	[W/(°C · m]	Thermal conductivity of the PM
κ_{rotor}	[W/(°C · m]	Rotor core thermal conductivity
κ_{shf}	[W/(°C · m]	Thermal conductivity of the ETM shaft
l	[m]	Valve lift
L	[m]	Wheelbase
L_{aero}	[N]	Aerodynamic lift
L_{av}	[m]	Normalized average distance between 2 battery charges
l_{Cu}	[m]	Coil turn's length
l_b	[m]	ETM bearings' width
L_{bb}	[H]	Buck-boost inductor
l_c	[m]	Coil turn's width
L_{dq}	[H]	ETM stator windings' inductance
L_{Fe}	[m]	Vehicle's full electric range
LHV	[J/kg]	Fuel lower heating value
L_{ovc}	[m]	Distance covered on the NEDC before maximal battery depletion
l_r	[m]	ETM rotor length
L_{rs}	[m]	Distance between roadside and vehicle's centre of mass
L_{secu}	[m]	Security distance for braking
L_{slot}	[m]	ETM stator slot perimeter
L_{stop}	[m]	Minimum stopping distance
l_t	[m]	ETM stator teeth length
λ_0	[-]	ETM magnetic flux leakage coefficient
$\mathbf{M}$	[kg]	Mass matrix of the multibody system
m	[kg]	Vehicle mass
$m_{a,1}$	[-]	Stoichiometric ratio mass of air / mass of fuel
M_{aero}	[Nm]	Aerodynamic moment
m_b	[kg]	Braking system mass
m_{bat}	[kg]	Battery pack's mass
m_c	[kg]	Mass of gas inside one ICE cylinder
m_{cell}	[kg]	Individual battery cell's mass
m_{Cu}	[kg]	Mass of the ETM's copper windings
m_{diff}	[kg]	Differential's mass
$\dot{m}_f$	[kg/s]	Mass flow
m_{gb}	[kg]	Gearbox' mass
m_{etm}	[kg]	ETM's mass
m_{ice}	[kg]	ICE total mass
M_m	[kg/mol]	Molar mass
m_{mix}	[kg]	Mass of air-fuel mixture in one ICE cylinder
m_{ph}	[-]	Number of phases in the ETM
M_{pitch}	[Nm]	Rolling resistance moment
m_{PM}	[kg]	ETM's PM's mass
$\dot{m}_r$	[kg/s]	Mass reflow
$m_{R,Fe}$	[kg]	Iron mass in the ETM rotor
M_{roll}	[Nm]	Overturning moment
$m_{S,Fe}$	[kg]	Iron mass in the ETM stator
m_{tank}	[kg]	Fuel tank instantaneous total mass

$\hat{m}_{VSI}$	[-]	VSI modulation factor
M_{yaw}	[Nm]	Aligning torque
m_ϕ	[kg]	Fuel consumption
μ_b	[-]	Pad to disc brake friction coefficient
μ_{ttg}	[-]	Tire-to-ground friction coefficient
μ_0	[N/A^2]	Air magnetic permeability
n_c	[-]	Number of turns in the stator coils
n_{cell}	[-]	Number of battery cells constituting the pack
$n_{cell,s}$	[-]	Number of cells placed in series in a branch
n_{cyl}	[-]	Number of ICE cylinders
Nu	[-]	Nusselt number
$n_\parallel$	[-]	Number of battery branches
ν_{air}	[m^2/s]	Air kinematic viscosity
ξ	[-]	Power electronics' IGBT duty ratio
p	[-]	Number of pairs of poles in the ETM
$p_{b,mc}$	[Pa]	Master cylinder pressure
p_b	[Pa]	Brake caliper piston pressure
p_c	[Pa]	Pressure inside one ICE cylinder
P_{em}	[W]	Electromagnetic power
P_{etm}	[W]	ETM output power
p_{ex}	[Pa]	Pressure at the intake manifold
P_{ice}	[W]	ICE power output
p_{in}	[Pa]	Inlet pressure
p_m	[Pa]	Motoring pressure
p_{me}	[Pa]	Mean effective pressure
p_{me}	[Pa]	Mean effective pressure
p_{mf}	[Pa]	Mean friction pressure
p_{mi}	[Pa]	Mean indicated pressure
p_{mp}	[Pa]	Mean pumping pressure
p_{nt}	[Pa]	Pressure at nozzle throat
$\underline{p_{optim}}$	[various]	Optimization parameters vector
Pr	[-]	Prandtl number
p_w	[m]	Tire penetration
p_0	[Pa]	Normal condition pressure
$\Pi_{t,max}$	[-]	ICE maximum boost ratio at low speeds
$\mathbf{Q}$	[N]	Joint forces in the mbs
Q	[J]	Thermal energy
q	[m]	Generalized coordinates of the joints in the mbs
$Q_{bat,0}$	[Ah]	Nominal capacity of the battery pack
Q_{Cu}	[W]	Copper or Joule losses
$Q_{R,Fe}$	[W]	Magnetic or iron losses at the ETM rotor
$Q_{S,Fe}$	[W]	Magnetic or iron losses at the ETM stator
Q_{WF}	[W]	Mechanical losses at the ETM stator
R	[J/(mol · K)]	Universal gas constant
r	[-]	ICE volumetric efficiency
R_i	[J/(kg · K)]	Specific gas i constant
R_b	[m]	Disc brake radius
R_{bat}	[Ω]	Overall battery resistance
R_c	[Ω]	Individual battery cell resistance
R_e	[m]	Effective radius of the wheel
R_f	[N]	Friction resistance
R_{ir}	[m]	ETM inner rotor radius
R_{is}	[m]	ETM inner stator radius
R_{ms}	[m]	ETM stator yoke radius
R_{or}	[m]	ETM outer rotor radius
R_{os}	[m]	ETM outer stator radius
R_{sh}	[m]	ETM shaft radius
R_{road}	[N]	Road resistance
R_{turn}	[m]	Turn's curvature radius

$R_{turn,f,l}$	[m]	Turn's curvature radius at the front left wheel
ρ_{Cu}	[kg/m^3]	Copper density
ρ_{Fe}	[kg/m^3]	Electrical steel density
ρ_{PM}	[kg/m^3]	PM density
ρ_0	[kg/m^3]	Air density in normal conditions
ϱ_w	[N/(m/s)]	Tire's radial damping coefficient
s	[-]	Electrical / fuel energy use equivalence ratio
S	[-]	Number of slots at the ETM stator
SOC	[%]	Battery state of charge
S_{PM}	[m^2]	ETM PM's area
S_{slot}	[m^2]	ETM stator slots' area
S_{wa}	[m^2]	Total surface of the winding external to stator
S_x	[m^2]	Vehicle's projected frontal area
S_y	[m^2]	Vehicle's projected lateral area
S_z	[m^2]	Vehicle's projected Z-axis area
σ_{Cu}	[$\Omega \cdot$ m]	Copper resistivity
σ_t	[°]	Road orientation at the target point
σ_v	[°]	Vehicle orientation
σ_w	[°]	Sideslip angle
ς	[°]	Seat angle
Ta	[-]	Taylor number
t_b	[s]	Combustion time duration
T_c	[K]	Temperature inside the cylinder
T_{case}	[°C]	ETM's case's temperature
$T_{coolant}$	[°C]	ETM's coolant's temperature
t_{diff}	[-]	Differential's friction calibration parameter
T_{ex}	[K]	Temperature in the exhaust manifold
T_{in}	[K]	Temperature in the intake manifold
t_{lap}	[s]	Lap time around the reference track
T_{PM}	[°C]	ETM PM's temperature
T_{rotor}	[°C]	ETM rotor's temperature
T_{shaft}	[°C]	ETM's shaft's temperature
T_{stator}	[°C]	ETM stator's temperature
T_{sw}	[s]	Bidirectional DC/DC converter switching period
T_w	[°C]	ETM winding's temperature
T_{wall}	[K]	ICE cylinders' walls' temperature
T_0	[K]	Normal condition temperature
τ	[-]	Volumetric ratio
τ_p	[-]	ETM pole pitch
u	[-]	Torque split ratio
u^*	[-]	Energetically optimal torque split ratio
U	[V]	Electric voltage at the ETM
U_{bat}	[V]	Electric voltage at the battery
$U_{bat,0}$	[V]	Electric nominal voltage at the battery
U_{bus}	[V]	DC bus electric voltage
U_c	[J]	ICE cylinder internal energy
U_{cell}	[V]	Electric instantaneous voltage at one battery cell
$U_{c,0}$	[V]	Electric nominal voltage at one battery cell
$U_{L_{bb}}$	[V]	Voltage drop at the buck-boost inductor
U_{ph}	[V]	Electric voltage at the ETM phases
v	[m/s]	Longitudinal speed of the vehicle
V_{BDC}	[m^3]	Bottom dead center cylinder capacity
V_c	[m^3]	Instantaneous cylinder volume
V_{cc}	[m^3]	ICE cylinder capacity
V_{Cu}	[m^3]	Copper volume in the ETM stator windings
$V_{R,Fe}$	[m^3]	Iron volume in the ETM rotor
$V_{S,Fe}$	[m^3]	Iron volume in the ETM stator
V_{TDC}	[m^3]	Top dead center cylinder capacity
V_ϕ	[m^3]	Fuel effective volume

$V_{\phi,0}$	[l]	Fuel tank capacity
ϕ	[-]	Fuel richness
ϕ_{PM}	[Wb]	Air-gap flux due to PM in the ETM
φ	[-]	Rolling resistance coefficient
W	[N]	Weight
W_m	[J]	Mechanical work
W_p	[J]	Pumping work
w	[m]	Valve seat width
w_v	[m]	Vehicle track width
X	[Ω]	Electric reactance of the ETM stator windings
$\dot{Y}_r$	[rad/s]	Vehicle's yaw rate
χ	[-]	Combustion progress
ψ_{PM}	[-]	Flux linkage of the PM flux in the stator windings
Z_{ag}	[°C/W]	Air-gap convection thermal resistance
Z_{mr}	[°C/W]	Radial conduction thermal resistance of the poles
Z_{rs}	[°C/W]	Radial conduction thermal resistance of rotor core
Z_s	[Ω]	ETM stator windings' impedance
Z_{shf}	[°C/W]	Thermal resistance of the shaft
Z_{st}	[°C/W]	Radial conduction thermal resistance of stator teeth
Z_{sy}	[°C/W]	Stator yoke radial conduction thermal resistance
Z_{wa}	[°C/W]	Thermal resistance between external windings and adjoining air
Z_{ws}	[°C/W]	Thermal resistance between windings and stator
ω_b	[rad/s]	ETM base speed
ω_e	[rad/s]	Supply frequency of the ETM phases
ω_{sh}	[rad/s]	Motor shaft speed
ω_t	[rad/s]	ICE speed
ω_w	[rad/s]	Wheel rotation speed

Table 2: Notations used in this text

An index $(x; y; z)$, $(f; r)$ or $(l; r)$ may be attributed to those notations specifying the direction of the force, if the physical quantity is measured on the front or rear axle, or to the left or right of the vehicle respectively.

List of Figures

List of Tables

General Introduction

The growing importance of the energetic question in the minds of any citizen and an ever-firmer tax pressure by the governments on the car manufacturer - a bit like society would need a scapegoat - has force the industry to engage in unprecedented energetic transition. The first step in those long-term changes, is the electric hybridization of conventional thermal powertrain.

One of the goals of this present study is to ultimately conclude about great guidelines for hybrid electric vehicle conception. Indeed, it sometimes appear as if the constructors were rushing towards something unknown, but at the end of the day, still producing the same cars.
The idea here is to consider the vehicle in its entirety: from its tires, to its aerodynamics via the whole powertrain simulation. Because it has to be noted that this a work of simulation and simulation only. Lots of hypotheses were made, and to reintegrate in a real car the values from the evaluation of a vehicle realized on a computer would simply be a shame.

However, what this master thesis strives to implement, is a methodology to globally visualize a vehicle and hopefully suiting it the best for its destined application. This is perhaps the base of all this work, considering a vehicle, and particularly a hybrid electric vehicle for its potential use.

In practice, this is achieved by what could be called "hybridization" of the models in a multibody simulation process. This work makes use of the UCL proprietary environment *Robotran*© and strives to bring to it components that were never before taken into account. This means the modeling of the whole powertrain architecture to output external forces that should propel the vehicle, of the aerodynamic efforts on the chassis, and of all the control units that are present to manage the dynamic behaviour of the car in real time.

After the construction of this simulator described in the first part of this report, the goal is to create an objective function for optimization that would realistically render the performances of the vehicle. This objective function should be "tweakable" according to the desired use for the vehicle as matter of sportiveness or fuel economy.

Finally, the simulator could be put to the test with this performances evaluation strategy, and conclusion be drawn from the results for potential advice to everyone who would want to build an hybrid electric vehicle.

Part I

Parametrized Hybrid Electric Vehicle Simulator

1 Introduction

A motor vehicle is an extensively complex system, composed by various sub-systems each with their own level of complexity: engine, gearbox, differential, suspensions... Therefore, when one envisages a detailed realistic model of an automobile, one has to understand how any of those mechanics coexist and influence each other.
Recalling the objective of parametrical optimization, a first challenge is imposed by the limits of available computing technologies. Indeed, processing capacities being finite, a truly realistic numerical simulation taking into account every single parameter of influence (i.e. an infinity) is simply inconceivable. But one can represent reality reliably by encoding the most critical variables, i.e. the ones that deeply impact the dynamic behaviour of a vehicle.
Identifying those is here achieved empirically, and falls into good common sense after thorough researches and scientific readings.
This part presents the conclusion of a wide literature review as to how efficiently simulate a hybrid electric vehicle (HEV) for quick optimization results.
Obviously, the documenting process was done keeping in mind the level of simplicity that this work strives to achieve. This leads to well defined equations that model basic but fully functioning technologies. The point here is not to simulate a current particular vehicle model in all its complexity but to understand how to globally optimize a car.

The simulator uses forward-facing modeling - taking the driver's commands as inputs - and a constant analysis of the control strategy used in simulation, with focus on actual feasibility, were carried out in order to best reflect the reality. However, it has to be recalled that it is the global approach to vehicle optimization that might, hopefully, be applicable to real-life automobiles, not the numerical values of the parameters directly taken from the simulation process.

The next step is to apprehend the whole control chain: from the driver's reactions to the road in front of him to the subsystems that output significant values for the car's behaviour. That chain basically represents the vehicle under study and is made of sub-systems briefly introduced above in this introduction. The exhibition of that "diagram of operation" makes another section in this part of the report and prefaces a more detailed model of each sub-system.

All in all, this part of the work is presented firstly as an exposition of the goals, and then as a "dive" into the automotive mechanics - through their chosen equivalent models - that allows to understand what permits to achieve those goals.

2 Powertrain Architecture

At the beginning of any work of modelization, there is a certain amount of features that require to be fixed beforehand. Indeed, the goal here is not to simulate any hybrid vehicle but to fully optimize one. This starts by drawing the boundaries to the field of optimization such as the powertrain architecture under study.

2.1 Structure Design Selection

When talking of hybrid electric powertrain structure, there are two great categories of mounting: series and parallel hybrid.

Series Hybrid

In a series architecture, typically, an internal combustion engine (ICE) acts as a prime mover for an electric generator that supplies energy to either the batteries, an electric motor or both depending on the actual amount of energy produced versus the torque demanded by the operator. As it can be understood quickly, a series architecture represents quite a long power transmission chain, with non-perfect yield at each "link". It is thus currently not often used to propel hybrid vehicles.

Parallel Hybrid

In a parallel hybrid, both types of motorization are connected to the wheels via a single or two separate shafts and so are able to propel the car in combination or independently [7]. This structure allows advanced power management strategies and is thus preferred in an automotive industry subjected to increasingly stringent regulation about energy efficiency.
From that point, lots of combinations are possible, allowing various driving modes such as fully thermal, electric or combined propulsion. In general, those combinations are carried out via torque coupling, but some models such as the hybrid electric Toyota Prius make use of planetary gears, linked to both different motors and to the output shaft, for speed coupling.

Moreover, though it may not be advantageous compared to the possibilities a hybrid powertrain offers today, plug-in solutions have been dismissed as this work strives to consider one unique type of HEV for diverse conceivable applications. These even include racetrack competition where pit stops does not allow quick battery supercharge. The electrical path must thus here be what is called self-sustainable, i.e. it must recharge its storage system by internal control.

Considering all these conditions and possibilities, the architecture chosen for the purpose of this work is a parallel single shaft hybrid stucture such as the one described in Figure 1.

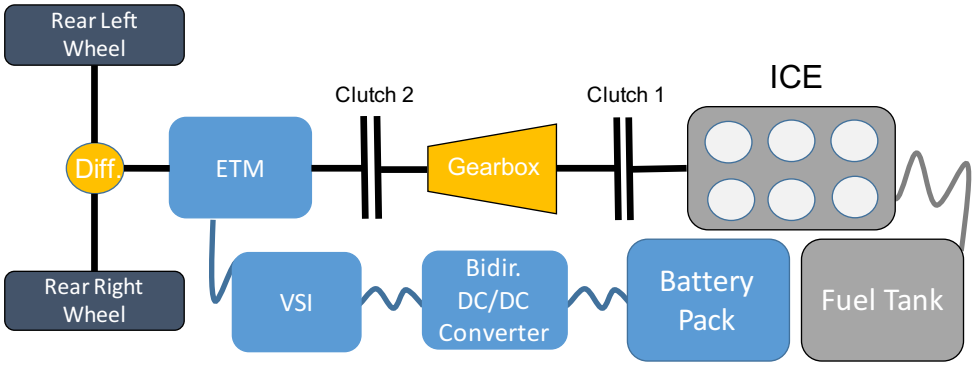

Figure 1: Powertrain architecture under study

The schematics shows only systems that are supposed to influence the power management of the structure. What is designated here by "ETM" is in fact the electric traction motor, i.e. an electromechanical converter that can be operated as a motor as well as a generator.

A colour code is used following the type of energy conversion happening in the various systems. Yellow concerns pure mechanical transmission through gear assembly. As it will be explained further, a simple model of the battery does not take into account chemical reaction taking place into each cell. The converter thus exchanges pure electrical quantities with the battery pack, through power electronics such as a voltage source inverter (VSI) and a bidirectional (bidir.) DC/DC converter, all depicted in blue. Grey is for the internal combustion engine "consuming" gasoline from a fuel tank reserve.

2.2 Practical advantages

More than being a relatively simple power transmission chain, this architecture has also been chosen for its practical advantages.
Firstly, the addition of of a second mechanical clutches offers opportunities for the three types of propulsion. Indeed, the well-thought arrangement of the systems allows the electric drive to not suffer the mechanical losses of the 6-speed gearbox.

Current technologies and particularly variable frequency supply (VFS) permit electric traction motor (ETM) to be operated on a rather large band of rotation speed. In electric mode, a gearbox is thus no longer required for the vehicle to cruise from zero to its maximum speed. On the other side, such mechanism is still needed for the ICE operation as its bandwidth is limited by the volumetric efficiency at high speed [8]. To use part of the electrical work in order to rotate the gearbox when it is not necessary would then be a shame, so a second clutch is introduced to isolate the electric machine.

Moreover, ETM have been lately proven to be particularly adequate for automobile traction. If well dimensioned, they provide high starting torque which stays constant at low speed. Above rated speed, the control strategy transits from constant torque to constant, near maximal power operation (see section 8). This vastly coincides with current driving habits allowing quick acceleration from low speeds and less power for extra-urban cruising for instance. Synchronizing motor rotation speed on the wheels through a constant differential ratio should thus be a viable solution.

In thermal propulsion nevertheless, a fuel conversion (into electrical recovery) strategy can be imagined in order to drive the ICE on its optimal operating points. The objective is that, as long as those operating points produce more output torque than demanded by the operator, the positive difference can be used to recover electrical energy by rotating the electromechanical converter in generator mode.

Finally, the advantages of introducing power electronics managing electrical exchanges between the battery and the converter are discussed in section 10.

3 Vehicle Model

This chapter provides a first introduction to the quantities that impacts vehicle dynamic performances, and to the automotive technologies that influence those quantities. For example, after a simple kinematic equilibrium, a propulsion force appears necessary to vanquish the road load; the powertrain's role is to produce that force. How it is achieved in practice is the subject of the next chapters.

3.1 2-D Kinematic Equilibrium

The simplest way to contemplate a vehicle is to model it as a road load. This is achieved by putting it in a dynamic equilibrium state as seen on Figure 3. The figure shows any forces and moments applied on the vehicle and thus that it has to counter in order to carry on forward.

The inertial reference frame $OXYZ$ is the one of the vehicle, with origin at its centre of mass (CM) , as usually in automotive engineering (see Figure 2).

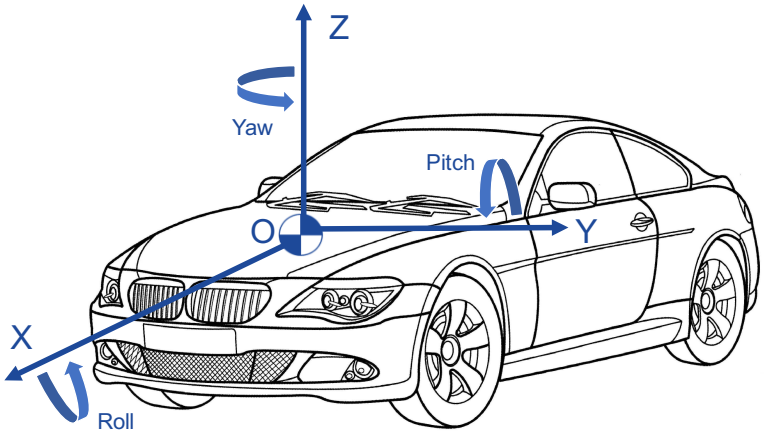

Figure 2: ISO/DIN reference frame

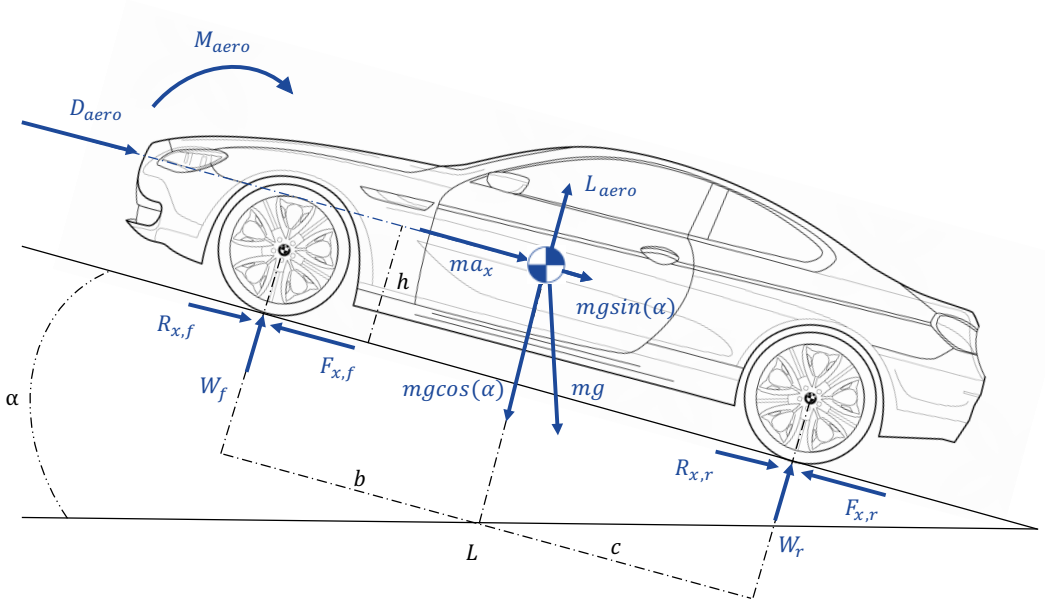

Figure 3: Forces and moments that undergoes a vehicle in dynamic equilibrium

Being methodic in the inventory of the forces and moments on Figure 3, it becomes easy to compute the dynamic equilibrium; equalizing forces and moments that have opposite orientation.

The aerodynamic forces being aligned with the CM in this model, an aerodynamic moment M_{aero} [Nm] has been introduced in order to compute the pitch generally induced by lift, drag and braking. There comes:

$$ma_x = \sum_i F_{x,i} - \sum_i R_{x,i} - mg\sin(\alpha) - D_{aero} \quad (1)$$

$$0 = mg\cos(\alpha) - \sum_i W_i - L_{aero} \quad (2)$$

$$0 = W_f b - W_r c + \sum_i F_{x,i} h - \sum_i R_{x,i} h + M_{aero} \quad (3)$$

Where m [kg] is the vehicle's total mass, g [m/s^2] the gravitational acceleration, and $i = f, r$ whether the force is applied on the front or rear axle.

Low Speed Weight Distribution

From this equilibrium state, seeing that $b + c = L$, one can compute the weight [N] physically felt under the wheels on the front and rear axles, W_f and W_r respectively.

$$W_f = mg\cos(\alpha)\frac{c}{L} - mg\sin(\alpha)\frac{h}{L} - ma_x\frac{h}{L} - \frac{M_{aero} + D_{aero}h + L_{aero}c}{L} \quad (4)$$

$$W_r = mg\cos(\alpha)\frac{b}{L} + mg\sin(\alpha)\frac{h}{L} + ma_x\frac{h}{L} + \frac{M_{aero} + D_{aero}h - L_{aero}b}{L} \quad (5)$$

Propulsion/Traction or Braking Force

Knowing those efforts is a key information as they limit the forces $F_{x,i}$ [N] transmitted to the ground from the engine(s) (two, a thermal engine and an electric traction motor for a HEV) or from the brakes.

$$F_x = \frac{C_t + C_e - C_b + \sum_j I_{w,j}|\dot{\omega}_w|}{R_e} \quad (6)$$

Where R_e [m] is the effective radius (taking into account the tire penetration) of the wheels, and $I_{w,j}$ the inertia of the j^{th} organ in rotation with the wheel axle i (disc brakes, rim, tire...).
As shown on Figure 1, the ICE torque C_{ice} is effectively transmitted through a gearbox, two clutches and a differential with transmission yield η_{gb} [-], $\eta_{clutch} = 0.95$ [-] and η_{diff} [-] respectively; the ETM's C_{etm} [Nm] through the differential only; while the braking torque C_b [Nm] is directly applied to the wheel via disc brakes. Regenerative braking via the ETM acting as a generator is also possible and is computed as a negative C_e. While the braking path is direct, the thermal path thus denotes "ICE - clutch - gearbox - clutch - differential - wheel axle", and the electric path is for "ETM - differential - wheel axle". Their respective output torques C_t, C_e [Nm] affected by imperfect mechanical yield are:

$$C_t = \eta_{diff}\, i_{diff}\, \eta_{clutch}\, \eta_{gb}\, i_g\, \eta_{clutch}\, C_{ice} \quad (7)$$

$$C_e = \eta_{diff}\, i_{diff}\, C_{etm} \quad (8)$$

Where $i_g = \frac{\omega_t}{\omega_{sh}}$ [-] designates the ratio between the rotation speed of the ICE crankshaft and that of the motor shaft.

The torques and rotation speeds are explicitly shown on the architecture (Figure 4) in order to better apprehend where they are measured.

Rolling Resistance

The rolling resistance covers various phenomena of different natures such as friction in the driveline, dissipation in the suspension system, scrubbing of the tires on the ground, etc. Experience shows that it is simply modeled by a linearization of the vehicle weight:

$$R_{x,i} = \varphi_i \cdot W_i \quad (9)$$

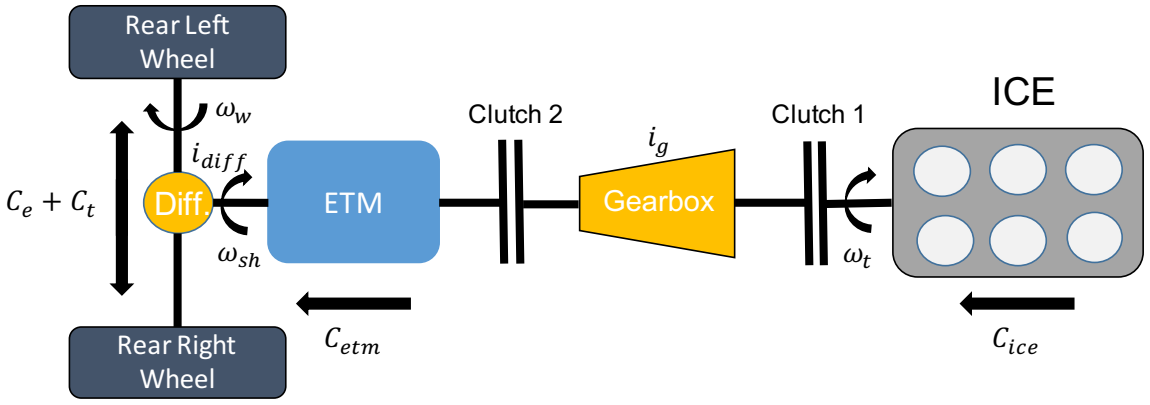

Figure 4: Torques and rotation speeds in the driveline

Where φ_i [-] is the rolling resistance coefficient and depends on the tire's structure, inflating pressure and its rotation speed (inducing "inflating" centrifugal effects) and also on the road conditions (smooth or gravelly, dry or wet). On normal cars, $R_{x,f} = R_{x,r}$ usually.

The conclusion of this equilibrium methodology is that there are only a limited number of outputs to explicit. Those are resistive efforts such as aerodynamics, dissipations of torque in the gearbox, the differential and the brakes, and of course propulsion torques via their respective engine model and energy source. All in all, this provides the basic sub-systems, or boxes, that constitutes a road vehicle.

3.2 Diagram of Operation

A second step towards a realistic vehicle simulator, is envisaging how the driver's commands - reactions to the road in front of him (turning the wheels, accelerating, decelerating) - are propagated between those sub-systems. This approach is called forward-facing modeling as opposed to backward-facing modeling. The latter takes as inputs the desired performances (for instance, the vehicle's speed) and then calculates the power required. Regarding this, the forward-facing modeling has the disadvantage of higher complexity and computational costs, but better transcripts the reality of vehicle control. The discrete diagram of operation is schematically detailed in Figure 5.
As one should read this schematics: the *Driver* receives a certain path (x, y) to follow on the track or an open road. Knowing the actual speed v_x of its car and where it is positioned ($\underline{X_V}$) on the track, he can react by turning the steering wheel of a certain angle that transfers into a displacement δ_{rp} of a rack and pinion steering gear. Of course, the *Driver* also adjust his foot position k_b on the braking or k on the accelerator pedal. This information is either directly transmitted to the *Brakes* that convert it into a braking torque C_b, or to what is called the *Power Split Device* (PSD) that decides the repartition of that load on the two engines (k_t is the throttle for the ICE and k_e for the ETM) in function of the availability of their respective energy source (mass of fuel m_ϕ in the tank and battery state of charge SOC).

k_t dictates the arrival of fuel m_ϕ in the ICE, and therefore its output torque C_{ice}. But these are also functions (generally called engine mapping) of the rotation speed of the crankshaft ω_t varying according to the rotation speed of the motor shaft ω_{sh} and the ratio i_g selected at the 6-Speed *Gearbox*. C_{ice} then transits via the motor shaft ($C_{sh} < i_g\, C_{ice}$ due to non-perfect gear coupling in the gearbox) to the $Differential$, where it is summed with the electrical path torque C_e to obtain the final torque distribution to the wheels ($C_{w,l}$ and $C_{w,r}$).

Talking of electromechanical torque, this one demands a certain intensity I of current in order to be produced by the ETM supplied with a voltage U. Those quantities are provided by the *Battery Pack* at U_{bat} which can undergo voltage drops following the demand of current I_{bat}. Hopefully, the voltage U is maintained constant thanks to *Power Electronics* as explained further.

Finally, the *Aerodynamics* "box" influences the vehicle's behaviour on the track via the computing of aerodynamic forces such as the lift L_{aero}, the drag D_{aero}, the lateral force $F_{y,aero}$ and the aerodynamic

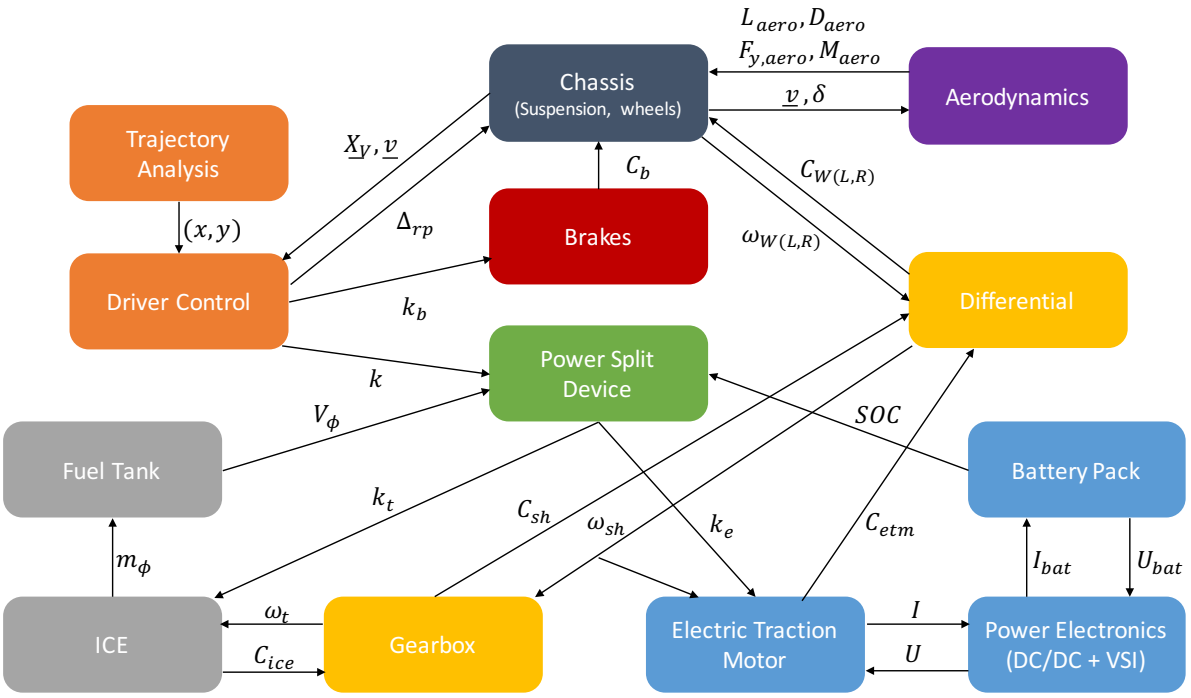

Figure 5: Principal components of a HEV with their respective inputs and outputs

moment M_{aero} that depend on the car's velocity $\underline{v}$ a and its orientation δ relative to the air flow.

3.3 Black Box Diagram

Each of the aforementioned models will be, for the sake of clarity, summarized as a "*Black Box*" equivalent. While Figure 5 brought to light their respective inputs and outputs - values that vary with time - the black box diagram is also supposed to give visibility to fixed parameters.
As this master thesis also includes a part about optimization, some of those parameters will have their values "left" to an optimization process (described further). They are distinguishable in red color.
Figure 6 shows a typical Black Box Diagram with its legend.

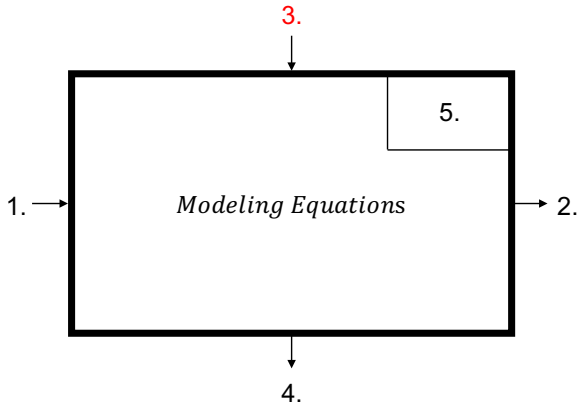

1. Inputs varying with time, logically computed by another *black box*
2. Outputs as computed by equations in the *black box*
3. Optimization parameters
4. Fixed parameters of value calculated in the *black box*
5. Hypotheses

Figure 6: Typical *Black Box* diagram

4 The Driver

Powerful embedded computing units and an ever bettering artificial intelligence has allowed vehicle driving to be more and more assisted; to the point that manufacturers like Tesla and now also Audi and BMW launched car models with full automatic pilot this year. In this work of simulation, the challenge is a bit different in the sense that a "virtual driver" is needed to test the modeled automobile on a track; and also because events in simulation are never supposed to be completely random, compared to reality.
The "Driver" here must react to the road in front of him only: no speed-limited zones, no other road users, etc... His job is thus separated in two controllers: one for steering and the other for accelerating.

4.1 Information on the track

Before selecting a strategy of operation, it is important to have clear sight of the information available from the track. A track design tool compatible with the simulation environment *Robotran* © used for this work, was provided. It interpolates check-points drawn by the user via splines so that each section of the road is a cubic function of X and Y coordinates. There is no Z-axis component as the track is completely flat (slope $\alpha = 0$ [°]). A schematic representation of a designed track is shown on Figure 7, with the equations of the splines between check-points 7 and 8.

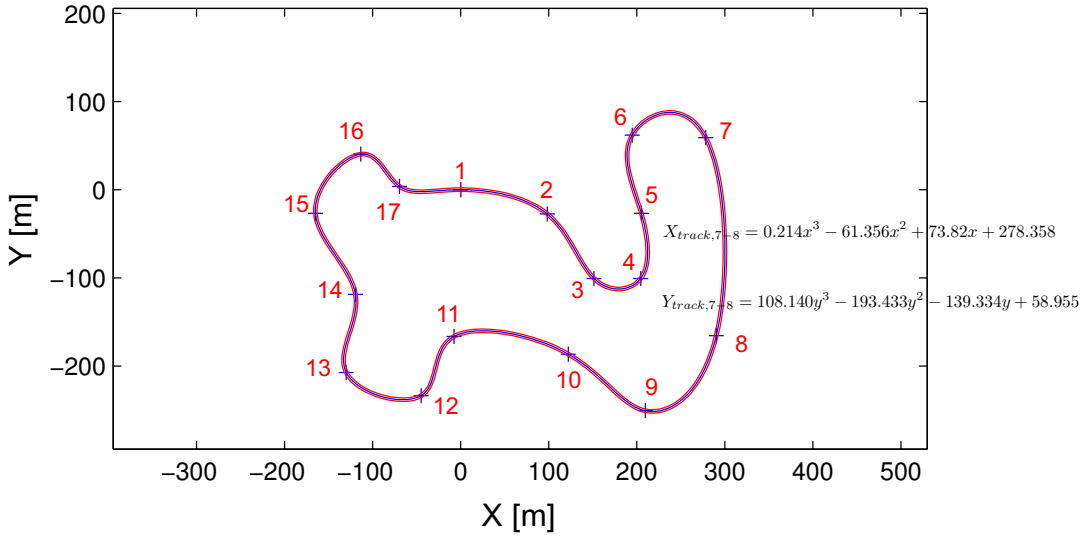

Figure 7: Track design representation

The road limits are 2 [m] appart of the described trajectory (i.e. the road is 4 [m] wide).

4.2 Steering

The steering controller will not be discussed in too many details here as it was not designed by the authors nor is it the purpose of this work.
It operates a four-bars steering mechanism via the displacement Δ_{rp} [m] of a rack-and-pinion gear.
Steering adjustments are made to maintain the car on the middle-point trajectory predefined by cubic splines. Cornering is thus always achieved in the centre of the lane, and offers no possibilities of taking advantage of the turns' apexes. It is therefore assumed that no optimization of the trajectory on the track is possible with this *Driver*. The steering controller is constituted of 3 "sub-controllers", each managing different information on the track.

1. A proportional-integral-derivative (PID) controller on the difference ϵ_{sc} [m] between the current position and the current spline assures that the vehicle stays in the middle of the road
2. A PD controller monitors the good orientation of the car σ_v [°] regarding that of trajectory at the target point σ_t [°] in front of it (tangent to the trajectory)
3. A weight is also attributed by a non linear function $f_{R,sc}$ to the curvature $1/R_{turn}$ [1/m] of the turn in the current section of the track

$$\Delta_{rp}(t) = PID(\epsilon_{sc}(t)) + PD(\sigma_t(t) - \sigma_v(t)) + f_{R,sc}\left(\frac{1}{R_{turn}(t)}\right) \tag{10}$$

Figure 8 gives an illustration of the pieces of information (in green) monitored in real-time for steering adjustments.

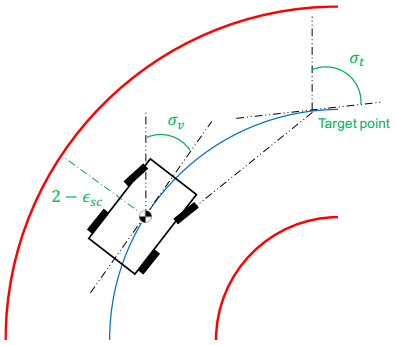

Figure 8: Informations necessary for the steering controller

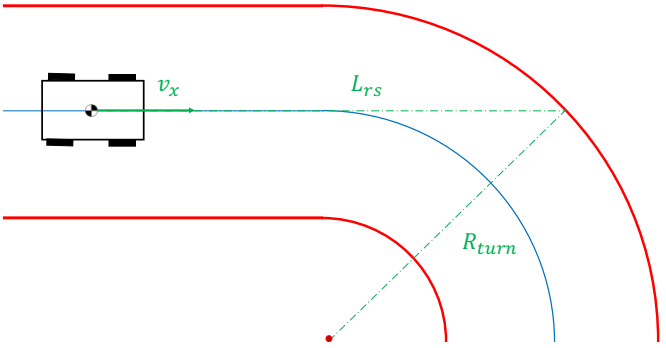

Figure 9: Informations necessary for the accelerating/braking controller

4.3 Accelerating / Braking

For the *Driver*'s response to the road in front of "him", in terms of throttle or braking load, the whole strategy adopted is based on the stopping distance L_{stop} [m]. If one recalls the expression for longitudinal equilibrium expression for the vehicle in straight motion, the deceleration can be computed as:

$$a_x = -\frac{1}{m}(F_b + R_x + D_{aero}) \tag{11}$$

Where F_b and R_x [N] are respectively the cumulative braking force and rolling resistance on both front and rear axles.

Equation 12 expresses the stopping distance, considering a *Driver* with null reaction/decision time and that the aerodynamic drag D_{aero} [N] is decreased as the square of the vehicle's longitudinal speed v_x [m/s] (see section 15).

$$L_{stop} = \frac{v_x^2}{2\ a_x} \approx \frac{v_x^2}{2\ F_b/m} \geq \frac{v_x^2}{2\ F_{long,MAX}/m} \tag{12}$$

Where m [kg] is the vehicle's mass and $F_{long,MAX}(\gamma_{long}, \sigma_w)$ [N] is the limit to the braking force evaluated in the tire model (see section 5.2), according to the current longitudinal slip ratio γ_{long} [-] and slip angle σ_w [°]. Above that limit, i.e. if $F_b > F_{long,MAX}$ [Nm] wheels begin to slip uncontrollably and L_{stop} [m] is increased.

The controller checks in real time the separation L_{rs} [m] between the vehicle and the roadside straight in front of it (on the x-axis in the vehicle's frame) and compares it to a security L_{secu} [m] based on that stopping distance:

$$L_{secu}(t) = \left(1 + k_{secu}\left(1 + \frac{k_{turn}}{R_{turn}(t)}\right)\right)\ L_{stop}(t) \tag{13}$$

R_{turn} [m] gives the next turn's radius ($1/R_{turn}$ [m^{-1}] its curvature) and k_{secu} [-] is a tuning parameter according to the *Driver*'s audacity (the smaller that coefficient is, the later he will push the brake pedal). For turns with curvature radius under the optimization parameter's value k_{turn} [m], it becomes risky to temporize the braking and a larger weight is therefore attributed.

A representation of the distances and longitudinal speed measured by the controller in real time is given in Figure 9 and so, at each time-step, two cases are possible:

If $L_{rs} > L_{secu}$ [m]

The road ahead is supposed straight and the *Driver* is authorized to accelerate. For this, a ramp raising the throttle k [-] up to $k_{max} \leq 1$ [-] (maximum allowed throttle) depends on an "aggressiveness" coefficient k_a [-] giving a slope to how hard the pilot is going to hit the gas pedal.

$$\text{if } L_{rs} > L_{secu} \begin{cases} k_b = 0 \\ k = k_a \, \Delta t \quad \in [0 \; ; \; 1] \end{cases} \tag{14}$$

In acceleration, the braking load $k_b = 0$ [-] obviously.

If $L_{rs} \leq L_{secu}$ [m]

The car is supposed to approach a turn and it becomes critical to hit the brakes. The braking load k_b [-] is adjusted to enter the curve at a velocity $v_{turn}(R_{turn})$ [m/s] clearly depending on the turn's curvature radius.

$$v_{turn} = k_v \, R_{turn} \tag{15}$$

k_v [1/s] being part of an optimum research. $v_{turn} = 0$ [m/s] logically for a U-turn with $R_{turn} = 0$ [m].

Of course, loading should be achieved intelligently: $F_b = k_b \, F_{b,max} < F_{long,MAX}$ [N] in order to prevent the braking force from locking wheels and slip from increasing uncontrollably. Unfortunately, this limit was not implemented due to simulation instability.

$$\text{if } L_{rs} \leq L_{secu} \begin{cases} \text{if } v_x \leq v_{turn} \begin{cases} k_b = 0 \\ k = k_a \, \Delta t \quad \in [0 \; ; \; 1] \end{cases} & \text{(16a)} \\ \text{elseif } v_x > v_{turn} \begin{cases} k = 0 \\ k_b = \frac{1}{F_{b,max}} \, \frac{m \, (v_x - v_{turn})^2}{2 \, L_{rs}} \quad \in [0 \; ; \; 1] \end{cases} & \text{(16b)} \end{cases}$$

4.4 Black Box

The *black box* 10 summarizes the process described; gathering in real time information of the track, on the vehicle speed and of the maximum transmissible braking force to the ground. Then evaluating the possibility of accelerating or the necessity of braking, loading is adjusted accordingly.
According to the specified objective, the *Driver*'s behaviour is optimized on the track regarding security braking distance k_{secu} [-], adjusted for each turn's curvature via k_{turn} [-], while the speed to approach them is defined thanks to k_v [-].

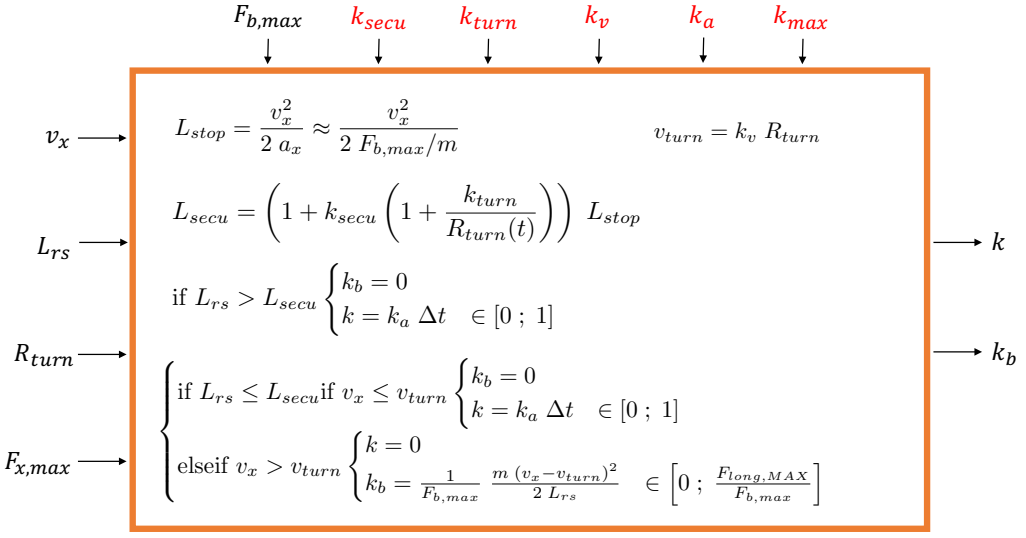

Figure 10: *Load controller* black box

5 Chassis

Even though it was not developed for the purpose of this work exclusively, a short description of the chassis used in this multibody simulation appeared important for the entire description of the vehicle model.
The advantage of working a defined chassis on a simulator like *Robotran* © is that all the movement equations are generated by the program and one can concentrate one's efforts on how to produce the movement itself, i.e. here to build a complete model of the powertrain and braking systems.

5.1 Suspensions and Antiroll Bars

Suspensions plays a critical role in the weight distribution and the vehicle's cornering dynamics by affecting [9]:

- Lateral load transfer
- Change in camber angles
- Roll steer
- Lateral force compliance steer
- Aligning torque
- Tractive force

Antiroll bars also, as their name implies, prevent roll (rotation around the x-axis in the vehicle's frame) by offering rolling stiffness in torsion, when a suspension is raised regarding the other. A schematics of the suspension flattening (inner wheel) and stretching (outer wheel) and the antiroll bar reaction in cornering is shown in Figure 11.

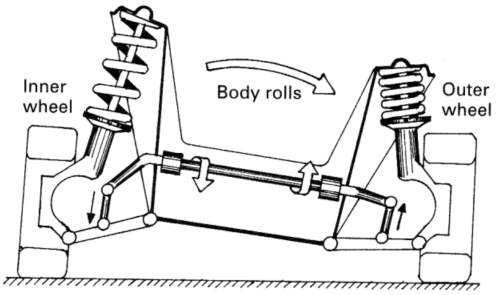

Figure 11: Antiroll bar's torsion in corners[1]

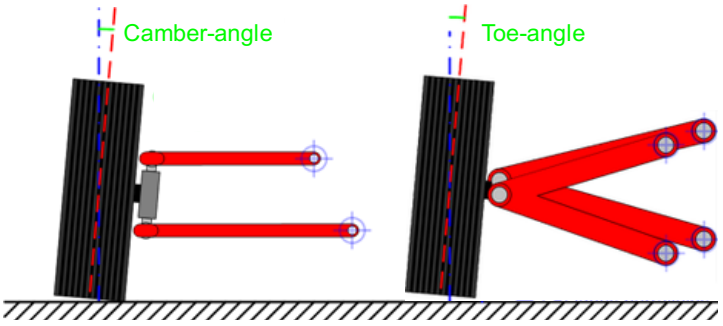

Figure 12: Front and top view of double wishbone suspension[2]

The chassis model under study is equipped with 2 antiroll bars (one on each axle) and the 4 suspensions are totally rigid double wishbone (see Figure 12) plus a mechanical damper.

It thus offers possibilities of optimization via parameters of camber-angle (rotation according to the vehicle's frame's z-axis), toe-angle (rotation according the y-axis) and the suspensions' and bars' stiffness and damping coefficient. Stiffnesses K_i [N/m] are already adapted according to the total mass of the vehicle which varies with the model's parameters' values.

$$K_i = K_{ref,i}\frac{m}{m_{ref}} \tag{17}$$

Where $K_{ref,i}$ [N/m] indicates the reference stiffnesses for the chassis supporting a vehicle of mass m_{ref}; m [kg] being its actual value.

[1] Victor A.W. HILLIER and Peter CROOMBES. Hillier's Fundamentals of Motor Vehicle Technology, volume 1. The Institute of the Motor Industry, 5th edition, 2004, Figure 7.38
[2] Original figure from https://fr.wikipedia.org/wiki/Suspension_de_véhicule, 20/05/16

5.2 Tire-to-Ground Model

A contact model is necessary to compute forces $\underline{F_w}$ [N] and moments $\underline{M_w}$ [Nm] at the base of the wheel. $\underline{F_w} = (F_{long},\ F_{lat},\ F_{vert})$ [N] gives the longitudinal, lateral and vertical forces that apply on the road respectively. The pure torque vector $\underline{M_w} = (M_{roll},\ M_{pitch},\ M_{yaw})$ [Nm] which components are the overturning, the rolling resistance and the aligning torque. Fortunately, a tire-to-ground model (TTG) is already implemented in the simulation environment *Robotran* ©.

The vertical ground/tire force F_{vert} [N] depends on the tire penetration $p_w = (R_w - R_e)$ [m] (R_w [m] the nominal wheel radius, and R_e [m] its effective value) following the weights actual repartition of the vehicle and suspension's response.

$$F_{vert} = K_{w,rad}\, p_w + \varrho_{w,rad}\, \dot{p}_w \tag{18}$$

Where $K_{w,rad}$ [N/m] is the radial stiffness and $\varrho_{w,rad}$ [N/(m/s)] the damping coefficient of the tire respectively.

F_{vert} [N] then serves as an input for computation of the other contact forces via empirical non-linear functions according to the Bakker model. Their authors indeed proposed a series of formulae for evaluation of F_{long} [N], F_{lat} [N] and M_{yaw} [Nm] in terms of the longitudinal slip γ_{long} [-] (or expressed as a percentage $\gamma'_{long} = 100\gamma_{long}$ [%]), of the slip angle σ_w [°] and of the camber angle ζ_w [°] [1].

Figures 13 and 14 show representations of those functions for $F_{vert} = 1000$ [N] and $\zeta_w = 0$ [°]

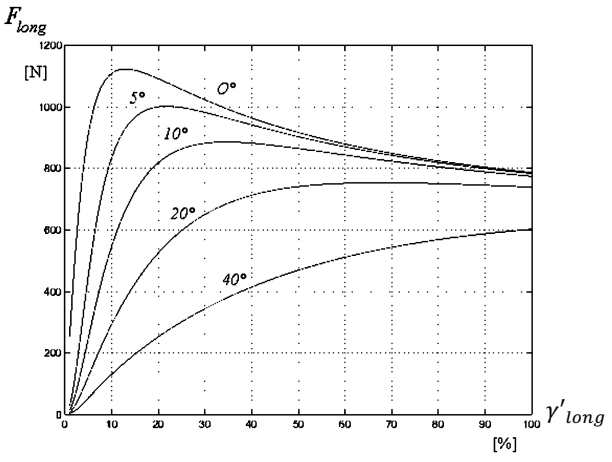

Figure 13: Bakker model for longitudinal force [1]

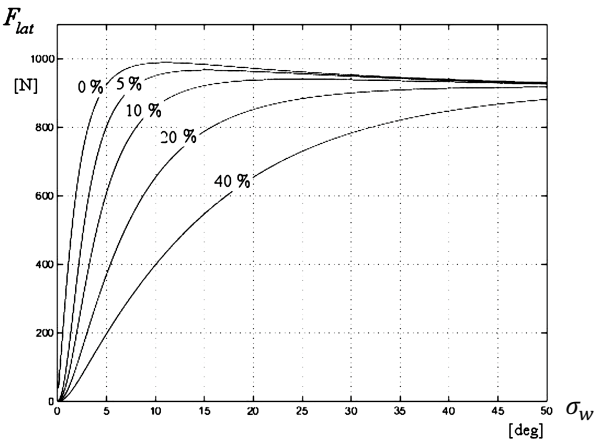

Figure 14: Bakker model for lateral force [1]

"Both F_{long} [N] and F_{lat} [N] obey a "natural" saturation effect for large slip, all the more reduced since the slip in the other direction increases: this simply illustrates the fact that the reserve of longitudinal force - for instance - is larger when braking along a straight line than in a curve." [1]

Those forces give thus limits to the maximum transmissible forces to the ground in various situations and can therefore be used for the implementation, for example, of an anti-lock braking system (ABS).

6 Power Split Device

This chapter presents the strategy used to determine the best power split between thermal and electrical path in real time. This requires local optimization inside the global one.

6.1 Problem Statement

For stating the optimization problem, a strong hypothesis is firstly made: electricity is considered as a "free source of energy", and even though it is not the case on a global scale, the only cost attributed to the battery current state of discharge is that it will not be available to supply the powertrain architecture in the future; or at least not without regenerative braking.
The whole base for intelligent power management strategy is thus to energetically evaluate the road ahead. For obvious reasons, this is absolutely not optimally achievable in a real-time operation. However, power split controllers based on minimization of the fuel consumption seem to be one step ahead of simple maps based on data acquired about the drivers' habits, even when frequently updated [10].

In order to build a power split logic, two hypotheses have to be introduced. Firstly, "no - or only limited - *a priori* knowledge of the future driving conditions is available during the actual operation. Secondly the self-sustainability of the electrical path has to be guaranteed. This is due to the fact that the storage system is not expected to be recharged by an external device, but rather during the vehicle operation by fuel conversion and by means of regenerative braking." [11]
The cost function to be minimized at each instant (real-time operation) has to rely on measurable system variables which obviously include the fuel consumption, but also variations in the SOC in order to guarantee the charge-sustainability.

6.2 Direct Programming

Firstly, a methodology often used, and most optimal, is the dynamic programming (DP) algorithm as it is very well suited for the job of taking successive, interrelated decisions. This one considers the vehicle as a discrete dynamic system, with SOC state and ETM power output as control variables. The power necessary for the vehicle to overcome the travel is evaluated; each split allowed by charge-sustainability is considered, and the solution that minimizes fuel consumption is elected. This technique is thus only feasible off-line as the driving cycle has to be known before operation, and requires heavy duty processing. However, being the optimal solution to the global problem of maximizing fuel economy, this method remains an important tool for evaluation of other sub-optimal strategies.

6.3 Equivalent Consumption Minimization Strategy

A promising approach consists in attributing an equivalent fuel consumption to the electrical path as its operation generates variations in the SOC: it is called the ECMS for equivalent consumption minimization strategy.
An equivalence factor s [-] between electrical E_e [J] and fuel energy use E_t [J] is thus introduced and is basically evaluated by taking average efficiency of their transformation into work (motor) or into storable electricity (generator).

$$E_e(t) = \int_0^t E_{bat}\ \dot{SOC}(\tau)d\tau \tag{19}$$

$$E_t(t) = \int_0^t LHV(\tau)\ \dot{m}_\phi(\tau)d\tau \tag{20}$$

$$E_w(t) = \int_0^t C_w(\tau)\ \omega_w(\tau)d\tau \tag{21}$$

Where $E_{bat} = 3600 Q_{bat,0}\ U_{bat,0}$ [J] represents the total energy capacity of the battery ($Q_{bat,0}$ [Ah] and $U_{bat,0}$ [V] the battery capacity and open-circuit voltage respectively - see section 9 *Battery Pack*). Note that certain ECMS define $E_e(t)$ as an integration of the battery electrical power supply (cfr. [12]), but the presence here of the variation in SOC accounts for losses and nonlinearities in the battery, and multiplied by E_{bat} [J], gives the electrochemical power used for electric powertrain operation [2]. $\dot{m}_\phi$ [kg/s] is the consumption of fuel of lower heating value $LHV = 43$ [MJ/kg], while E_w [J] gives the motor work

necessary to propel the car at the torque C_w [Nm] and rotation speed ω_w [rad/s] demanded at the wheels.

The cost function J [kg_{fuel}/s] of the optimal local control problem is thus:

$$J(u,t) = \dot{E}_t(u,t) + s(t)\,\dot{E}_e(u,t) \qquad \overset{eq}{=} \qquad \dot{m}_{\phi,eq}(u,t) = \dot{m}_\phi(u) + s(t)\frac{E_{bat}}{LHV}\dot{SOC}(u,t) \tag{22}$$

Of which value is minimized at each instant, by the torque split ratio $u(t) = u^*(t)$ [-]:

$$C_w(t) = C_e(t) + C_t(t) \qquad \text{where} \begin{cases} C_e(t) = u(t)C_w(t) \\ C_t(t) = (1-u(t))C_w(t) \end{cases} \tag{23}$$

Remember that $C_e(t) = \eta_{diff}\,C_{etm}$ [Nm] and $C_t = i_g\,\eta_{box}\,\eta_{diff}\eta^2_{clutch}\,C_{ice}$ are respectively the electrical and thermal paths output torques.

Of course, s [-] would be independent of time if the engines (ICE and ETM) were operated at constant yield; but the latter depends on the operating point of each motor (see respective sections) and, hence, must be averaged on the drive-cycle to deal with.
Indeed, if s [-] is too high, the electrical path will be penalised and fuel consumption will not be minimized. On the contrary, if it is too low, the electrical path is favoured and will not remain charge-sustaining. The phenomenon is exposed in Figure 15 for the drive-cycle shown.

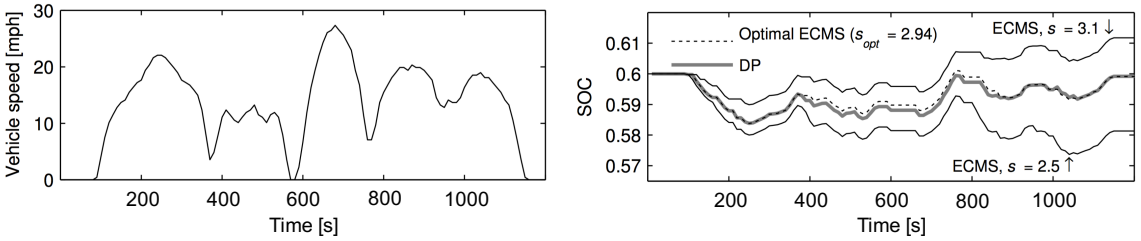

Figure 15: ECMS with constant equivalence factor on drive-cycle [2]

This means that s [-] should be part of another local optimization processed off-line too, following the drive-cycle, and thus making ECMS not more compatible with the first aforementioned hypothesis than DP.

6.4 Adaptive ECMS

Fortunately, this method can be made adaptive (A-ECMS), refreshing its equivalence factor based on past driving conditions. In [12], the authors proposed an adaptation making use of a Kalman filter to predict the future vehicle speeds: showing good results while quite computationally demanding. Here, and following the conclusion taken in [2], the idea is to bring corrections to $s(t)$ [-] at regular intervals of time Δt [s] in order to counteract SOC deviations from its reference value SOC_{ref}(= 0.6 [-] for instance), giving a "heavier weight" to the electrical path use when the SOC drops and "lighter weight" when the battery is near full charge.
To improve stability, the power split device keeps in memory the two previous values of s [-], and the adaptation law [2] is given by (24):

$$s(t) = \frac{s(t-\Delta t) + s(t-2\Delta t)}{2} + k_{P,psd}\,(SOC_{ref} - SOC(t)) \tag{24}$$

Where $k_{P,psd}$ [-] is the proportional gain of the feedback controller on SOC, and is a tuning parameter for the strategy.
Simulation results are given for DP, optimal ECMS and with adaptation every $\Delta t = 10$ [s] are shown in Figure 17 for the driving cycle 16.

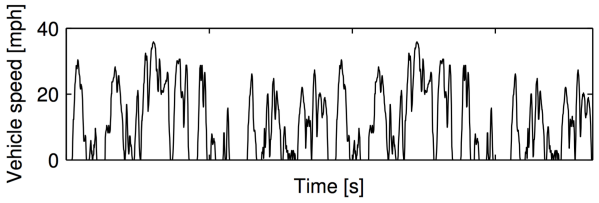

Figure 16: Evaluating driving cycle for A-ECMS performances [2]

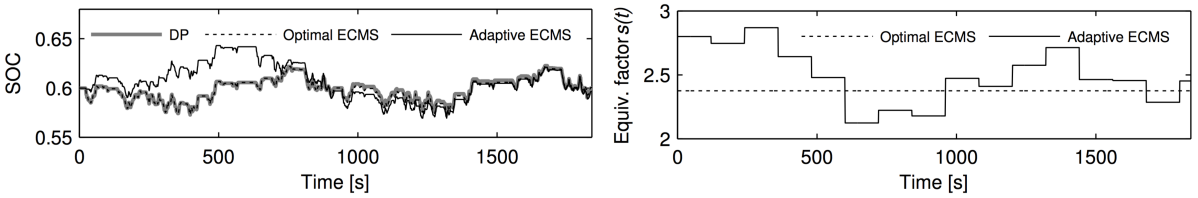

Figure 17: A-ECMS performances comparison [2]

6.5 Black Box

At this point, throttle k [-] as demanded by the *Driver* is known. For the purpose of splitting it on both types of motorization, local minimization is performed the A-ECMS cost (or equivalent consumption) function J [kg_{fuel}/s] is considered with an equivalence factor re-evaluated every Δt [s] via equation (24). Near optimal torque split ratio $u(t) = u^*(t)$ is computed. Thermal and electrical loads are prescribed to their respective engines. A security check is done to be sure that $u^*(t)$ [-] does not request more torque than available (depending on the actual operating point of the selected motorization) and if that case occurs, part of the work is transferred to the second engine while the most requested is at full throttle.

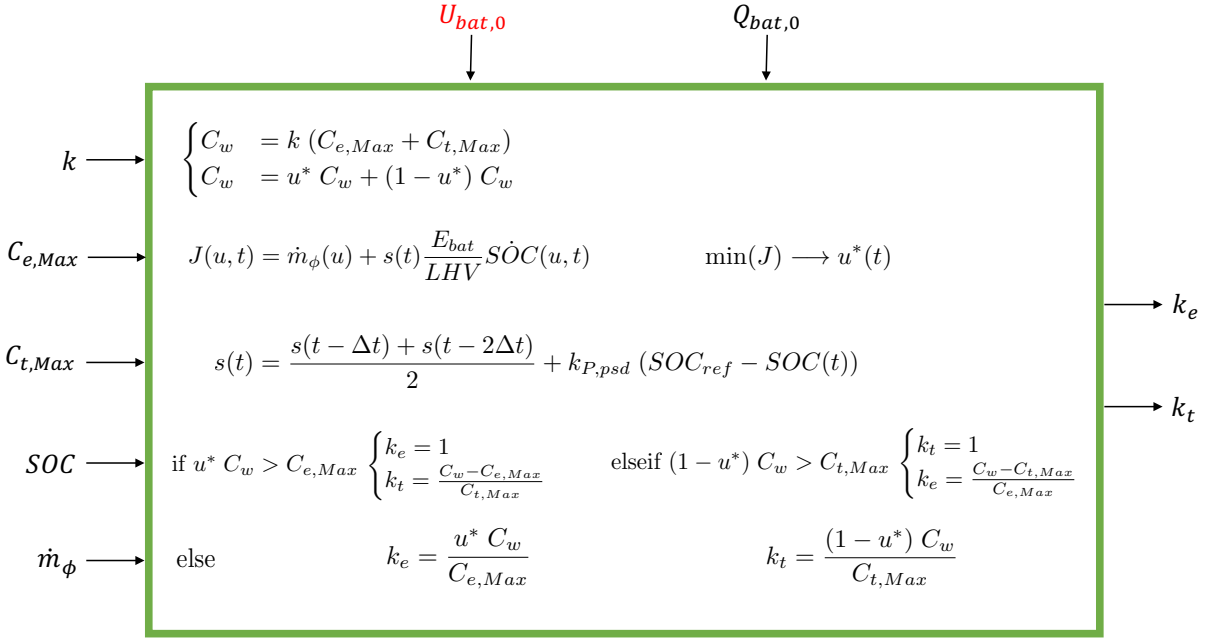

Figure 18: *Power Split Device* Black Box

7 Brakes

7.1 Basic System

In a car braking systems, the pressure applied by the caliper pistons on the discs is basically controlled by a hydraulic circuit pressurized by the master cylinder as seen in Figure 19.

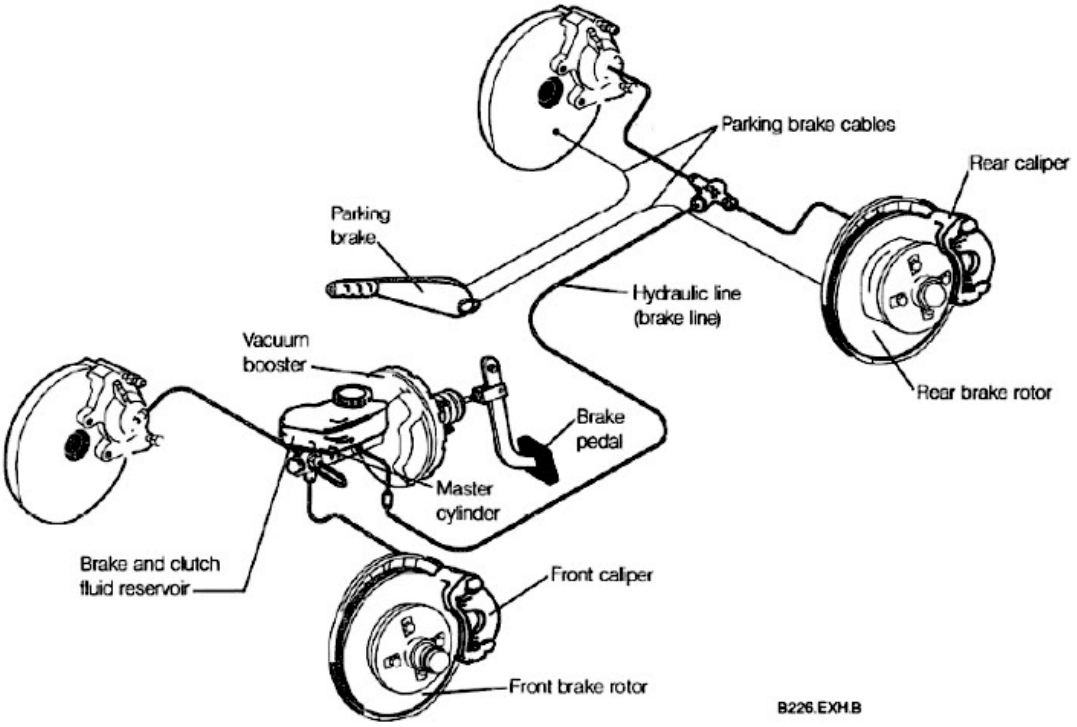

Figure 19: Brake lines diagram[3]

As, for the purpose of this work, the vacuum booster (not present in any system) is considered linear, the pressure $p_{b,mc}$ [Pa] at the master cylinder is a direct reflection of the pressure applied on the braking pedal (or braking load $k_b \in [0;1]$ [-]):

$$p_{b,mc} = k_b p_{b,max} \tag{25}$$

Where $p_{b,max}$ [Pa], even in racing-dedicated braking systems, usually does not exceed 100 [bar] $= 10^7$ [Pa].

For the sake of simplicity, the repartition of the braking load between front and rear axles is fixed beforehand here by the dimensioning of the discs and is thus not dynamically changed during operation (as it can be on newer systems). Moreover, the left and right wheels of one axle are affected by the same braking torque C_b [Nm], as long as the Electronic Stability Program (ESP) is not triggered (read further). The pressure p_b [Pa] applied by the calipers on their respective discs is thus the same, and supposed to be one fourth of the total master cylinder pressure.
From that point, and following the schematics proposed on Figure 20, the braking torque applied on one wheel mounted on the front axle f ($(l;r)$ for left and right) is computed by equation (26) [13]:

$$C_{b,f,l} = C_{b,f,r} = \frac{1}{2}\frac{F_{b,f}}{R_e} = 2\mu_b p_b R_{b,f} A_b \tag{26}$$

Where R_b [m] is the brake disc radius, dimensioning parameter for the optimization of the brake repartition $R_{b,f}/R_{b,r}$. μ_b [-] is the friction coefficient between the pads and the disc (2 similar contacts at both sides of the disc); A_b [m^2] is the pads' surface in contact with the disc; supposed equal for both front and

[3]Courtesy of Photobucket user srainey1, http://s106.photobucket.com/user/srainey1/media/5%20Lug/BrakesSystem.jpg.html, 07/04/2016

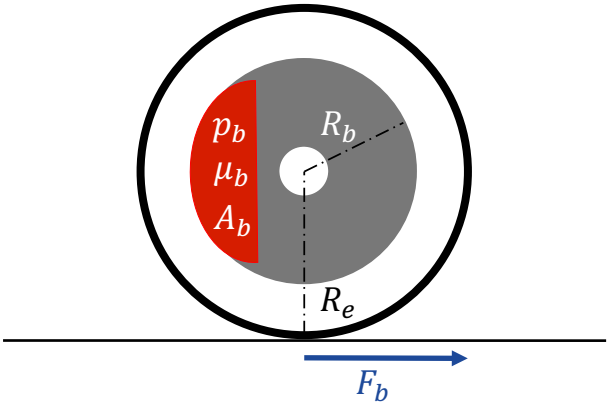

Figure 20: Brake disc's schematics

rear axles (even though it is never the case in practice, this detail is of lesser importance), and taken as a mean of manufacturers' (such as Brembo®) data regarding high performances ceramic brakes:

$$\mu_b = 0.40 \qquad A_b = 80 \text{ [cm}^2\text{]} \tag{27}$$

7.2 Regenerative Braking

Concerning the braking on the rear axle, computations are slightly complicated because of regenerative braking via the ETM in generator mode. Firstly, the demand of braking torque $C_{b,r}$ on the rear axle is computed:

$$C_{b,r} = \frac{1}{2}\frac{F_{b,r}}{R_e} = 4\mu_b p_b R_{b,r} A_b \tag{28}$$

The maximum regenerative electric braking torque $C_{b,e,max}$ [Nm] is calculated according to the actual battery's state of charge, limitations in current intensity, and the power electronics' adaptability (see respective sections). Priority is given to regenerative braking following orders (29a) and (29b):

$$\begin{cases} C_{b,e} = C_{b,r} & \text{if } C_{b,r} \leq C_{b,e,max} \quad (29a) \\ C_{b,r,l} = C_{b,r,r} = \frac{1}{2}(C_{b,r} - C_{b,e,max}) & \text{if } C_{b,r} > C_{b,e,max} \quad (29b) \end{cases}$$

As an illustration, a HEV equipped with an ETM of 595 [Nm] maximum output torque, has been put to a 100-0 [km/h] braking test. The gear reduction ratio at the differential provides $C_{b,e,MAX} = 2000$ [Nm] in the slower speeds region (see chapter 8 for details over ETM operation). The braking torques, as demanded by the operator $C_{b,asked}$ [Nm], applied via the 4 discs $C_{b,discs}$ [Nm] and via regenerative braking $C_{b,etm}$ [Nm] are shown in Figure 21.

7.3 Brakes' Mass and Inertia

As in-wheel brakes constitute non-suspended masses, it is imperative to compute their overall weight. Again, based on manufacturer's catalogs' data, caliper and pistons usually reach 5 [kg], pads are around 800 [g] and a linearization regarding the disc radius R_b [m] gives empirical formulae for the brakes' mass m_b [kg]:

$$m_{b,i,l} = m_{b,i,r} = 5 + 2 \cdot 0.8 + 7.00 \cdot R_{b,i} \tag{30}$$

With $i = \{f; r\}$ for front or rear axle.

Perhaps more critical than the brakes' mass is their inertia I_b [kg $\cdot$ m^2] inside the wheels (recall equation (6) for the propulsion or braking force):

$$I_{b,i} = m_{b,i}\, R_{b,i}^2 \tag{31}$$

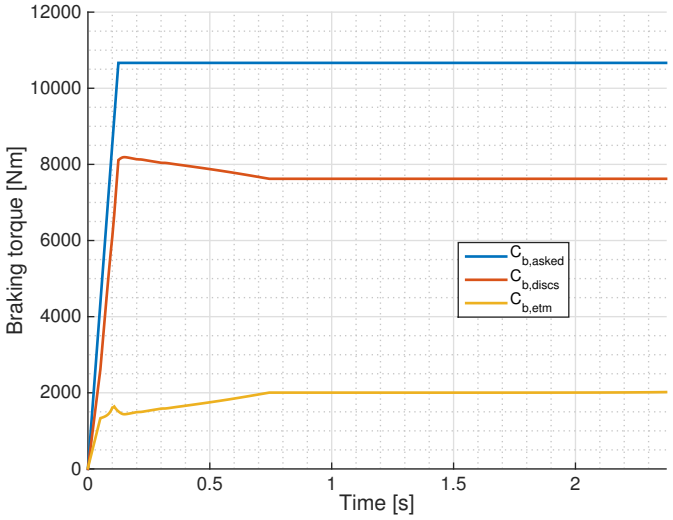

Figure 21: 100-0 [km/h] test with regenerative braking

7.4 Black Box

As always, the *Brakes'* purely mechanical, non-thermal nor fluid-dependent model is summarized in Figure 22 under the "black box" form. The braking rear / front repartition $R_{b,r}/R_{b,f}$ [-] is an optimization parameter as it influences the dynamic behaviour of the car. $R_{b,r}$ [m], fixing the maximum available braking torque is also a specific data that can be changed following the track.
k_b [-] is the loading input coming from the *Driver*'s command while $C_{b,e,max}$ [Nm] is computed *ETM* black box according to its actual operating point (see section 8).
Finally, k_e [-] is computed for the control of the ETM, the different $C_{b,i,j}$ [Nm] ($i \in \{f,r\}$ and $j \in \{l,r\}$) are applied to their respective wheel (i,j) and the non-suspended masses $m_{b,i,j}$ [kg] are affected.

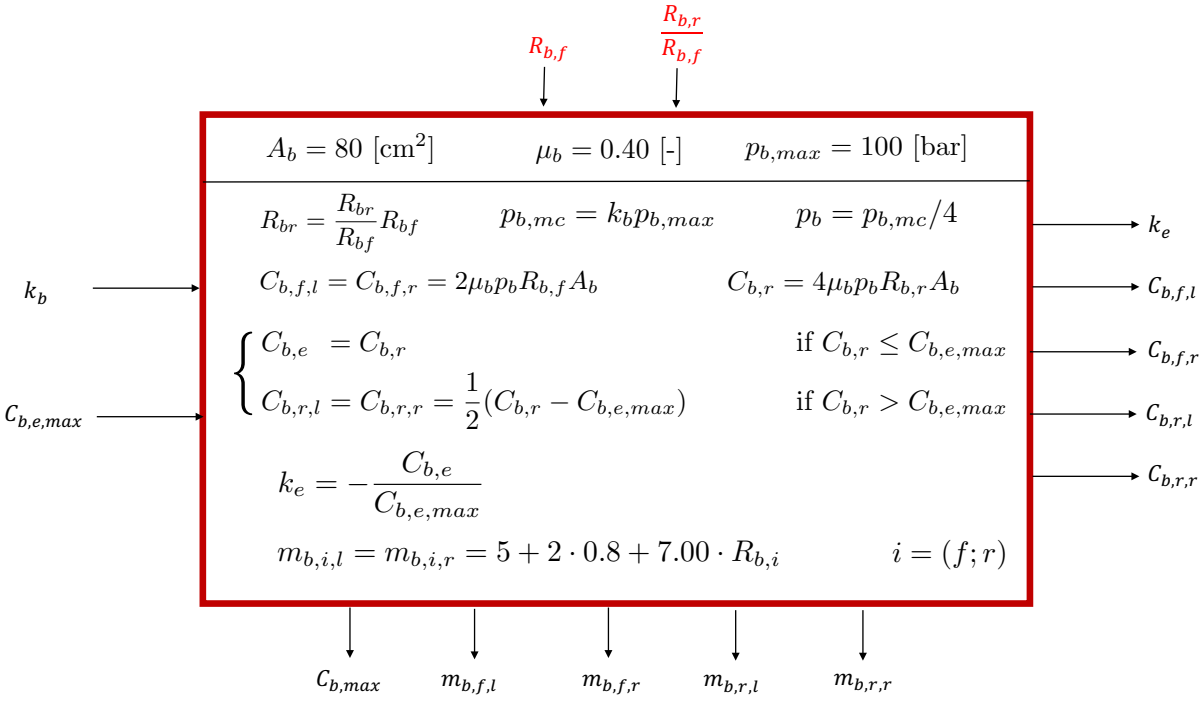

Figure 22: *Brakes* black box

7.5 Electronic Stability Program

In order to improve dynamic stability in curves, wheels may also be braked independently following a super-controller: the Electronic Stability Program (ESP)[4]

The basic principle of the ESP is to slow down one wheel (thus only possible through the discs; regenerative braking being available only on both rear wheels) in order to create a moment of force around it and so rectify the trajectory when a loss of control is detected. It has to be noted that the basic configuration presented in Figure 19 has to be adapted to allow independent braking management.
Measuring the steering angle $\delta_{w,f,l}$ [°] on the front left wheel only, the turn's curvature radius R_{turn} [m] can be computed depending on that wheel being inside or outside the curve, and so the yaw rate $\dot{Y}_{r,want}$ [rad/s] as wanted by the *Driver*.

$$\dot{Y}_{r,want} = \frac{v_x}{R_{turn}} \quad \text{with} \quad \begin{cases} R_{turn} = \infty & \text{if } \delta_{w,f,l} = 0 \\ R_{turn} = \sqrt{\left(\frac{L}{2}\right)^2 + \left(R_{turn,f,l}\cos\left(\delta_{w,f,l}\right) + \left(\frac{w_v}{2}\right)\right)^2} & \text{if } \delta_{w,f,l} > 0 \\ R_{turn} = -\sqrt{\left(\frac{L}{2}\right)^2 + \left(R_{turn,f,l}\cos\left(\delta_{w,f,l}\right) + \left(\frac{w_v}{2}\right)\right)^2} & \text{if } \delta_{w,f,l} < 0 \end{cases} \tag{32}$$

Where v_x [m/s] is the lineic speed in the vehicle's frame, L [m] and w_v [m] its wheelbase and track width respectively. $R_{turn,f,l}$ [m] is defined as the turn's curvature radius at the front left wheel:

$$R_{turn,f,l} = \left| \frac{L}{\sin\left(\delta_{w,f,l}\right)} \right| \tag{33}$$

Comparing the yaw rate $\dot{Y}_{r,want}$ [rad/s] with its actual value $\dot{Y}_r$ [rad/s] determined by a gyroscope, neutral steer, oversteer or understeer is detected and the suited wheel is braked accordingly (see black box 23).

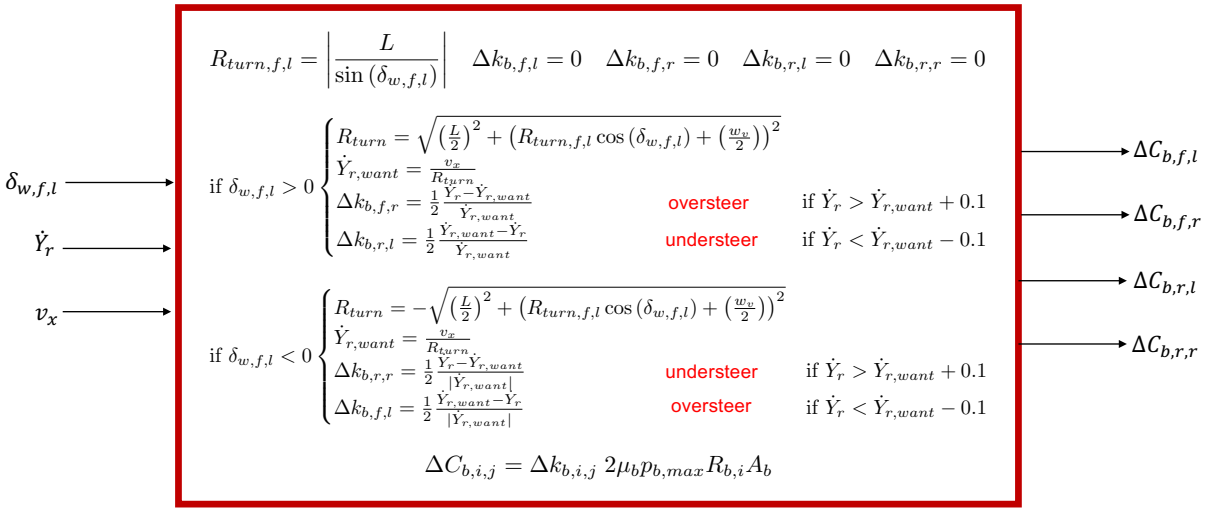

Figure 23: *ESP* super-black box

7.6 Possible Improvements

As it is well known by any racetrack engineer, materials composing the brakes - and particularly when they include carbon - tend to have a totally different behaviour in non-usual operating temperatures. Indeed, gradient in the disc brakes can exceed 500 [°C/s], and output braking torque is therefore affected. Those differences in operation of the brakes could easily be computed by a variation of $\mu_b(T_b)$ according to the temperature of the interface pads / disc. However, being air cooled, and the modeling work of this thesis not taking aerodynamic variations around the wheels, a physically correct thermal model of the brakes was not achievable here. Instead, brakes are supposed to be perfectly cooled and their operating temperature staying at nominal constant value.

[4]also labeled under other names: Electronic Stability Control, Dynamic Stability Control, Vehicle Stability Control, Dynamic Stability and Traction Control, Vehicle Stability Assist, etc...

8 Electric Traction Motor

8.1 Machine Selection

The difficulty in the early phase of modeling an electric traction motor is firstly to decide which architecture to elect. Indeed, numerous structural organizations of the motor already exist or are under study for near future development. Suited for the job of propelling an automobile, there are induction machines (IM), permanent magnets synchronous machines (PMSM) and switched reluctance motors (SRM). If the latter type shows promising results, its spectral range of operation is still hard to master. Induction motor drives are, them, very reliable, low cost and provide wide field weakening range. However, compared to PMSM, they have lower efficiency and power density. PMSM also present the advantage of being operated in motor or generator according to the direction of the current.
With the purpose of obtaining a fully optimized powertrain, it thus appeared clear to go for a PMSM. But in this type of drive even, different configurations are possible. Following the design principles presented in [6], the research was narrowed on topologies with interior permanent magnets (IPM) (read further).

This section strives to bring a complete multi-physics model for deep understanding of the influences of each dimensional parameter on the performance of the electric drive. Sometimes simplified, the objective was also to reduce the number of those parameters by coupling them or by arbitrarily maximizing the space available. The importance of a model taking into account the relation between multiple physics such as electricity and magnetism obviously, but also thermodynamics and vibratory (not kept in this model as it presents a weaker link) is exposed in [14].
It has to be recalled that this is a work of simulation and in no case, the values obtained by optimization processes have been verified, at least not for the purpose of this thesis, by actual prototyping; the only way to fully validate a model.

8.2 Electrical Path Architecture

In order to clearly visualize its components and values, the electrical power architecture is shown in Figure 24.

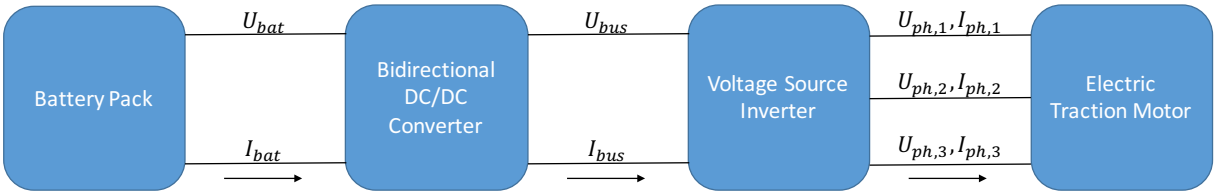

Figure 24: Electrical power architecture

In motor operation, DC power (U_{bat} [V], I_{bat} [A]) flows from the battery to the ETM (the opposite situation appears in generator mode). A bidirectional DC/DC converter assures constant DC voltage U_{bus} [V], adapting its transfer gain following voltage variations at the battery. U_{bus} [V] is then inverted by a DC/AC voltage source inverter (VSI) to supply tri-phase current and voltage $U_{ph,j}$ [V] and $I_{ph,j}$ [A] ($j \in \{1,2,3\}$) (see section 10). Voltage inversion is here supposed ideal (perfect respect of the spectral content of the signal without any introduction of noise) with modulating signals $\hat{m}_{VSI,j}$ constituting a symmetric 3-phase, direct order system.

8.3 $dq0$ Transformation

The $dq0$ or direct-quadrature-zero transformation is a mathematical tool particularly important for vector control of electric machines like a tri-phase PMSM drive for instance, as it no longer places the electric quantities in the tri-phase source (1;2;3) frame but directly in the 2-dimensional (direct d and quadrature q) frame of the motor in rotation.
Since it is only a tool for the development of the ETM model, a complete description of the $dq0$ transformation can be found in appendix A.1. The read non familiar with this technique is advised to browse it.

8.4 Drive Control

As presented before, the ETM receives its first control input k_e [-] from a local optimization process in the *Power Split Device*. This throttle value gives the proportion of maximum available torque $C_{e,Max}(\omega_e)$ [Nm]:

$$C_{em}(t, \omega_{sh}) = k_e(t)\ C_{e,Max}(\omega_{sh}) \tag{34}$$

Where C_{em} [Nm] gives a notion of the desired output torque. It is the electromagnetic torque defined as:

$$C_{em} = \frac{P_{em}}{\omega_{sh}} = \frac{m_{ph}}{\omega_{sh}}(E_0\ I_q + I_d\ I_q\ (X_d - X_q)) \tag{35}$$

m_{ph} [-], the number of phases will be fixed here at 3 as tri-phase supply are well mastered with today's power electronics. Stator windings, from which are found the direct and quadrature components I_d and I_q [A], are therefore supplied with currents $i_j(t)$ [A] and voltages $u_j(t)$ [V] ($j \in \{1, 2, 3\}$ obviously) of the form:

$$i_1(t) = \sqrt{2} I_{ph,1} \cos(\omega_e t) \tag{36}$$

$$i_2(t) = \sqrt{2} I_{ph,2} \cos\left(\omega_e t + \frac{2\pi}{3}\right) \tag{37}$$

$$i_3(t) = \sqrt{2} I_{ph,3} \cos\left(\omega_e t + \frac{4\pi}{3}\right) \tag{38}$$

$$u_1(t) = \sqrt{2} U_{ph,1} \cos(\omega_e t) \tag{39}$$

$$u_2(t) = \sqrt{2} U_{ph,2} \cos\left(\omega_e t + \frac{2\pi}{3}\right) \tag{40}$$

$$u_3(t) = \sqrt{2} U_{ph,3} \cos\left(\omega_e t + \frac{4\pi}{3}\right) \tag{41}$$

Where $I_{ph,j}$ [A] and $U_{ph,j}$ [V] are the j^{th} phase current and voltage respectively. ω_e [rad/s] is the supply frequency which, for a synchronous motor, equals the rotation speed of the shaft multiplied by p [-], the number of pair of poles: $\omega_e = p\omega_{sh}$ [rad/s].

E_0 [V] is the back electromotive force (emf) induced in the stator windings by the permanent magnets (PM):

$$E_0 = \psi_{PM}\omega_e = n_c\ \phi_{PM}\ \omega_e \tag{42}$$

n_c [-] is the number of turns constituting the coils/windings in the stator. ϕ_{PM} [Wb]=[T $\cdot$ m^2] is the air-gap magnetic flux generated by the PM and $\psi_{PM} = n_c\ \phi_{PM}$ [Wb] is its linkage with the stator windings. n_c [-] and ϕ_{PM} [Wb], with winding reactances $X_d = \omega_e\ L_d$ and $X_q = \omega_e\ L_q$ [Ω] (L [H] designating inductances) are fixed by the dimensions of the drive. These are quite critical regarding its performances. The subject is thoroughly treated in appendix A.2.

Anyway, equation (35) can now be rewritten as:

$$C_{em} = m_{ph}\ p\ I_q(n_c\ \phi_{PM} + (L_d - L_q)I_d) \tag{43}$$

I_d and I_q [A] are computed with the help of equations (44) and (45) for the direct and quadrature voltages U_d and U_q [V] respectively:

$$U_d = Z_s\ I_d - X_q\ I_q \tag{44}$$

$$U_q = Z_s\ I_q + X_d\ I_d + E_0 \tag{45}$$

Z_s [Ω] is the stator windings' impedance, being also influenced by the ETM dimensions (notably by the wire's cross section S_{Cu} [mm^2]). It is thus also described in appendix A.2 about the motor design.

As (43), (44) and (45) make a system of only 3 equations for now 4 unknown variables, the two modes of operation are introduced: the constant torque and then flux weakening operation [15], as visible in mappings 25 and 26 (extracted from [6]).

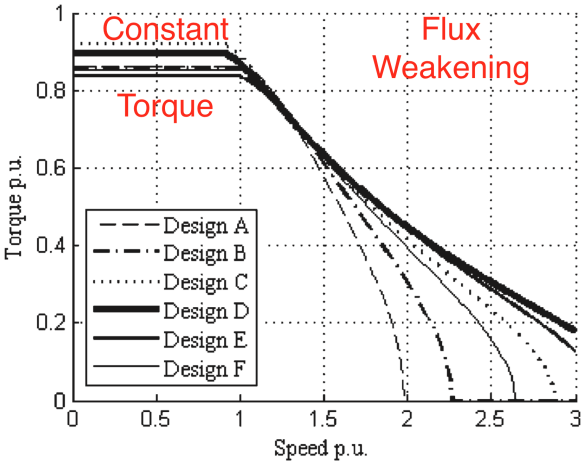

Figure 25: Electromagnetic torque output mapping

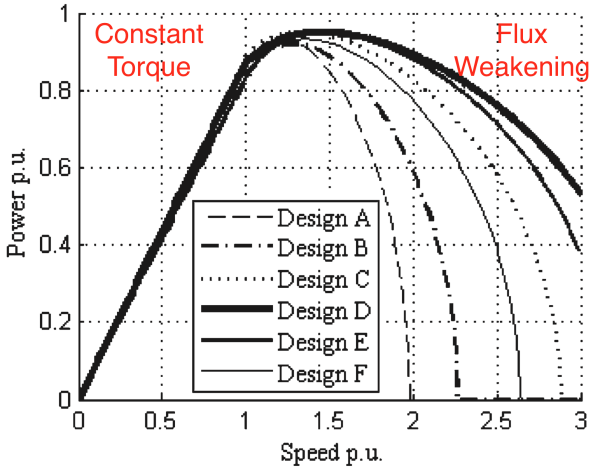

Figure 26: Electromagnetic power output mapping

Constant Torque Operation

For rotation speed $\omega_{sh} < \omega_b$ below the base speed ω_b [rad/s], no direct-axis current is injected because of thermal limitations in the ETM at low speeds (see the thermal modeling of the ETM in appendix A.3). $I_d = 0$ [A] is thus the missing equation to compute system (43), (44), (45), rewritten as:

$$I_d = 0 \tag{46}$$

$$I_q = \frac{C_{em}\omega_e}{m_{ph}\ p\ E_0} = \frac{C_{em}}{m_{ph}\ p\ n_c\ \phi_{PM}} \tag{47}$$

$$U_d = -X_q\ I_q \tag{48}$$

$$U_q = Z_s\ I_q + E_0 = Z_s\ I_q + n_c\ \phi_{PM}\ \omega_e \tag{49}$$

About the base speed, an optimum ratio of approximately 3.0 between maximum and base rotation speed has been found in [16], taking into account the total costs and the motor performances (peak and continuous power, total mass, losses and average efficiency) for HEV propulsion.

$$\omega_b = \frac{\omega_{sh,Max}}{3} \qquad \text{with} \qquad \omega_{sh,Max} = \frac{\omega_{t,Max}}{i_{g,6}} \tag{50}$$

Where $\omega_{t,Max}$ [rad/s] is the maximum ICE speed (6000 [RPM]) and $i_{g,6}$ [-] the 6^{th}, and shortest gear ratio (see respective sections).
From now on, the maximum electromagnetic torque, reachable only in this region, will be called $C_{e,Max,0}$ [Nm].

Flux Weakening Operation

The transition to the flux weakening region of the mapping is made when maximum stator voltage is reached. $U_b = \sqrt{U_d^2 + U_q^2}$ [V] becomes constant and a direct-axis current I_d [A] is injected: one that generates a magnetic flux in the opposite direction of ϕ_{PM} [Wb].
The missing equation is found by keeping U_b [V] at its value in constant torque operation:

$$U_b = \sqrt{(X_q I_{q,b})^2 + (Z_s I_{q,b} + E_0)^2} \qquad \text{with} \qquad I_{q,b}(t) = \epsilon(t)\ I_{q,Max} \tag{51}$$

Where $I_{q,Max} = \frac{C_{e,Max,0}}{m_{ph}\ p\ n_c\ \phi_{PM}}$ [A] and ϵ [-] defines the actual power ratio:

$$\epsilon(t) = \frac{P_{em}(t)}{P_{e,Max}} = \frac{C_{em}(t)\ \omega_{sh}(t)}{C_{e,Max,0}\ \omega_b} \tag{52}$$

All in all, the equations system to compute in this region of operation is:

$$I_q = \frac{C_{em}\omega_{sh}}{m_{ph}\ p(E_0 + (X_d - X_q)I_d)} \quad (53) \qquad U_d = Z_s\ I_d - X_q\ I_q \quad (55)$$

$$U_q = Z_s\ I_q + X_d\ I_d + E_0 \quad (54) \qquad \sqrt{U_d^2 + U_q^2} = U_b \quad (56)$$

After resolution of the appropriate system, one has found current values of $\underline{I_{dq}}$ [A] and $\underline{U_{dq}}$ [V], from which the phase values $\underline{I_{ph}}$ [A] and $\underline{U_{ph}}$ [V] can be computed via $dq0$ transformation. Energy consumption can then be evaluated from equations at the VSI (taking into account its efficiency in motor mode $\eta_{VSI} = 0.95$ [-] in generator mode $\eta_{VSI} = 1/0.95$ [-]):

$$\underline{\hat{m}_{VSI}}(t) = \frac{\underline{U_{ph}}(t)}{U_{bus}} \qquad \eta_{VSI}\ I_{bus}(t) = \underline{\hat{m}_{VSI}}^T(t)\ \cdot\ \underline{I_{ph}}(t) \quad (57)$$

8.5 Mechanical Output

Unfortunately, the so-called electromagnetic torque C_{em} [Nm] is not perfectly output-able from the ETM, but is rather an illustration of the demand of torque by the operator. Indeed, the machine undergoes a series of losses in the transmission of power from the AC supply by the VSI to the final output at the motor shaft. Figure 27 shows a schematics of the power flow in the ETM.
DC power from the battery arrives via a DC bus maintained at constant voltage U_{bus} [V]; it is then transmitted via the VSI with its own efficiency for AC supply. Once "in" the motor, certain losses Q_{Cu} [W] are inherent to the fact that the stator winding's copper is not a perfect conductor. Magnetic transmission also is not ideal so that when arriving to the rotor, the original power is again diminished by iron losses Q_{Fe} [W]. Finally, mechanical losses Q_{WF} [W] are due to friction and the motoring of a ventilation system.

Computation of those losses is detailed by the complete thermal modeling of the ETM (following the technique initiated in [17]), provided in appendix A.3.

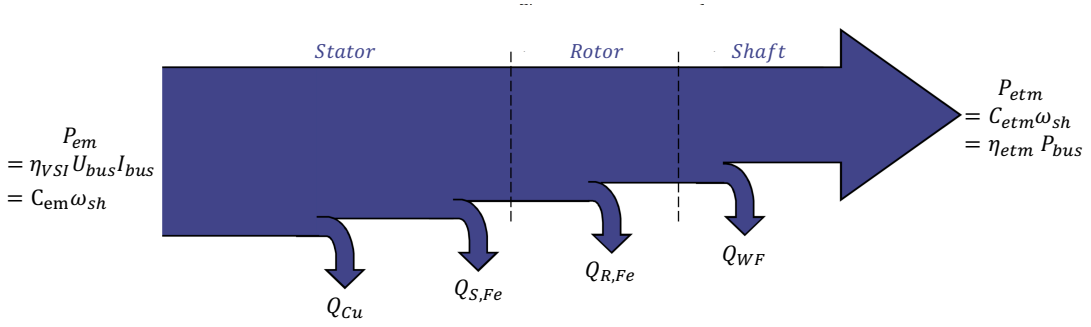

Figure 27: ETM power flow

η_{etm} [-] defines the motor global efficiency to transform the potential electromagnetic P_{em} [W] into true mechanical power P_{etm} [W].

8.6 Results

All in all, the complete model has been considerably reduced to the point that only 6 parameters (see Table 3) are necessary to fully dimension the PMSM and evaluate its performances.

p [-]	l_r [m]	R_{ir} [m]
Number of pair of poles	Rotor length	Inner rotor radius
e_{PM} [m]	R_{os} [m]	S_{Cu} [mm^2]
PM thickness	Outer stator radius	Wires cross section

Table 3: PMSM dimensional parameters

With the model exposed, experience has also shown that current density cannot really exceed 5 [A/mm^2], otherwise the temperature in the windings rises considerably, itself augmenting their resistivity (cfr. equation 130), thereby creating a fatal loop that virtually renders the motor unusable.

Thorough testing have been applied to a tri-phase ETM ($m_{ph} = 3$ [-]) dimensionally specified in Table 4 which have shown promising results - in the sense that they are physically coherent - as evidenced by Figure 29 illustrating the motor efficiency mapping and Tables 5 and 6 covering the thermal losses and temperatures (as computed by the thermal modeling described in appendix A.3) in the different parts of the machine at various operating points.

p [-]	l_r [m]	R_{ir} [m]	U_{bus} [V]	$C_{etm,max}$ [Nm]	$P_{bus,rated}$ [kW]
4	0.4	0.06	600	595	163
e_{PM} [m]	R_{os} [m]	S_{Cu} [mm^2]	$I_{bus,rated}$ [A]	ω_b [RPM]	$P_{etm,rated}$ [kW]
0.03	0.16	12	272	2500	156

Table 4: Simulated ETM specifications

For those dimensions, note that with a filling factor of 75 [%], each of the $\frac{S}{2} = 24$ [-] coils constituting the stator windings are made of $n_c = 23$ [-] turns.

In order to clearly visualize the design selected and its dimensions, Figure 28 summarizes the optimization parameters introduced above in this chapter and in the appendices.

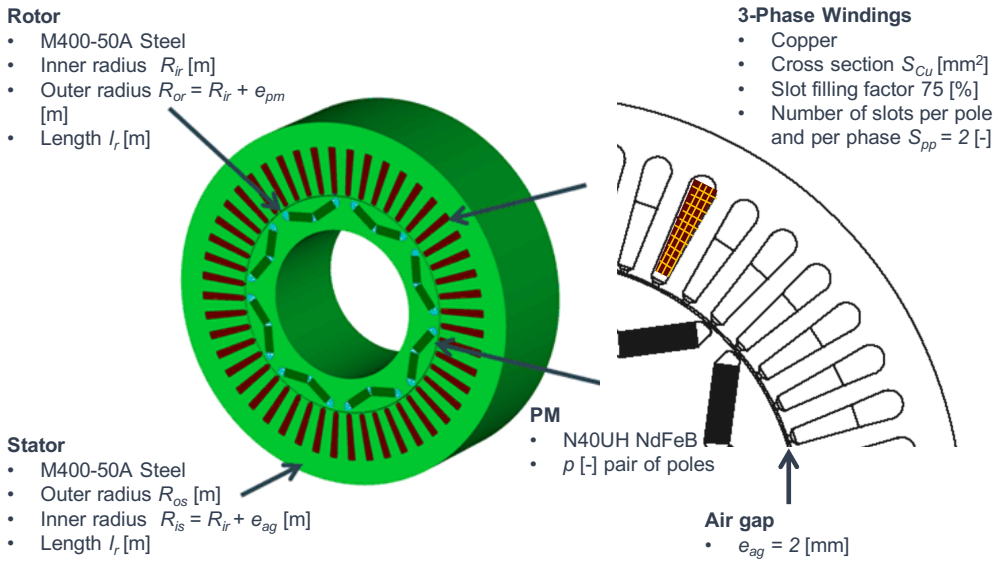

Figure 28: ETM model specifications[5]

Thermal losses

C_{etm} [Nm]	ω_{sh} [RPM]	Q_{Cu} [kW]	$Q_{S,Fe}$ [kW]	$Q_{R,Fe}$ [kW]	Q_{WF} [kW]
583.3	2550	0.757	1.082	0.386	0.657
300.5	4950	0.401	2.692	0.959	1.276
198.3	7500	0.272	4.495	1.602	1.934

Table 5: Simulated ETM thermal losses repartition

[5]Courtesy of Computer Simulation Technology, *Optimization of Torque in a Permanent Magnet Synchronous Motor (PMSM) for Traction Applications*, http://www.cst.com, 2016

Temperature profile

C_{etm} [Nm]	ω_{sh} [RPM]	T_w [°C]	T_{stator} [°C]	T_{PM} [°C]	T_{rotor} [°C]	T_{shaft} [°C]
583.3	2550	151.8	38.7	79.6	78.9	78.6
300.5	4950	104.3	50.5	126.4	125.1	124.4
198.3	7500	93.6	64.7	168.3	166.5	165.6

Table 6: Simulated ETM temperature distribution

The stator seems to remain at quite low temperatures. This is most likely due to the hypothesis of perfect external cooling: $T_{case} = T_{coolant} = T_{ambient}$ [°C]. The other values are coherent - however a little underestimated - with expectations for an ETM this powerful [17].

Motor efficiency η_{etm} [-]

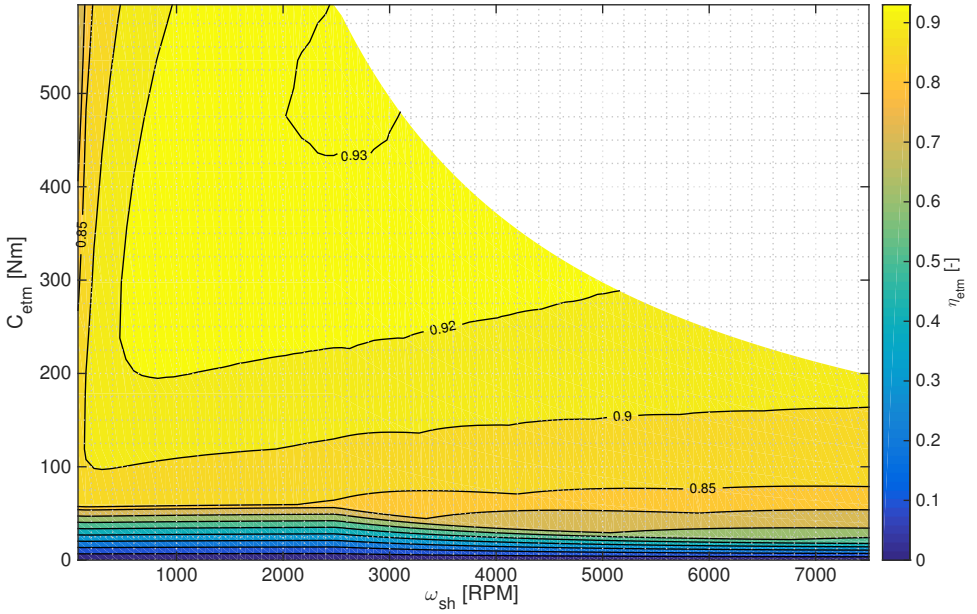

Figure 29: Simulated ETM efficiency mapping

The simulated ETM meets its aforementioned global requirements: a consequent torque is still available at $\omega_{sh,max} = 3\omega_b$ [RPM]. The efficiency mapping is also very comparable to datasheet of PMSM used for traction, while a little overestimated at lower rotation speed ω_{sh} [RPM]. What may be questioned is the flux weakening region that keeps quasi constant power output though in reality, it is most likely to fade with increasing speed.

8.7 ETM's mass

Having also all the materials' volumes constituting the dimensioned ETM, its mass m_{etm} [kg] is quite easily computed:

$$m_{etm} = m_{Cu} + m_{S,Fe} + m_{R,Fe} + m_{PM} = \rho_{Cu}\, V_{Cu} + \rho_{Fe}(V_{S,Fe} + V_{R,Fe}) + \rho_{PM}\, V_{PM} \tag{58}$$

Where $\rho_{Cu} \approx 9000$ [kg/m^3] and $\rho_{PM} = 7700$ [kg/m^3] are the copper and NdFeB magnets density respectively.

8.8 Black Box

The ETM command is obviously made via throttle k_e [-] which gives an image of the *Driver*'s demand of torque. Following the current rotation speed of the motor shaft ω_{sh} [rad/s] and thus the operating region, the demand C_{em} [Nm] is taken into account in the resolution of the corresponding system of equation.
At each time-step, the magnetic field B_{PM} [T], the windings' impedance Z_s and reactance X_{dq} [Ω] is computed with the optimized set of dimensions to optimize and following the previous profile of temperature.
The necessary supply I_{bus} [A] is evaluated and once the thermal losses are estimated, the ETM torque C_{etm} [Nm] can be outputted.

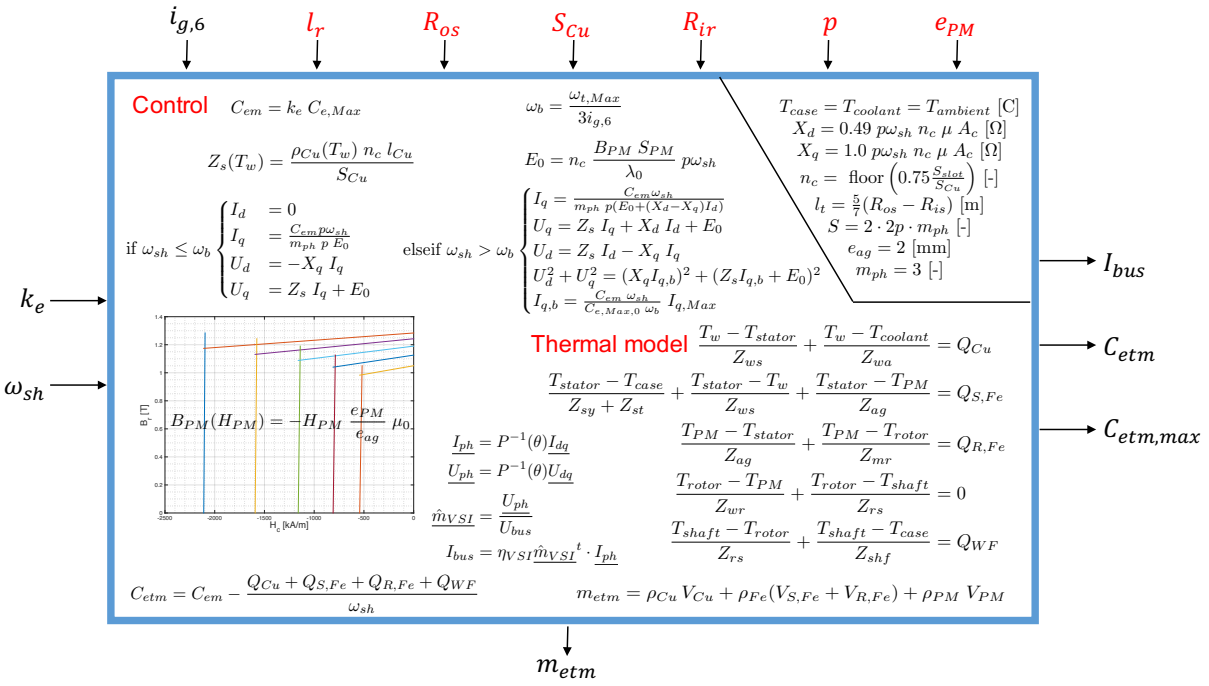

Figure 30: ETM *Black Box*

8.9 Possible Improvements

Possible refinements of the model can be a study of weaker links like vibratory effects in the ETM and thermal losses due to Eddy currents.

9 Battery Pack

9.1 Description and Modeling

A battery pack can be seen as a "grid" composed of a great number n_{cell} [-] of chemical cells; of which $n_{cell,s}$ [-] are placed in series, forming a "branch", to increase the overall open circuit voltage $U_{bat,0}$ [V] at full charge. $n_{\|}$ [-] branches are disposed in parallel to obtain the desired nominal capacity $Q_{bat,0}$ [Ah]. The battery's internal - considered constant - resistance R_{bat} [Ω] is logically computed as a parallel disposition of $n_{\|}$ branches, each made of of $n_{cell,s}$ cells of individual resistances R_c placed in series.

$$n_{cell} = n_{\|} n_{cell,s} \qquad U_{bat,0} = n_{cell,s} U_{c,0} \qquad Q_{bat,0} = n_{cell} Q_c \qquad R_{bat} = \frac{n_{cell,s}}{n_{\|}} R_c \tag{59}$$

Where $U_{c,0}$ [V] and Q_c [Ah] designate the open circuit voltage and internal capacity of one cell respectively.

Knowing that, the current in one cell (i.e. in one branch) is easily calculated for a direct current I_{bat} [A] subtracted (or supplied) to the battery by the motor (generator):

$$I_c(t) = \frac{I_{bat}(t)}{n_{\|}} \tag{60}$$

As mentioned in the *Power Split Device* (PSD) section, algorithms for managing the motors' load and the battery itself need a precise and quick computation of the current state of charge (SOC) variation (and resulting change in open circuit voltage), power and capacity fade as well as the instantaneous available power. In order to obtain this, an accurate cell model is necessary, of which multiple forms are reviewed in [18] and [3].

HEV applications constitute a very harsh environment due to highly dynamic rate profile (i.e. quick changes in demand / supply of power), in frequency and amplitude, in comparison with, for instance, small order, quasi constant power demand in smartphone applications. Taking this into account, the conclusion of authors Wang, Zhang and Chen in [3] is the use of a switching multi-model implementation to compare results from different equations in order to grant a better robustness of the battery management system (BMS). However, the purpose of this master thesis being pure simulation, one-type modeling of the battery SOC evolution should suffice to provide precise theoretical results.

The choice for most suitable model for SOC and individual cell voltage U_c [V] evaluation was based on the experiments in [3]. The various mathematical evaluation methods of one battery cell c are:

The Shepherd Model (SM)

$$U_c(t) = U_{c,0,SM} - R_{c,SM} I_c(t) - \frac{k_{c,0,SM}}{SOC(t)} \tag{61}$$

The Universal Model (UM)

$$U_c(t) = U_{c,0,UM} - R_{c,UM} I_c(t) - k_{c,0,SM}(1 - SOC(t)) \tag{62}$$

The Nernst Model (NM)

$$U_c(t) = U_{c,0,NM} - R_{c,NM} I_c(t) + k_{c,0,NM} \ln(SOC(t)) + k_{c,0,NM} \ln(1 - SOC(t)) \tag{63}$$

The Combined Model (CM)

As its name implies, this model is a combination of the three electrochemical equations above (61), (62), (63).

$$U_c(t) = U_{c,0,CM} - R_{c,CM} I_c(t) - k_{c,0,CM} SOC(t) - \frac{k_{c,1,CM}}{SOC(t)} + k_{c,2,CM} \ln(SOC(t)) + k_{c,3,CM} \ln(1 - SOC(t)) \tag{64}$$

The various coefficients $k_{c,i,j}$ [V] ($i \in \{0,1,2,3\}$ and $j \in \{SM, UM, NM, CM\}$) take different values following the battery type - generally specified by manufacturers in their datasheet, or identified empirically

via the recursive least squares method. All models take $SOC(t)$ as its physical definition (I_{bat} being a time-varying DC current: positive values charging the battery, and negative values discharging it):

$$SOC(t) = SOC(t_0) + \int_{t_0}^{t} \frac{\eta_c I_{bat}(\tau) d\tau}{Q_{bat,0}} \tag{65}$$

With the coulombic efficiency $\eta_c \approx 1/0.95$ [-] in discharge and $\eta_c \approx 0.75$ [-] in charge.

The test led in [3] was about discharging different types of battery at constant discharge current I_{bat} [A]. Based on the definition (65), the battery SOC is then supposed to decrease linearly. Figure 31 shows the SOC real value's evolution during the discharge compared to the results computed via the different aforementioned methods.

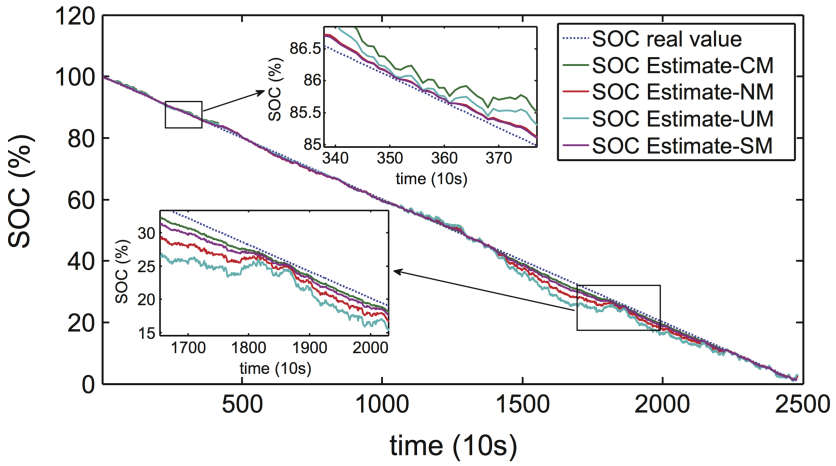

Figure 31: Comparison of SOC estimation results [3]

The root-mean square errors (RMSE) as well as program execution times (PET) - program run on small embedded field-progammable gate array (FPGA) - are plotted in Figures 32 and 33 respectively, for a better analysis of the different models regarding precision and real-time performance.

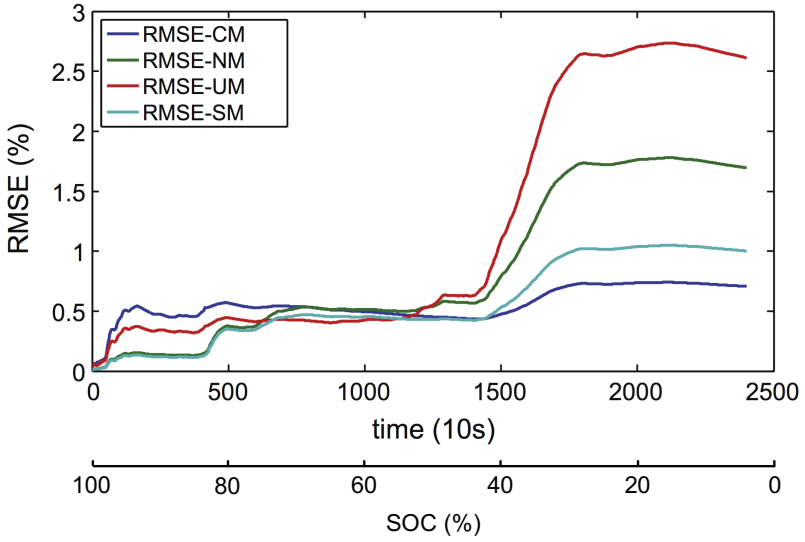

Figure 32: Comparison of SOC estimation models' RMSE [3]

After study of those figures and of the available processing power, it has been judged that the combined model, however a bit more time-consuming than the SM or the NM, should provide the best results - SOC real values for vehicle's battery management system (BMS) and PSD operation.

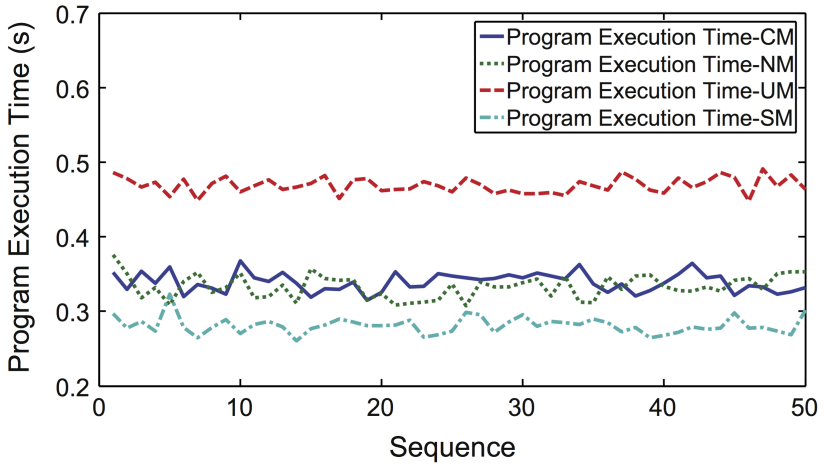

Figure 33: Comparison of cell voltage estimation models' PET [3]

Supposing that all battery cells are discharged at the same rate, the behaviour of one cell reflects the whole battery evolution; equation (65) gives the overall battery SOC and (66) is assumed to be true.

$$U_{bat}(t) = n_{cell,s} U_c(t) \tag{66}$$

9.2 Current Limitations

With this equation and (64), emphasis is brought to the fact that current I_{bat} [A] can deeply impact the dynamical output voltage U_{bat} [V] of the battery, and so, behaviour of the power electronics and ultimately, the one of the ETM. It is then limited so that, even in the worst case scenario (i.e. $SOC = 20$ [%], cfr. typical discharge curves like 34) U_c [V] does not fall under 50% of its last value.

$$I_{bat,Max} = n_{\parallel} I_{c,Max} \qquad \text{so that} \qquad \frac{U_c(t) - U_c(t+\Delta t)}{U_c(t)} \overset{(64)}{<} 0.5 \text{ with } SOC = 0.2 \tag{67}$$

9.3 Battery Pack's Mass

The casing and the interconnections being supposed to have negligible masses in front of the cells, the total mass of the battery pack is simply:

$$m_{bat} = n_{cell} m_{cell} \tag{68}$$

9.4 Battery type

The battery cell type chosen to "equip" the simulation vehicle is of Li-Ion rechargeable IFP1865140A-9. These have indeed a density of power very well suited for HEV applications.
The values for the CM parameters of this type of cell are compiled in Table 7 according to calibration [3] and manufacturer's specifications[6].

$U_{c,0}$	=	3.5120	[V]	Q_c	=	9.2	[Ah]
m_{cell}	=	332	[g]	R_c	=	0.0134	[Ω]
$k_{c,0}$	=	0.0004	[V]	$k_{c,1}$	=	0.2759	[V]
$k_{c,2}$	=	0.1532	[V]	$k_{c,3}$	=	-0.0313	[V]

Table 7: Data and calibration parameters for Combined Modeling of an IFP1865140A-9 cell

[6] Among others, developed by Hefei Guoxuan High-Tech Power Energy Co., LTD

Resolution of the implemented combined model (64) of this type of battery is shown in Figure 34 where, despite its (limited) errors, typical discharge curves are recognizable.

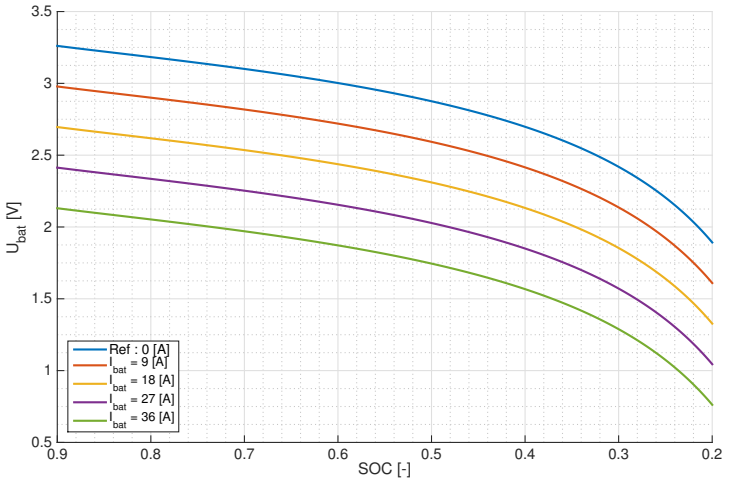

Figure 34: Discharge curves of an IFP1865140A-9 cell obtained via combined modeling

9.5 Black Box

The *Black Box* summary of the methodology described above is shown in Figure 35. $U_{bat,0}$ [V] is chosen a priori via optimization as it fixes the functioning voltage of the ETM. The overall capacity of the battery $Q_{bat,0}$ [Ah] is either an optimization parameters or adapted "in the *box*" in order to have a round number $n_{\parallel}$ [-] of branches, each composed of $n_{cell,s}$ [-] cells.
I_{bat} [A] is the intensity of electrical current demanded by the *Electric Traction Motor* to satisfy the *Driver*'s throttle output (see respective sections), nevertheless limited for managed depth of discharge.
The instantaneous battery voltage U_{bat} [V] is computed as a series of $n_{cell,s}$ [-] identically discharged cells at U_c [-], and the total mass is the sum of all individual cell's m_c [kg].

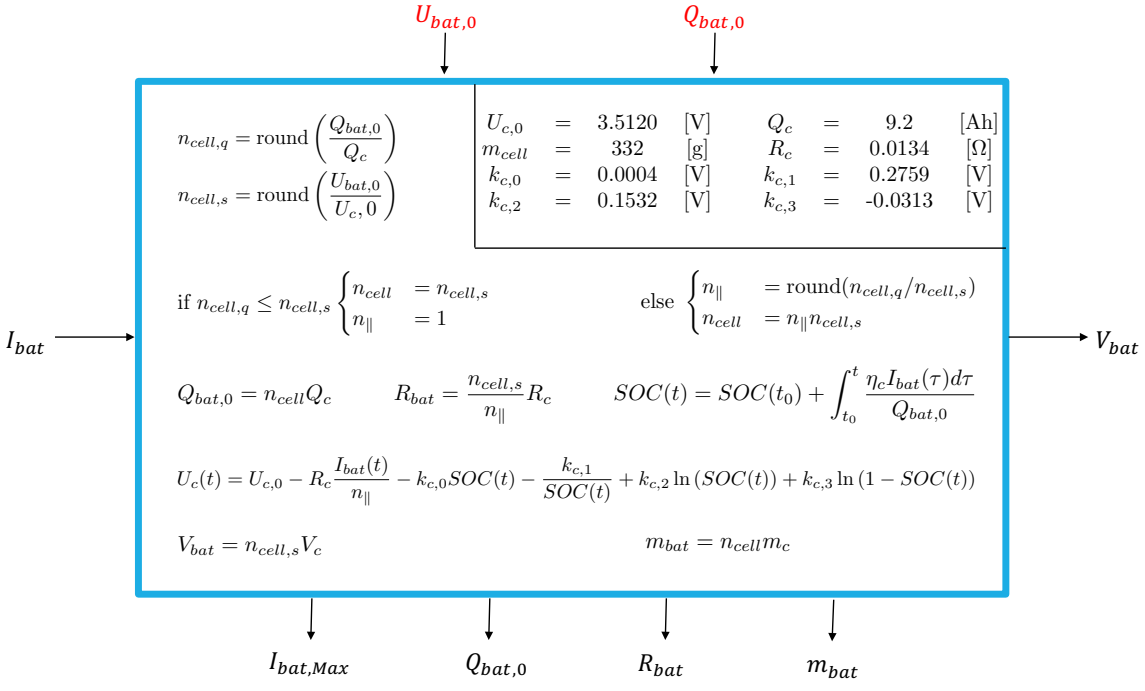

Figure 35: *Battery* Black Box

10 Power Electronics

As mentioned in previous sections, a certain amount of electronics is necessary to control the good operation of the battery and eventually, the electric traction motor. As both are power devices, the electronic management of their current intensity and voltage is designated by "power electronics". When one knows that a battery exchanges DC electrical quantities, it directly appears the necessity of a DC/AC inverter to supply the ETM. What may be less clear, is the request for a DC/DC converter between the battery and the inverter; the latter being able to deal with variation in its input DC voltage. However, keeping a constant operating voltage at what is called a DC bus allows to maintain constant torque range and power capability, to reduce damaging current ripple towards the battery and to ease the transitions between motoring and regenerative braking.

10.1 Three-Phase Voltage Source Inverter

Voltage source inverters (VSI) are the "closest" electronic device to the ETM as they directly manage its voltage frequency - hence, its rotation speed. In order to achieve this, pulse width modulated signals (PWM) control 6 insulated-gate bipolar transistors (6 IGBTs for high, 3-phase power applications - see Figure 36) for them to generate a sinusoidal AC output voltage on each phase.

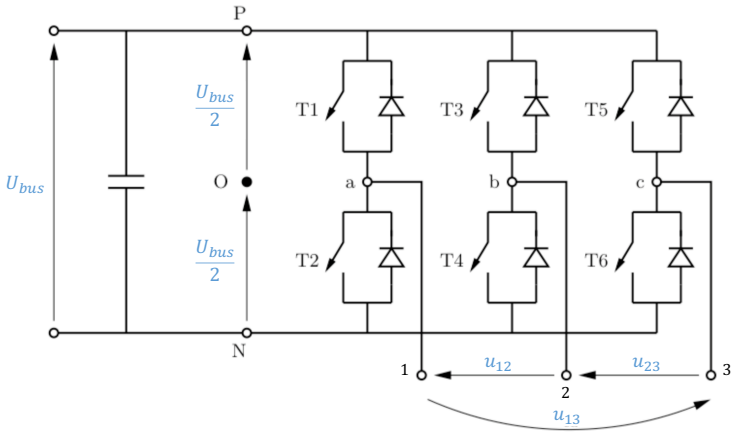

Figure 36: Three-phase VSI basic circuit

The switching frequency ([kHz] order) is not discussed in this work as the time-step used to discretize the vehicle simulation would simply not allow to make any difference. But it has to be noted that the general tendency is about lower frequency for higher power management, therefore lowering the switching losses but eventually raising the current and torque ripples.

The very simple model used in this work to describe this piece of equipment was already introduced in section 8 about the ETM. It consists in monitoring the 3 modulating signals $\hat{m}_{VSI,j}(\mathrm{t})$ ($j \in \{1,2,3\}$ for each phase) and assuring symmetry of the system and linear modulation ($\hat{m}_{VSI,j}(t) < \frac{\sqrt{3}}{2\sqrt{2}}$). Over-modulation ($\hat{m}_{VSI,j}(t) < \frac{\sqrt{3}}{2\sqrt{2}}$) would indeed introduce lower-order harmonics in the current of which real impacts would not be taken into account since this simulation does not cover the response of the system to such harmonics. An illustration of the PWM control in linear modulation is shown on Figure 37 [19].

10.2 Bidirectional DC/DC Buck-Boost Converter

The principal function of a boost converter is, as its name suggests, to raise the relatively low (according to the number of cells, hence the battery mass) U_{bat} [V] to the ETM operating voltage. Current technologies are indeed best driven when supplied by voltages around 600 [V]. Of course, when the ETM acts as a generator, power flows from the motor drive to the battery and the DC/DC converter must work in buck mode, lowering U_{bus} [V] to the battery requirements. This is called bidirectionality of the converter.
A basic configuration of such an electronic device in its non-isolated form is presented in Figure 38.

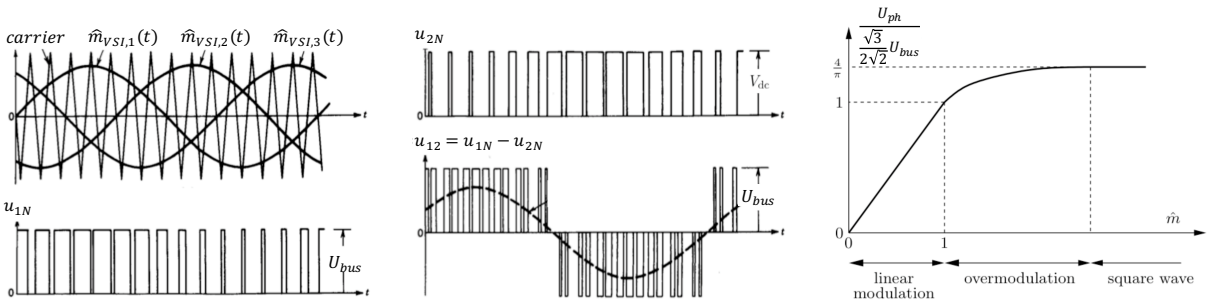

Figure 37: Pulse width modulation principle

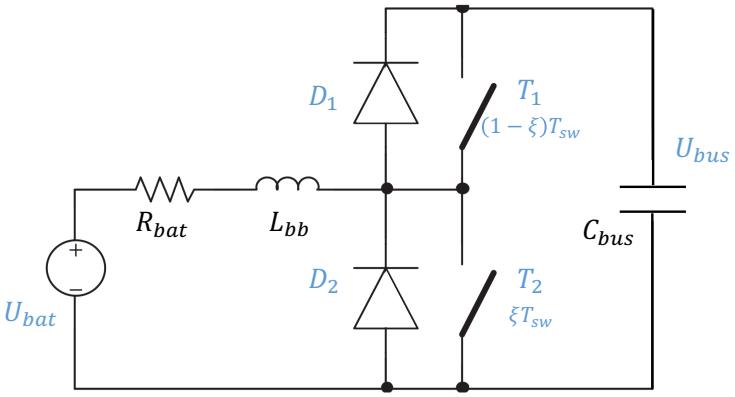

Figure 38: Bidirectional DC/DC converter basic topology

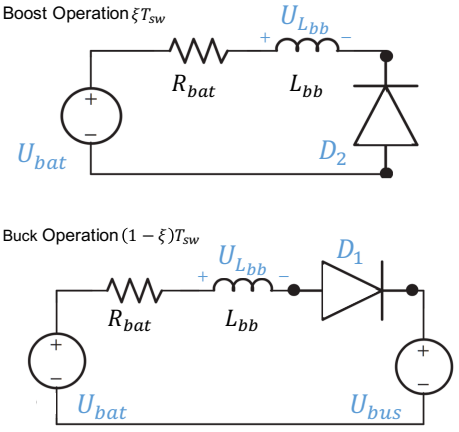

Figure 39: Buck-Boost operation

The capacitor C_{bus} [F] role at the DC bus is to smoothen the current ripples towards the battery. ξ [-] and $(1-\xi)$ [-] are the duty ratios (percentage of one cycle T_{sw} [s] during which the transistor is on) and are generally opposed to prevent short circuit (if both transistors are switched simultaneously). In practice, $\xi \in [0.2\ ;\ 0.7]$ [-] to avoid any malfunctioning.

Assuming ideal components, the two modes of operation of the device are shown on Figure 39. Also, inductor L_{bb} [H] sees its mean voltage $U_{L_{bb}}$ [V] remain constant over time. Thus, neglecting voltage drop at the diodes D_1 and D_2 (≈ 0.7 [V] very light compared to U_{bat} and U_{bus} [V]), one can compute $U_{L,boost} + U_{L,buck} = 0$ [V]:

$$\xi T_{sw}\ U_{bat} + (1-\xi) T_{sw}\ U_{bat} = 0 \tag{69}$$

$$\Leftrightarrow U_{bus} = \frac{1}{1-\xi}\ U_{bat} \tag{70}$$

Thus giving the transfer function, and the voltage gain (the current gain being the inverse for power conservation), of the bidirectional DC/DC converter. Gain that must be handled, by a proportional-integral (PI) controller, through the duty ratio ξ [-] in order to keep U_{bus} [V] constant even in case of voltage drop at the battery.

Constant Torque Range

Section 9 exposed the link between battery SOC, demand of current for ETM torque output, and voltage drops at the battery. Without a bidirectional converter between the battery and the inverter, any of those voltage drops will badly impact the performances of the ETM, making it difficult to maintain constant torque operation.

Current Ripple

As aforementioned, the switching functions at the inverter may introduce current harmonics on the DC side. Ideally, those high-frequency current ripples are smoothened by a low C_{bus} [F]. But actually, flowing into R_{bat} [Ω], they may induce damaging variations in U_{bat} [V] supposed to be constant.

Regenerative Braking

Similarly, brutal variations in the ETM torque output, like transition from motoring to regenerative braking, will cause dramatic changes in U_{bus} [V] significantly complicating vector control of the generator/motor. A DC bus voltage maintained constant or quasi-constant via a PI controlled converter will make regenerative braking far easier to handle [15].

10.3 Black Box

The PI controller mentioned tweaks the duty ratio ξ [-], at each time-step Δt [s], by monitoring the error on the bus voltage U_{bus} [V] regarding its reference value $U_{bus,ref}$ [V]. This precise value is based on the rated open circuit battery voltage $U_{bat,0}$ [V] which is optimized for the whole electric powertrain operation.
Following the demand (ETM in motor mode) or supply (ETM in generator mode) in current I_{bus} [A] at the DC bus, the respective discharge or charge of the battery does not have the same efficiency. This efficiency is exposed in converter's datasheet and usually around 95 [%] in boost and 90 [%] in buck mode.

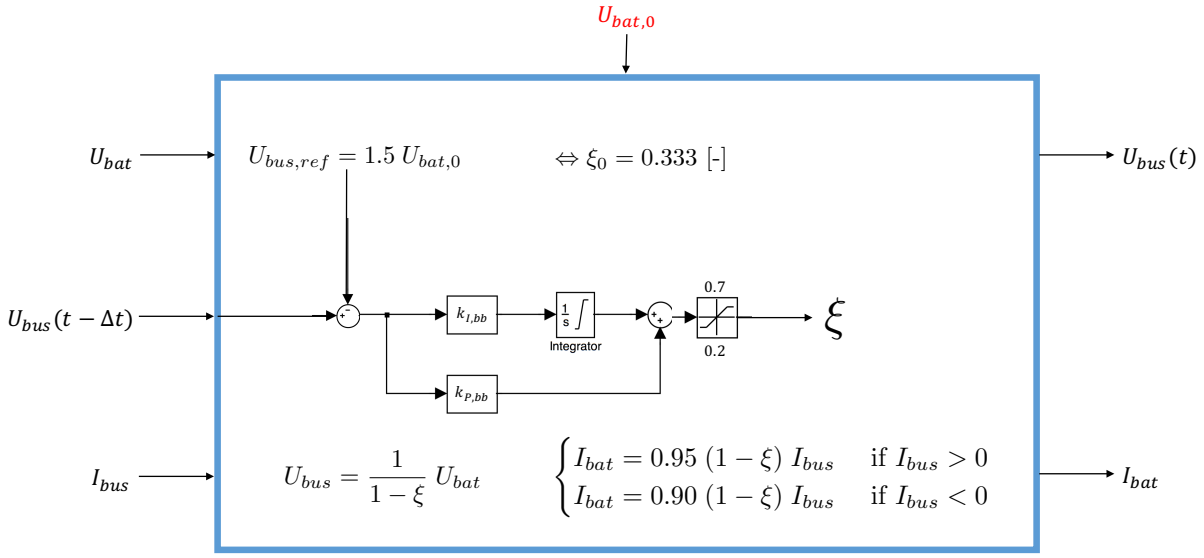

Figure 40: Bidirectional DC/DC converter *Black Box*

11 Internal Combustion Engine

Most of the modeling process described in this chapter is directly taken from the works of Pr. Hervé Jeanmart [20] (UCL) and Pr. Lino Guzzella [21] (ETH).

11.1 Model Limitations

Today's engines are very complex systems. Indeed, persisting for now more than 150 years, the internal combustion engine (ICE) has had time to evolve, to be suited for automobile vehicle's propulsion; and the late drive of the car industry to constantly reduce toxic and particularly CO_2 emissions has led to numerous technical innovations that have well boosted its efficiency, but also complicate the overall system simulation. For the achievement of this master thesis, the available processing power was limited. For the global optimization of a hybrid vehicle already heavily parametrized, it has thus been decided to "strip down" the engine to its most basic function.
The ICE chosen to alternatively propel the vehicle under study is thus an atmospheric petrol, fixed timing spark ignition (SI), engine with indirect injection at fixed valve timing.
It will not be question here of exhaust gas recirculation (EGR), variable valve timing (VVT) turbocharging, water injection, etc - all designed in today's context for better efficiency and emissions reduction. In fact, this work does not at all focus on internal combustion residual emissions. Chemical reactions could have been calculated, but as it will be exposed further, a simple ICE model allows only limited influence on exhaust gas composition.
Moreover, structural disposition of the engine's cylinders will also not be discussed in this paper as the process of global optimization varies continuous dimensional parameters' values only.
All in all, the simplicity of the model considered is also justified by sort of a consistency with other subsystem's models, as it would be incoherent for it to monopolize most of the available processing power while the other vehicle's part are simplified to extreme.

In conclusion, and as precised previously, direct results of this simulation work are not to be taken as real applicable values; but the accent has to be put on the methodology which, hopefully, can be enriched in future works by more advanced modeling.

11.2 Engine Breathing

Volumetric efficiency

To present an internal combustion engine in its simplest way, one can describe it as a volumetric machine, swallowing gas and air in order to produce a useable work. This work obviously depends on the quantity of air that penetrates in a cylinder. To quantify the filling of the cylinder, the volumetric efficiency r [-] is defined as the ratio between the mass of air-fuel mixture m_{mix} [kg] and the maximum mass admissible in the cylinder if it was at normal conditions of pressure and temperature:

$$r = \frac{m_{mix}}{\rho_0 V_{cc}} \tag{71}$$

ρ_0 [kg/m^3] is thus the air density in normal conditions, and V_{cc} [m^3] the capacity of one cylinder.

$$T_0 = 298.15 \text{ [K]} \qquad p_0 = 101325 \text{ [Pa]} \qquad \rho_0 = \frac{p_0}{R_{air} T_0} = 1.1837 \text{ [kg/m}^3\text{]} \tag{72}$$

$$V_{cc} = \pi \left(\frac{B}{2}\right)^2 C \text{ [m}^3\text{]} \tag{73}$$

With $R_{air} = 287.1$ [J/(kg $\cdot$ K] the specific air constant, B [m] is one cylinder's bore and C [m] the stroke. Hybridization having also the objective of engine downsizing, C/B ratio is chosen at 0.8, which assures a slightly short stroke in order to, hopefully, achieve higher power density and engine speed.

The quantity m_{mix} [kg] penetrates in the cylinders thanks to the valve breathing of the engine. The whole process combines thermodynamic and fluids mechanics phenomena and is described in appendix B.1.

The mass of fuel m_ϕ [kg] admitted in one cylinder over one cycle (720 [°] of crank angle) is thus:

$$m_\phi = \frac{m_{mix}}{1 + m_{a,1}/\phi} \tag{74}$$

$m_{a,1} = 14.7$ [$\text{kg}_{air}/\text{kg}_{CH_{1.8}}$] the ratio of air quantity regarding the fuel mass for stoichiometric combustion.

Figure 41, for example, gives a mapping of that mass m_ϕ [g] admitted in one of the 4 cylinders of the engine dimensionally specified in Table 8.

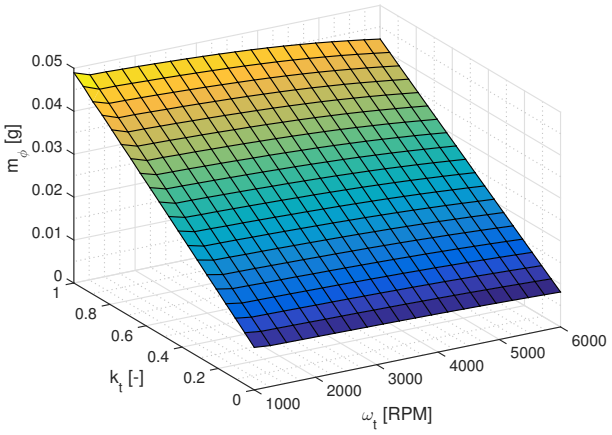

Figure 41: Admitted fuel mapping

n_{cyl} [-]	B [cm]	C [cm]	V_{cc} [cc]
4	10	8	2513

$\theta_{i,o}$ [°]	$\theta_{i,c}$ [°]	$\theta_{e,o}$ [°]	$\theta_{e,c}$ [°]
360	540	140	360

Table 8: Example engine specifications

The mass of fuel admitted in the cylinder (max. 0.0477 [g]) is there, and as expected, a linear evolution of the throttle k_t [-] with a slight diminution of the volumetric efficiency remarkable at higher speeds. This diminution is due to the fact that natural aspiration is not fast enough to fill the cylinder properly at those speeds.

Pumping Work

Nevertheless, non-perfect volumetric efficiency is not the only factor that can diminish the thermal energy $Q = m_\phi LHV$ [J] contained in m_ϕ [kg] ($LHV = 43$ [MJ/kg] the lower heating value of gasoline). Indeed, indicated mean pressure p_{mi} [Pa] is usually defined as:

$$p_{mi} = \frac{\eta_{ti} Q}{V_{cc}} - p_{mp} \tag{75}$$

Where $p_{mp} = W_p/V_{cc}$ [Pa] describes the pumping work W_p [J] necessary to admit fresh air-fuel mixture in and to put smokes out of the cylinder, by unit of cylinder capacity V_{cc} [m^3].

$$W_p = \int_{\theta_{i,e}}^{\theta_{i,e}} p_c \, dV_c - \int_{\theta_{i,o}}^{\theta_{i,c}} p_c \, dV_c \tag{76}$$

Pumping work being positive during exhaust as the pistons produce work on the smokes to put them out. As on the other side, during intake, a suction effect produced by the lowering of the piston in the cylinder facilitates entering for the air-fuel mixture.

V_c [m^3] is the available volume in the cylinder which varies with rotation of the crankshaft [22]:

$$V_c(\theta) = \frac{V_{cc}}{2}\left(1 - \cos(\theta) + \beta - \sqrt{\beta^2 - \sin(\theta)^2} + \frac{2}{\tau - 1}\right) \tag{77}$$

With β [-], the ratio between rod length and the crank radius (i.e. half of the stroke's length), is taken at approximately 3 [-] to obtain a piston movement in the cylinder apparently uniformly accelerated.
The compression ratio $\tau = V_{BDC}/V_{TDC}$ [-] is here limited to 11 even though it maximizes efficiency. Indeed, higher ratios require several adjustments such as VVT, ignition timing delaying systems and high octane leaded gas to prevent knock (which would not be observable in this work as flame propagation is not simulated).

A mapping of the pumping work for the engine described in Table 8 is given in Figure 42.

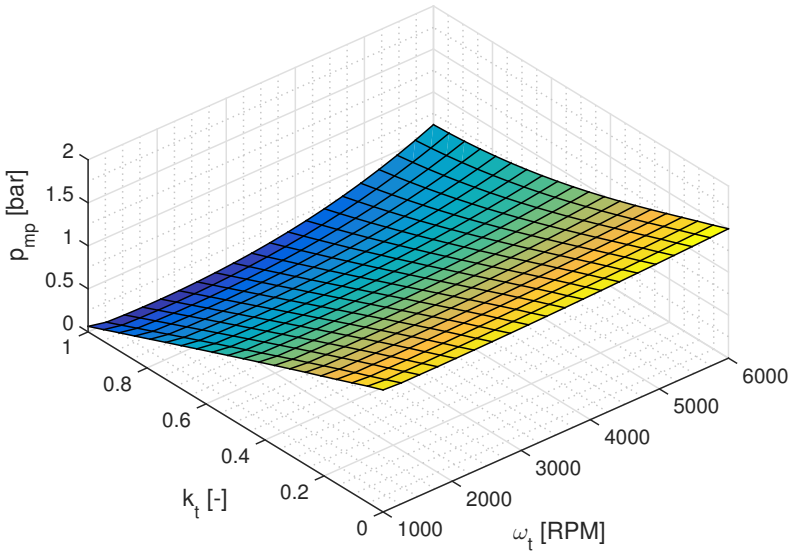

Figure 42: Pumping work mapping

Regarding the throttle k_t [-], obviously, the suction effect described above is disfavoured for a more closed butterfly valve (i.e. a lower throttle k_t - Imagine sucking into an obstructed straw). On the other hand, regarding the rotation speed, mass flows $\dot{m}_{f,i}$ and $\dot{m}_{f,e}$ [kg/s] are logically augmenting frequency. All other values remaining the same in equation (165), $p_{nt} = p_c$ [Pa] is decreased at intake and $p_i = p_c$ [Pa] is increased at exhaust, overall pumping work being thus raised with increasing speed following (76). All in all, this gives a negative pumping work between 0.0 and 1.504 [bar].

11.3 Compression and Expansion Strokes

In order to complete equation (75), there is still a need of a clear definition for the internal thermodynamic efficiency η_{ti} [-] which gives the transformation yield between thermal energy Q [J] and mechanical work W_m [Nm] or [J]:

$$\eta_{ti} \triangleq \frac{W_m}{Q} \tag{78}$$

The ICE being a volumetric machine, its mechanical work is expressed as:

$$W_m = \int_{0^\circ}^{180^\circ} p_c \, dV_c - \int_{540^\circ}^{0^\circ} p_c \, dV_c \tag{79}$$

W_m [Nm] being positive in expansion and negative in compression. The expansion work is obviously greater due to ignition of the air-fuel mixture contained in the cylinder.
The evolution of the pressure p_c [Pa] inside the cylinder during compression and expansion strokes is described as a function of the crank angle θ [°] [20], and depending on the ignition timing θ_s [°]. This function is developed in appendix B.2 and gives results such as Figures 44 and 43 for, again, the engine parametrized in Table 8 with a fixed ignition timing at $\theta_s = -15$ [°].

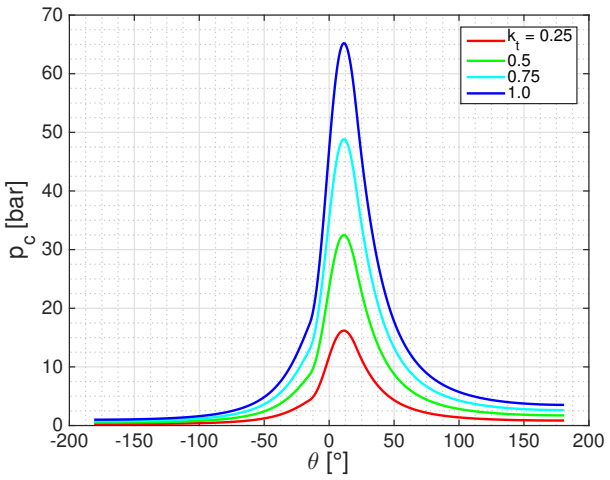

Figure 43: Evolution of internal pressure as a function of throttle

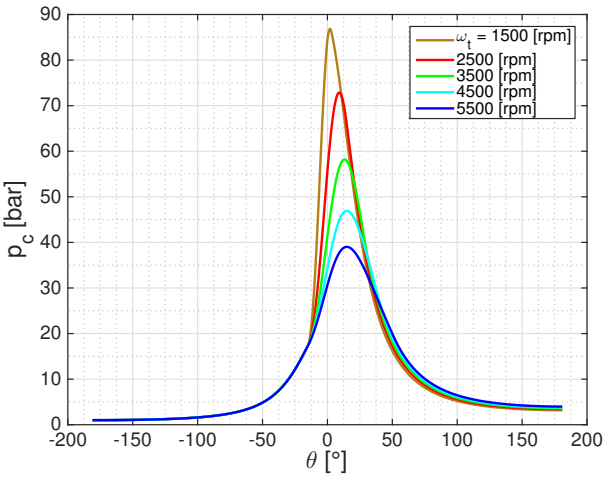

Figure 44: Evolution of internal pressure as a function of speed

The rise in pressure is clearly observable as soon as ignition starts.

Internal Thermodynamic Efficiency η_{ti}

The internal thermodynamic efficiency η_{ti} [-] (max. 43.24 [%] at full throttle and around 3000 [RPM] for the example engine) that limits the transformation of thermal energy into mechanical work via equation (78) can finally be displayed on Figure 45 shows the mapping of this efficiency.

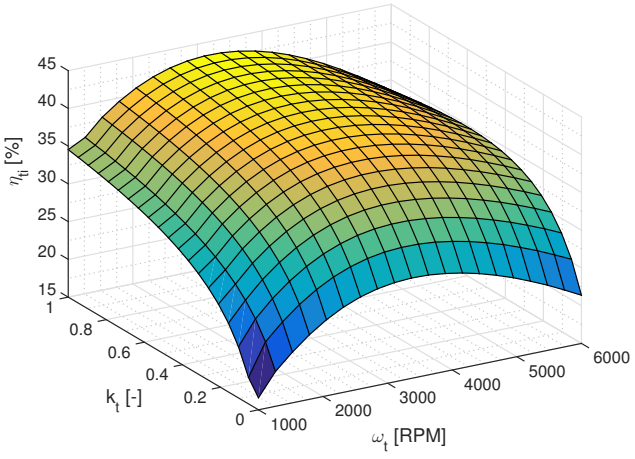

Figure 45: Internal thermodynamic efficiency mapping

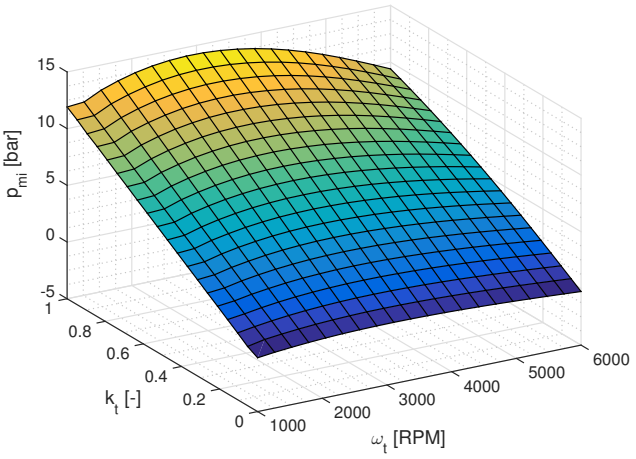

Figure 46: Indicated mean pressure mapping

Indicated Mean Pressure p_{mi}

All together in equation (75), the indicated mean pressure p_{mi} [bar] can be computed as a mapping of the throttle k_t [-] and the engine speed ω_t [RPM] as shown on Figure 46. $p_{mi,max} = 14.24$ [bar] is obviously reached at the same operating point as $\eta_{ti,max}$ [-], i.e. around 3000 [RPM].

11.4 Friction

But this ultimately does not give the energy output p_{me} [Pa] (for mean effective pressure) of the engine as p_{mi} [Pa] is still reduced by friction between the pistons and the cylinders' walls, between the crankshaft and its bearing, also for the actioning of the valves, etc.

$$p_{me} = p_{mi} - p_{mf} \tag{80}$$

The friction model for the computation of mean friction pressure p_{mf} [Pa] presented here is the one developed at the ETH Zurich by Martin Stöckli and its team in 1989 [21]:

$$p_{mf} = k_{f,1}(T_{wall})\ (k_{f,2} + k_{f,3}\ C^2\ \omega_t^2)\ \Pi_{t,max}\sqrt{\frac{k_{f,4}}{B}} \tag{81}$$

Which thus evolves as a quadratic relation of the engine speed ω_t [rad/s].
While $\Pi_{t,max}$ [-] represents the maximum boost ratio for which the engine is designed to operate at low speeds, taken at 1 for a naturally aspirated engine, factors $k_{f,i}$ ($i \in \{1,2,3,4\}$) are given in Table 9 with a dependency of $k_{f,1}$ [Pa] on the engine temperature T_{wall} as shown on Figure 47.

	SI	Diesel	
$k_{f,1}(T_{op})$	$1.44 \cdot 10^5$	$1.44 \cdot 10^5$	[Pa]
$k_{f,2}$	0.46	0.50	[-]
$k_{f,3}$	$9.1 \cdot 10^{-4}$	$1.1 \cdot 10^{-3}$	[s^2/m^2]
$k_{f,4}$	0.075	0.075	[m]

Table 9: Parameters of the ETH friction model

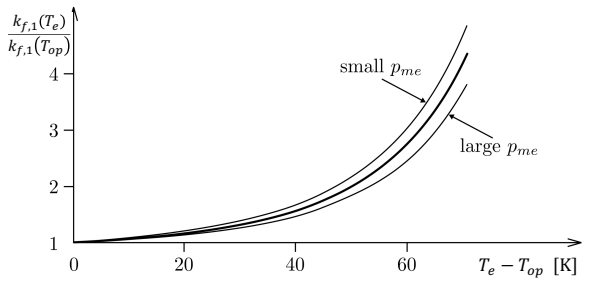

Figure 47: Temperature dependency of mechanical friction in ICE

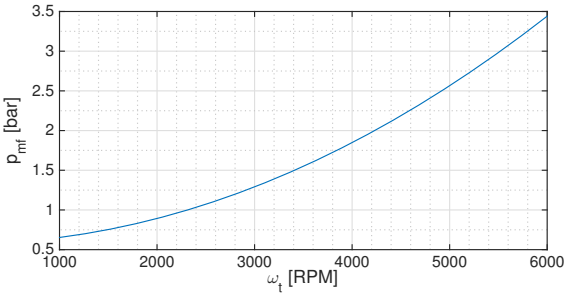

Figure 48: Mean friction pressure as a function of engine speed

As mentioned previously, the cylinders' walls of the ICE are considered to be perfectly cooled and maintained at constant operating temperature $T_{wall} = T_{op}$ [K] of a "pre-heated" structure.

Mean friction pressure p_{mf} [bar] is shown on Figure 48 as a function of the engine speed.

Mean Effective Pressure p_{me}

Having computed the whole model, a mapping of the mean effective pressure p_{me} [bar] (max. 13.06 [bar] at 2600 [RPM]) can be displayed on Figure 49.
Giving that the *pme* is the mechanical work density ([Pa] = [J/m^3]) taken out of one cylinder over one cycle, the ICE power P_{ice} [W] and therefore torque output C_{ice} [Nm] can be calculated as:

$$P_{ice} = p_{me}\ n_{cyl} V_{cc}\ \frac{1}{2}\frac{\omega_t}{2\pi} \qquad\qquad C_{ice} = \frac{P_{ice}}{\omega_t} \tag{82}$$

Where n_{cyl} [-] cylinders produce useable work for every 2 engine rotations. Note that, in practice, in order to avoid the cylinders from taking any disproportionate dimensions, n_{cyl} [-] is chosen according to the optimized value for the total displacement $V_{cc,tot}$ [l]:
The values in Table 10 have been established following thorough research on the internet and specialized magazines.

Both torque ($C_{ice,max}$ = 261.1 [Nm] at 2600 [RPM]) and power output ($P_{ice,max}$ = 99.92 [kW] at 4400 [RPM]) are shown on Figures 50 and 51 for the example engine (cfr. Table 8).

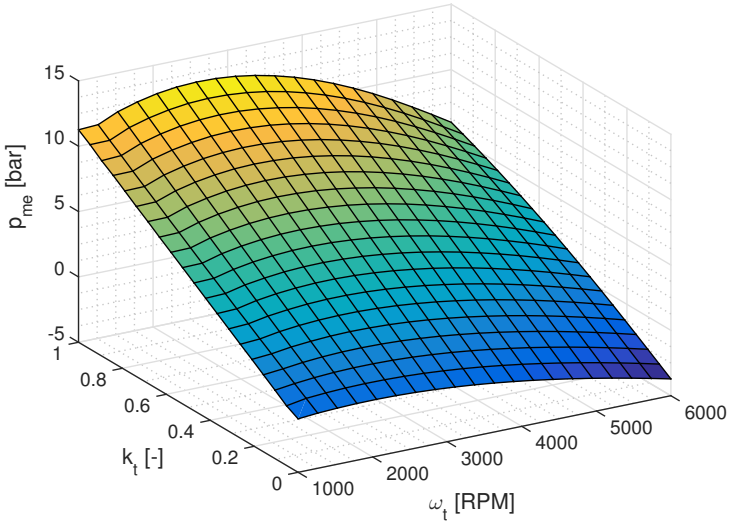

Figure 49: Mean effective pressure mapping

$V_{cc,tot}$ [l]	$\in [0.5\ ;\ 0.8[$	$\in [0.8\ ;\ 1.2[$	$\in [1.2\ ;\ 1.4[$	$\in [1.4\ ;\ 2.2[$	$\in [2.2\ ;\ 2.6[$
n_{cyl} [-]	1	2	3	4	5
$V_{cc,tot}$ [l]	$\in [2.6\ ;\ 3.8[$	$\in [3.8\ ;\ 4.6[$	$\in [4.6\ ;\ 5.2[$	$\in [5.2\ ;\ 6.5[$	$\in [6.5\ ;\ 8.2]$
n_{cyl} [-]	6	8	10	12	16

Table 10: Usual number of cylinders regarding the displacement in passengers cars' engines

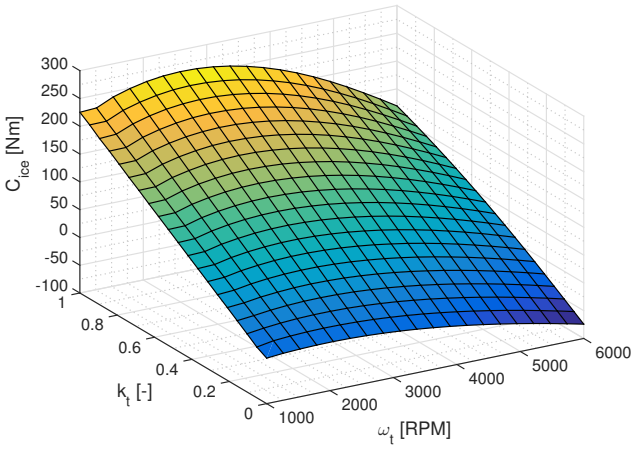

Figure 50: ICE output torque mapping

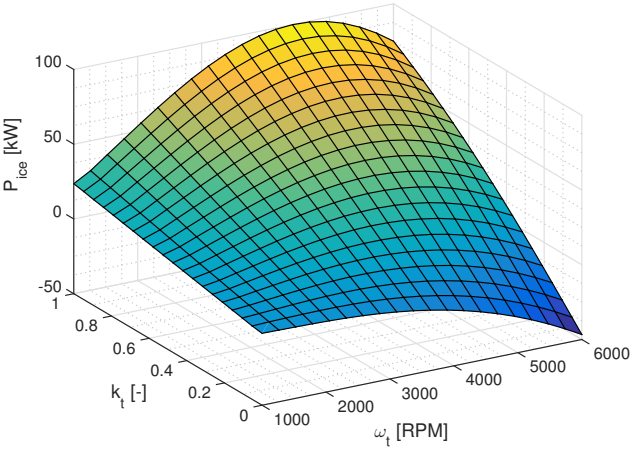

Figure 51: ICE power output mapping

Brake Specific Fuel Consumption

A final interesting value for the characterization of an ICE is its brake specific fuel consumption or $BSFC$ [g/kWh] giving the amount of fuel needed to output useable work following its operating point.

$$BSFC = \frac{1000\,\dot{m}_\phi}{P_{ice}/3600} = \frac{m_\phi\ \omega_t/(4\pi)}{P_{ice}} 3.6\ \cdot\ 10^6 \tag{83}$$

A BSFC map for the engine described by table 8 is shown in Figure 52.

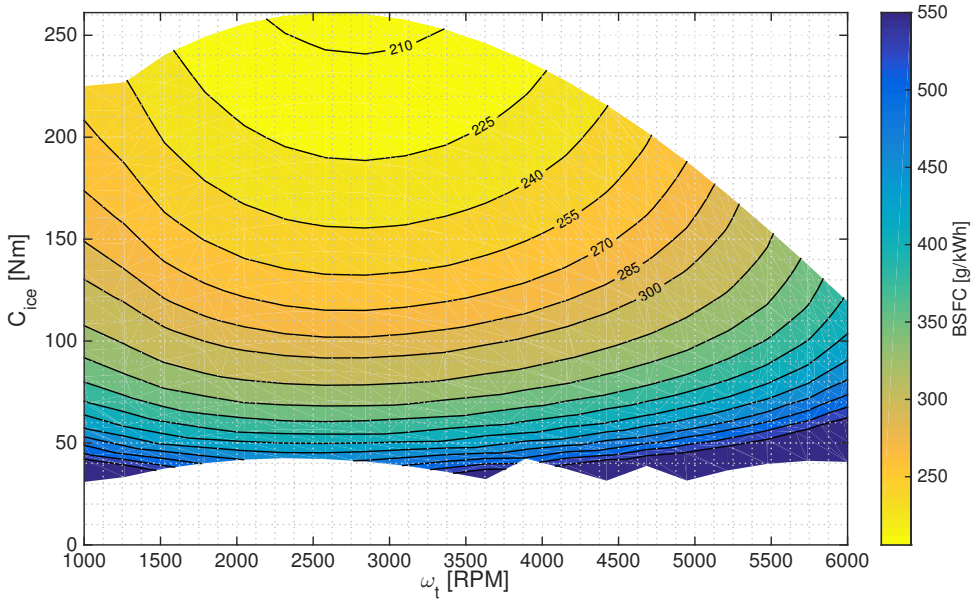

Figure 52: BSFC map

11.5 Engine's Mass

Engine's mass m_{ice} [kg] computation is achieved following its cylinder capacity according to a linearization on numerous amateur's data (see Figure 53) gathered on the internet. This takes into account the ICE only without any "auxiliaries" like the radiator(s) and the exhaust line that are supposed to have a fixed mass regardless of the engine's size (even though it is not true in practice). Those are thus assumed to be part of the minimum necessary chassis for hybrid electric application.

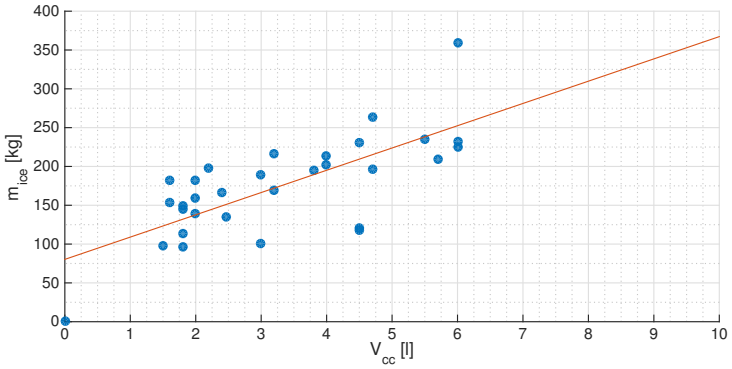

$$m_{ice} = 80.30 + V_{cc,tot}\ 28.69 \cdot 10^3 \quad (84)$$

Figure 53: Amateur's data for ICE mass computation

11.6 Black Box

The black box diagram 54 once again summarizes the whole process described above. The engine displacement $V_{cc,tot}$ [m^3], together with Table 10give condition to the whole cylinder capacity. While optimization parameters do not count the volumetric ratio - as it would always be maximized -, the timings $\theta i, j$ [°] ($i \in \{i, e\}$ and $j \in \{o, c\}$) for admission and exhaust with possible overlapping are, with ignition timing θ_s [°] part of the research for optimal energy conversion.
k_t [-] from the *Driver* via the *Power Split Device*, and ω_t [rad/s] according to the ratio selected in the *Gearbox*, give the engine state of charge.
First intake is computed via initial conditions of pressure and temperature at the exhaust. m_ϕ [kg] (and so, fuel consumption) then being known, the pressure rise during combustion can be found, which, in turn, gives initial conditions to the exhaust. Overall p_{mi} [Pa] is reduced by friction and the torque C_{ice}

[Nm] over the cycle can be outputted. $C_{ice,max,0}$ [Nm], the overall maximum torque is also demanded for the computation of the gearbox' mass. The current maximum available torque $C_{ice,max}(\omega_t)$ [Nm] is also necessary for power split evaluation (see section 6).
The process is repeated at each engine cycle (720 [°] in crank angle).

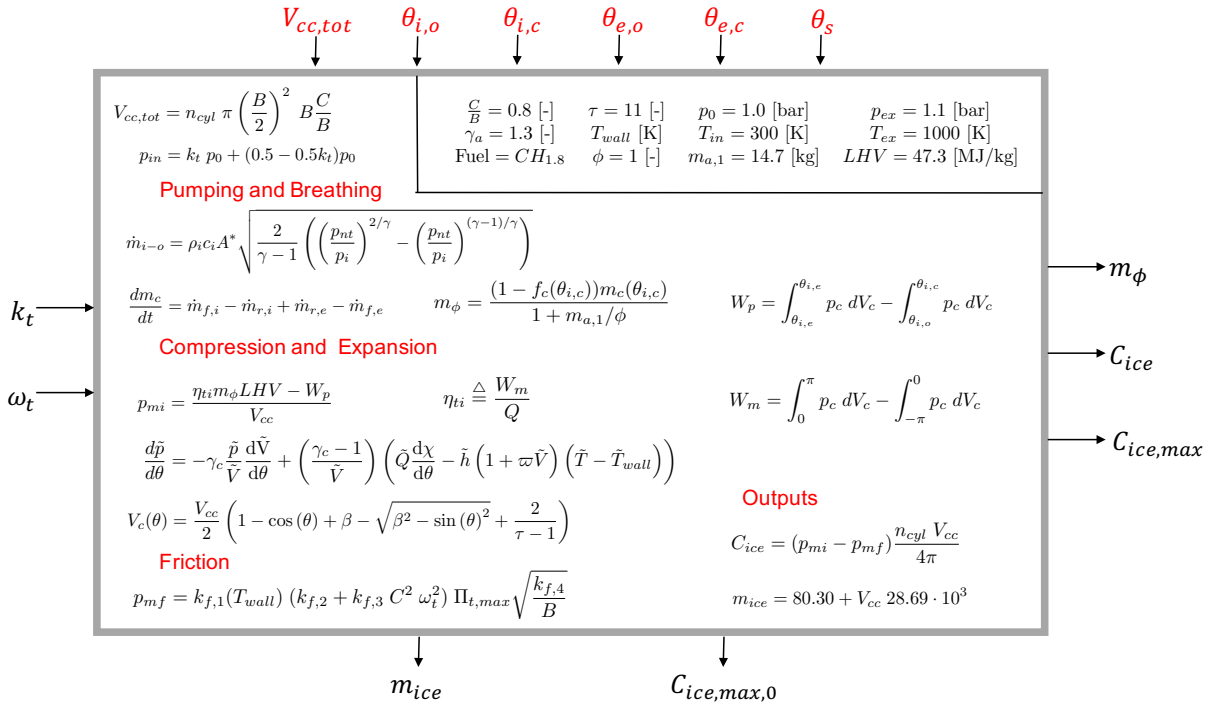

Figure 54: Internal combustion engine Black Box

11.7 Possible Improvements

Even though the model presented is rather complete, it is assumed that dynamic behaviour is a succession of steady state engine cycles which is not. It is very usual to have an engine state of charge (k_t [-], ω_t [rad/s]) that changes in between those 720 [°] of crank angle.
Moreover, there is still a certain number of parameters that are fixed even though they are supposed to change in actual operation. The one assumed to vary the most is perhaps the temperature in the exhaust manifold as this piece of equipment is not cooled and aerodynamic losses in the system can significantly reduce exhaust gas circulation at high speed, and so considerably increase T_{ex} [K]. Talking of load losses, Δp_{in} and Δp_{ex} [Pa], they are also supposed to vary with engine speed.
But the most important possible improvement might be brought to the combustion simulation and optimization since perfect, stoichiometric combustion as it is presented in this work, does not allow to compute pollutant emissions realistically; which is a bit odd when talking about hybrid vehicle as an "environmental-friendly" solution.

12 Fuel Tank

The fuel tank, containing the energy source for the ICE, is probably the easiest part to model as it present a very linear behaviour regarding its output. The mass of fuel in the tank is indeed computed at each ICE cycle $\Delta t = \frac{4\pi}{\omega_t}$ [s] as a diminution of the ICE consumption m_ϕ [kg] from its original capacity $m_{\phi,0}$ [kg]:

$$m_{tank}(t) = m_{\phi,0}(t) - m_\phi(t) \quad (85)$$

$$m_{\phi,0}(t + \Delta t) = m_{tank}(t) \quad (86)$$

And the current mass of the fuel tank $m_{tank}(t)$ [kg] is sufficient here to compute the available quantity of fuel and the actual vehicle mass, influencing on one side, the power split strategy, and on the other, overall dynamic behaviour on the road.

12.1 Black Box

The black box diagram 55 simply follows the process described by equations (85) and (86) with initial conditions of capacity $V_{\phi,0} = m_{\phi,0}/\rho_\phi$ [l] (with $\rho_\phi = 0.7$ [kg/l] gives the gasoline density) in volume chosen by the user.

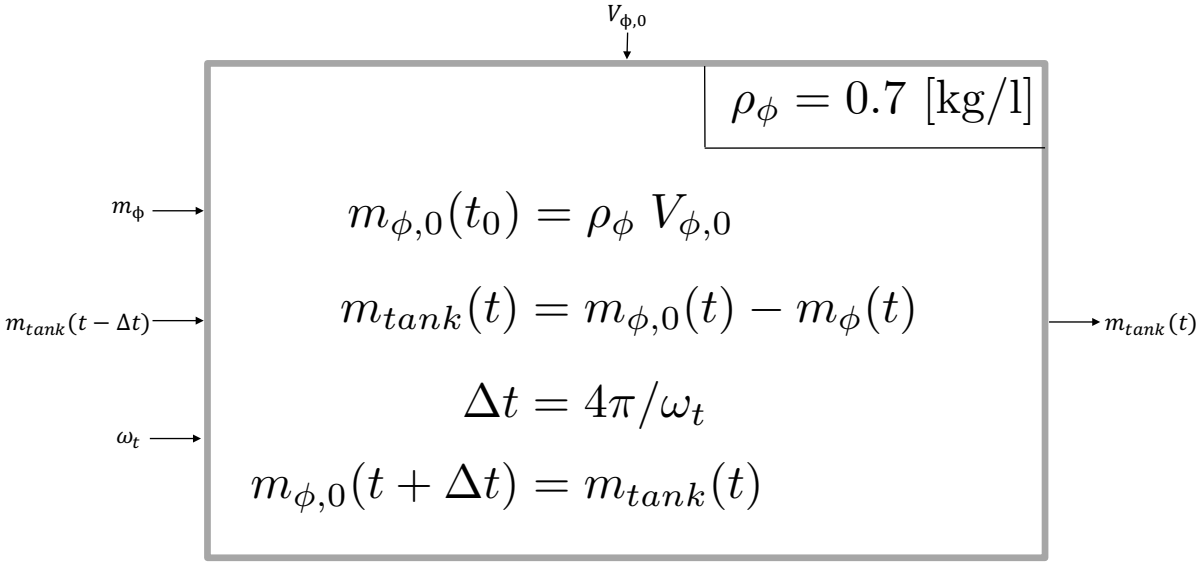

Figure 55: *Fuel tank* black box

13 Gearbox

A gearbox as its name implies, is the gear assembly allowing to select a reduction ratio i_g [-] between rotation of the motor shaft ω_{sh} [rad/s] and, here, the one of the ICE ω_t [rad/s]:

$$i_g = \frac{\omega_t}{\omega_{sh}} \tag{87}$$

Indeed, an ICE having its range of operation restricted by limitations of filling and combustion efficiency, administrating it a gear selector is necessary in order to extend the speeds at which the vehicle can travel.

13.1 Gearbox Logic

The simulation process obviously requiring the need of an automatic gear selection, several models of transmission controllers have been considered. The mostly referenced one, and therefore elected for the purpose of this thesis, is dependent of the shaft speed ω_{sh} [rad/s] and the throttle k_t [-], as illustrated in Figures 56 and 57. It is thoroughly described in MathWorks model [23].

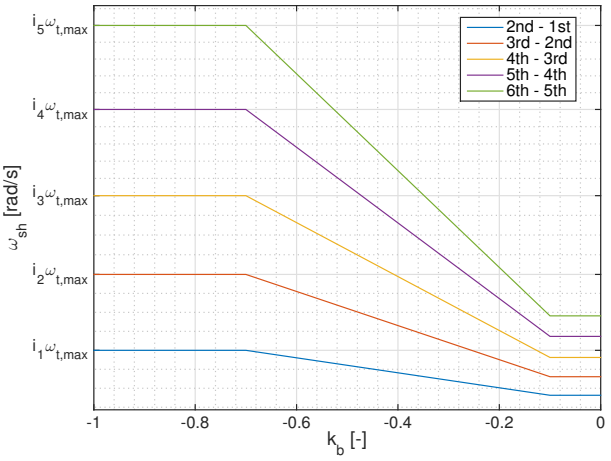

Figure 56: Down-shift gearbox logic

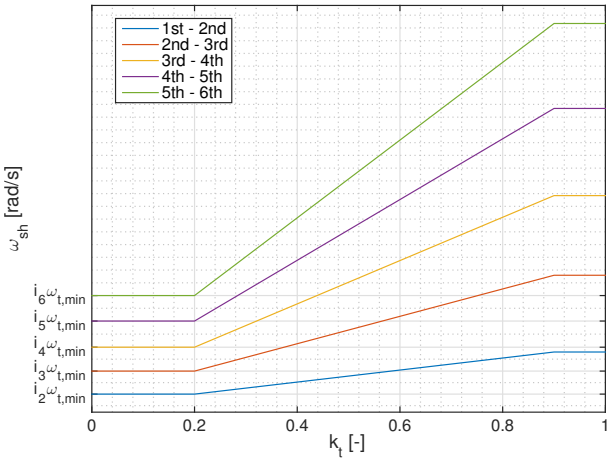

Figure 57: Up-shift gearbox logic

Where $\omega_{t,min}$ and $\omega_{t,max}$ [RPM] may be modified according to the vehicle application; with $k_{t,min} = 0.2$, $k_{t,max} = 0.9$, $k_{b,min} = 0.1$, $k_{b,max} = 0.7$ [-] (sensitivity to braking slightly increased in order to quickly downshift) are fixed arbitrarily for admissible frequency of gear change.
The graphs are easily understood as the state of charge of the ICE is at any time given as a function of two values: the rotation of the motor shaft ω_{sh} [rad/s] and the throttle k_t [-] or eventually, when engine brake is required, by the braking load k_b [-]. The transmission controller selects the gear ratio corresponding to the curve just under those state of charge coordinates.
A security range is also implemented in order to avoid oscillations between 2 gears.

As an example, if the actual state of charge is given by ($k_t = 0.5$ [-] ; $i_5\omega_{t,min} < \omega_{sh} < i_6\omega_{t,min}$ [rad/s]), the 3^{rd} should be selected.
Also, this work being about efficiency, gear change timing have been looked up for high performances gearboxes and a timing as short as 0.1 [s] has been chosen, based on dual clutch systems with continuous torque transmission.

13.2 Gear efficiency

Also, friction notably increases between gears at higher rotation speeds. In order to take that influence in a non-perfect coupling model, a formula for the gearbox efficiency in motoring is developed in [24] and exposed here:

$$\eta_{gb}(t) = \frac{C_{sh}(t)}{i_{g,j}(t)\ C_{ice}(t)} = \left(\eta_{g,0} - \frac{\eta_{g,1}}{\omega_{g,1}}\omega_t(t)\right)^{\text{sign}(C_{sh}(t))} \tag{88}$$

With $j \in \{1, 2, ..., 6\}$ according to the gear selected; and where $\eta_{g,0} = 0.95$ [-] is the generally admitted efficiency between two gears in longitudinal layout, $\eta_{g,1} = 0.02$ [(rad/s)$^{-1}$] and $\omega_{g,1} = 400$ [rad/s] are parameters of the pre-cited model.

13.3 Gearbox' mass

For the computation of the mass, numerous dimensional and structural parameters must be taken into account: single or dual clutch, material used, durability... However, for the sake of simplicity, only the maximum transmittable torque (i.e. $C_{ice,max}$ [Nm]) is elected as dimensional parameter. A linearization (see Figure 58) on various data gathered on the internet gives equation (89) for the gearbox' mass m_{gb} [kg]:

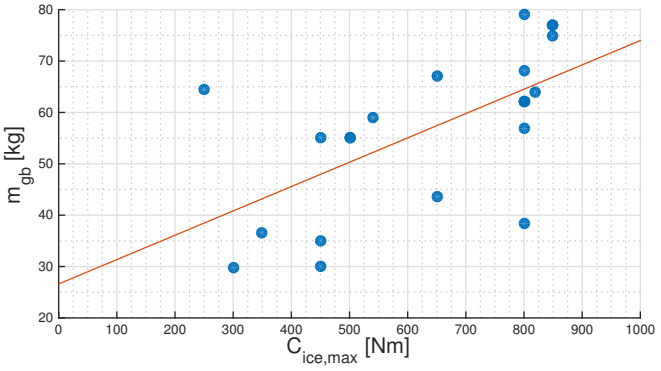

Figure 58: Gearboxes' masses linearization

$$m_{gb} = 26.614 + 0.047\ C_{ice,max} \tag{89}$$

13.4 Vehicle's effective mass

The major problem of gear reduction is not its own mass, but the fact that it introduces non negligible supplementary inertia to the car. In multibody simulation, this inertia can be described by a matrix associated to the gearbox element, itself linked to the chassis via rotary joints. This technique however introduces new degrees of freedom (dof) and thus sensible additional processing load. Another way of taking into account the gearbox inertia is via the concept of vehicle's effective mass introduced in [4]. The additional inertia is computed via the variable mass m_e [kg] of the vehicle according to the selected gear ratio.

$$m_e = (1.04 + 0.0025(i_{diff}\ i_g)^2)\ m \tag{90}$$

Where m [kg] is the nominal mass of the car and i_{diff} [-], the differential gear ratio.

13.5 Black Box

As described above, gear is selected according to a logic depending on the state of charge of the powertrain. Inputs of rotation speed ω_{sh} [rad/s] and load k_t or k_b [-]. Following the selection, speed output ω_t [rad/s] for the operation of the ICE and transmission of C_{sh} [Nm] is computed for a given C_{ice} [Nm].
Gear ratios are part of an optimization process since they can take different values according to the overall complexity of the performance test track. Each ratio is a sum of gear range $\Delta i_{g,j}$ [-] for the process not to take gears $i_{g,j-1}$ and $i_{g,j+1}$ as limits for calculation of $i_{g,j}$ [-]. Note that, for $i_{g,j}$ to logically decrease the ICE speed ω_t [rad/s] when up-shifting, $\Delta i_{g,j} < 0$ [-] except for $j = 1$.
Finally, the gearbox' mass is a parameter fixed in time to impact the vehicle behaviour on the road.
The complete methodology is summarized in black box 59.

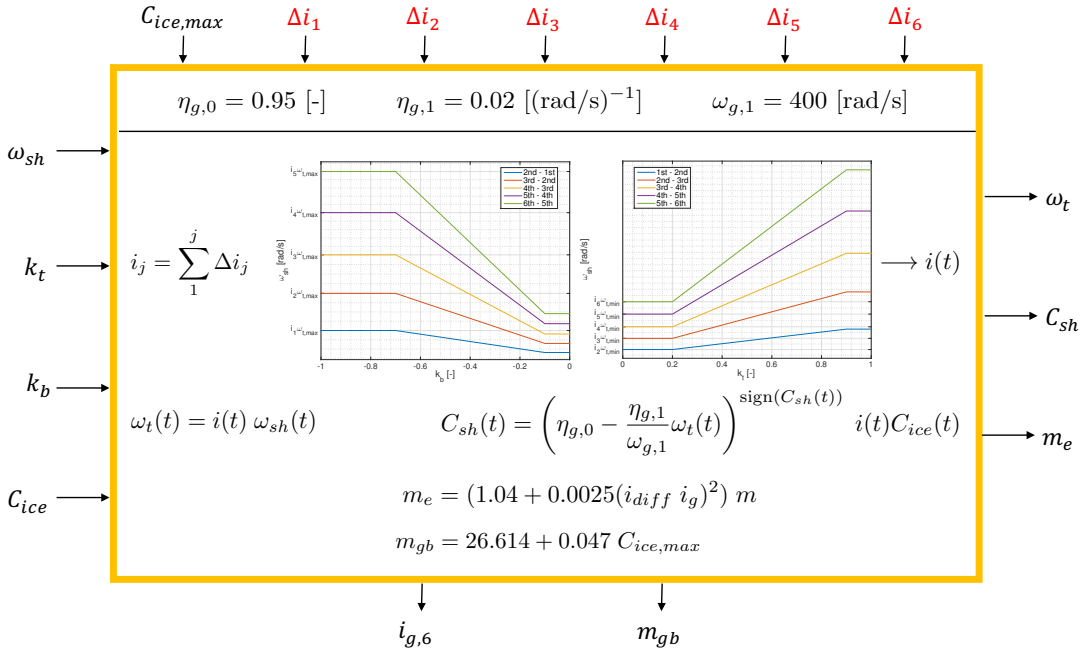

Figure 59: *Gearbox* black box diagram

14 Differential

A differential is a necessary system allowing a difference between left and right driving wheel rotation speeds. This is particularly important to control the motricity of the car in curves. Indeed, the radius of curvature of a turn not being the same for the inside and outside wheels, the circumferential slip is not the same for both. Though it is precisely this value, plus the discharge of the inside wheel due to lateral acceleration, that limits the torque transmittable to the ground by the tire (see section 5.2 *Chassis, Tire-to-Ground Model*). Independent rotation being enabled by conventional differential, if the maximum grip potential of one wheel is reached, it accelerates without raising the torque transmitted to it. The torque coming from the motor shaft should thus be limited for the wheel with minimal grip potential. This paradox lead to under-exploitation of the powertrain motricity.
To counter this absurdity, limited slip differentials (LSD) transfer the engine to the wheel with the best grip potential (i.e. the slower wheel) in order to gain better dynamic performances in turns.
However, in normal operation, LSD mus work as an open differential. Indeed, in a normal turn, the slower wheel is the inside, less charged one. In that case, best motricity is achieved by transferring the torque to the outside, quicker but more charged wheel. Therefore is torque vectoring considered in this chapter.

14.1 Limited Slip Differential

A "clutch pack" version of the limited slip differential (LSD) is observable on Figure 60.

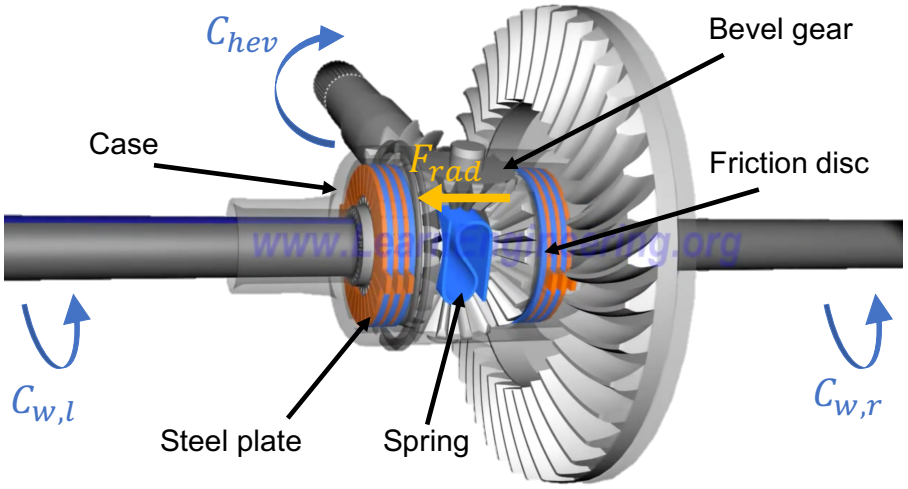

Figure 60: Flat limited slip differential schematics[7]

This type of differential - compared to the traditional one - limits the motion of the wheel with reduced grip regarding the other, by introducing friction between steel plates and discs (orange and blue respectively on Figure 60) in two clutch arrangements. The blue steel plates are fixed to the case of the differential while the orange friction discs are locked to the left and right wheel axles.
Moreover, the bevel gears, also used in usual differentials, have the particularity of generating a radial force F_{rad} [N] when transmitting a torque. So, eventually, this radial force pressing the "clutch" assembly against the case of the differential, the axle can rotate with the case, power flows to the wheel receiving the most torque, i.e. the one with the better grip. On the other, low traction wheel, the clutch will loosen to the point that only the pre-load spring will assure a minimal torque transmission equal to the friction torque $C_{f,diff,\gamma}$ [Nm], assuring limited power flow, and so that the vehicle can overcome the traction difference paradox.
Note that friction can be induced by very different ways than clutches.

14.2 Torque Vectoring

In order to fully master the torque balance, the spring load, and so the torque transfer, should be regulated (inspired by Mercedes-AMG GmbH Electronic LSD) according to the turn's radius, i.e. according to

[7]Found on http://www.learnengineering.org/2014/05/limited-slip-differential.html, 30/04/2016

the steering rack-and-pinion gear displacement Δ_{rp} [m]. The idea is to manage the balance of torque between the two driving wheels for better motricity. Without loss of power, a fraction t_{vec} [-] of the rear (propulsion) axle torque $C_{w,r}$ [Nm] is transferred to the outside wheel and so retracted from the inside, slower wheel.
Knowing that $\Delta_{rp} > 0$ [m] in case of right turn, and < 0 [m] in left turn, equation (91) gives the differential laws of control:

$$\text{Turning if } |\Delta_{rp}| > 0 \begin{cases} C_{w,r,r} = \frac{C_{w,r}}{2} - t_{vec}(\Delta_{rp})|C_{w,r}| \\ C_{w,r,l} = \frac{C_{w,r}}{2} + t_{vec}(\Delta_{rp})|C_{w,r}| \, \frac{\omega_{w,l}}{\omega_{w,r}} \end{cases} \tag{91}$$

The fraction t_{vec} [-] is limited to 40 [%] pushing the unbalance to maximum 90 [%] - 10 [%] of $C_{w,r}$ [Nm] in case of short turn; an ESP being also implemented for individual wheel braking.

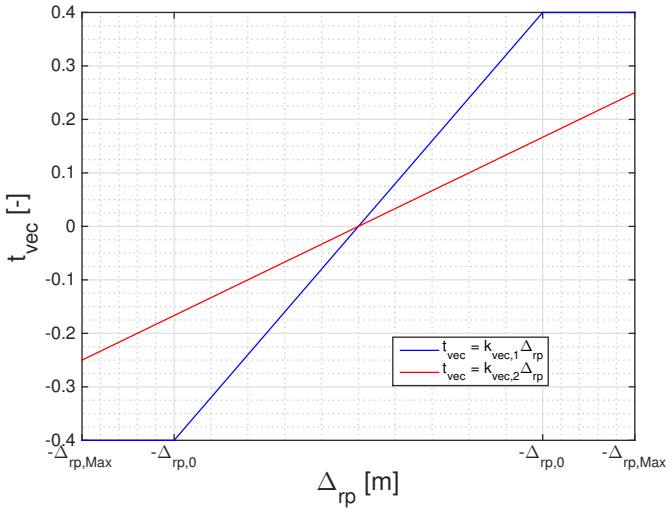

$$t_{vec}(\Delta_{rp}) = k_{vec}\ \Delta_{rp} \quad \in [0\ ;\ 0.4] \tag{92}$$

Figure 61: Torque vectoring logic

Of course, at maximum steering angle, the fraction can take lesser value than 0.4 [-] following the slope k_{vec} [-] which is part of a global optimum research.

In such a configuration, the torque $C_{w,r}$ [Nm] applied to the driving wheel axle and the rotation speed ω_{sh} [rad/s] of the motor shaft are computed as:

$$C_w = i_{diff}\ \eta_{diff}\ C_{hev} \qquad \omega_{sh} = i_{diff}\frac{\omega_{w,o} + \omega_{w,i}}{2} \tag{93}$$

$\eta_{diff} = 0.95$ [-], represents the gear efficiency, i_{diff} [-] is thus the fixed differential's reduction ratio while C_{hev} [Nm] gives the total torque produced by the hybrid powertrain:

$$C_{hev}(t) = C_{sh}(t) + C_{etm}(t) \tag{94}$$

C_{sh} [Nm] coming from the motor shaft of the ICE and C_{etm} [Nm] generated by the electric motor.

14.3 Differential's Mass

According to the limited amount of data found, the differential's mass has been fixed to $m_{diff} = 35$ [kg].

14.4 Black Box

According to the longitudinal slips $\gamma_{long,l}$ and $\gamma_{long,r}$, and the steering angle (via the rack and pinion displacement Δ_{rp} [m]), the electronic limited slip differential knows whether the faster wheel is outside a curve and/or on a slippery surface; and it transfers the total torque C_{hev} [Nm] accordingly.
The quantity transferred is influenced by the calibration parameter k_{vec} [-] in torque vectoring and t_{diff} [-] in limited slip operation, and because i_{diff} [-] gives condition to the maximum speed of the vehicle but

also its maximum output torque to the ground, the three parameters are part of an optimum research following the track.

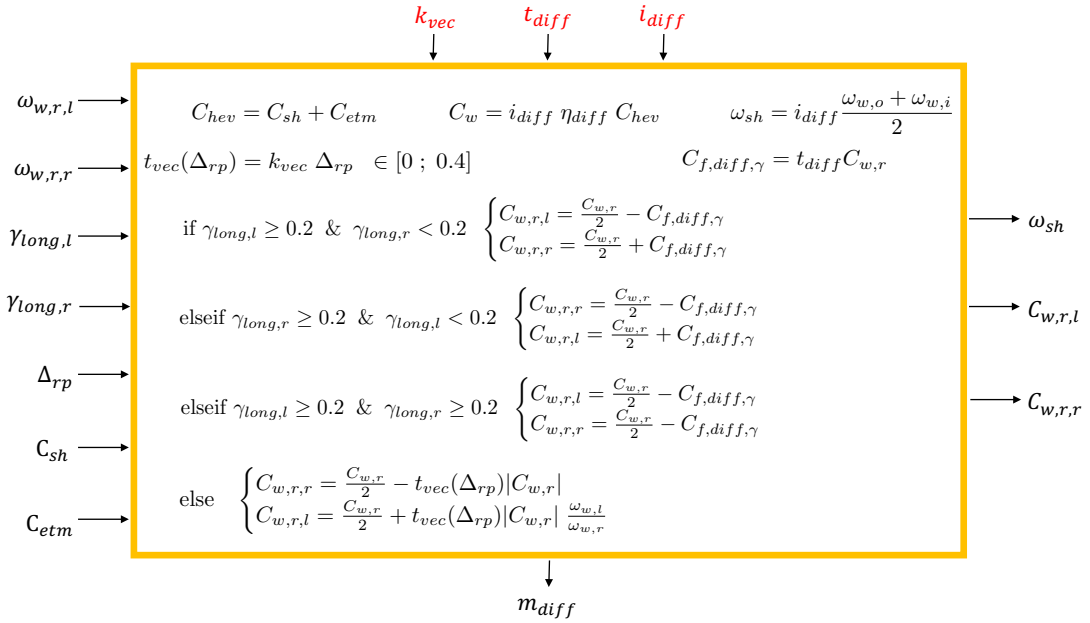

Figure 62: *Differential* black box diagram

15 Aerodynamics

The global modeling of the vehicle would not be complete without studying its behaviour in the air that surrounds it. Indeed, if one recalls the very first equation of this report, the road resistance can be expressed as:

$$R_{road} = R_{x,f} + R_{x,r} + mg\sin(\alpha) + D_{aero} \tag{95}$$

Where $R_{x,f}$ [N] and $R_{x,r}$ [N] are the rolling resistances on the front and rear axle respectively, $mg\sin(\alpha)$ [N] the vehicle's weight on a slope of α [°], and finally D_{aero} [N] the aerodynamic drag.
Against aerodynamic drag, not all vehicles are equal but it is generally assumed that, for normal passenger cars, it represents the most critical part of the road resistance above 80 [km/h], as exposed in [4] and on Figure 63.

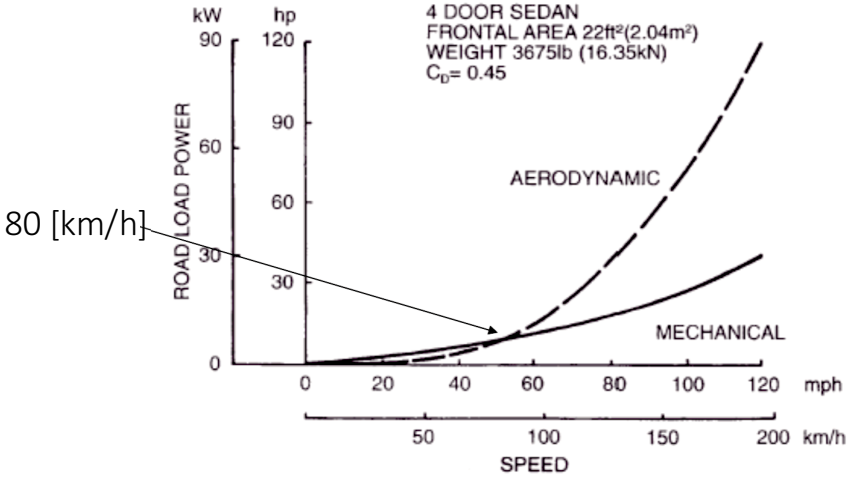

Figure 63: Power requirements of a full-size passenger car as a function of speed [4]

Hence the importance of computing the aerodynamic efforts in this work of simulation.

15.1 Model Limitations

Unfortunately, a complete simulation of the vehicle would be extremely computationally demanding. Even for car manufacturers or racing teams, computational fluid dynamic (CFD) analysis (not feasible in this work) is besides most often accompanied by tests in wind tunnels on full- or small-sized bodies.
For the purpose of this work's global simulation, the simplest way to consider the car is through its representative aerodynamic coefficients. But before any further details, certain hypotheses have to be made:

1. No wind is considered, the only displacement of air on the car's body is due to its own movement in the fluid
2. The car is supposed airtight (no air intakes), and the rotation of the wheels induces no perturbation
3. The aerodynamic coefficients are assumed constant whatever the speed
4. The lift has zero X-axis or Y-axis component (perfectly symmetric vehicle even in turns)
5. The natural drag and lateral forces components are applied to the centre of mass
6. Aerodynamic "add-ons" are able to displace the lift's application point
7. The lateral flow speed is weak compared to the longitudinal one
8. The effects of pitch and roll are neglected, and yaw has an impact on drag and lateral force only [25]

15.2 "Natural" Aerodynamic Efforts

The fluids mechanics say that any body in movement in a fluid (or any body immersed in a moving fluid with velocity $\underline{v} = (v_x\,;\,v_y\,;\,v_z)$ [m/s]) undergoes a drag - according to the direction of the vehicle's velocity, X-axis, as opposed to the movement - and a lift - vertical, Z-axis - force, both illustrated in Figure 64. If the first one is critical, as aforementioned, for rolling resistance, lift can play a significant role for the dynamic behaviour of the car in turns (eventually providing aerodynamic support for better wheel-to-ground contact).

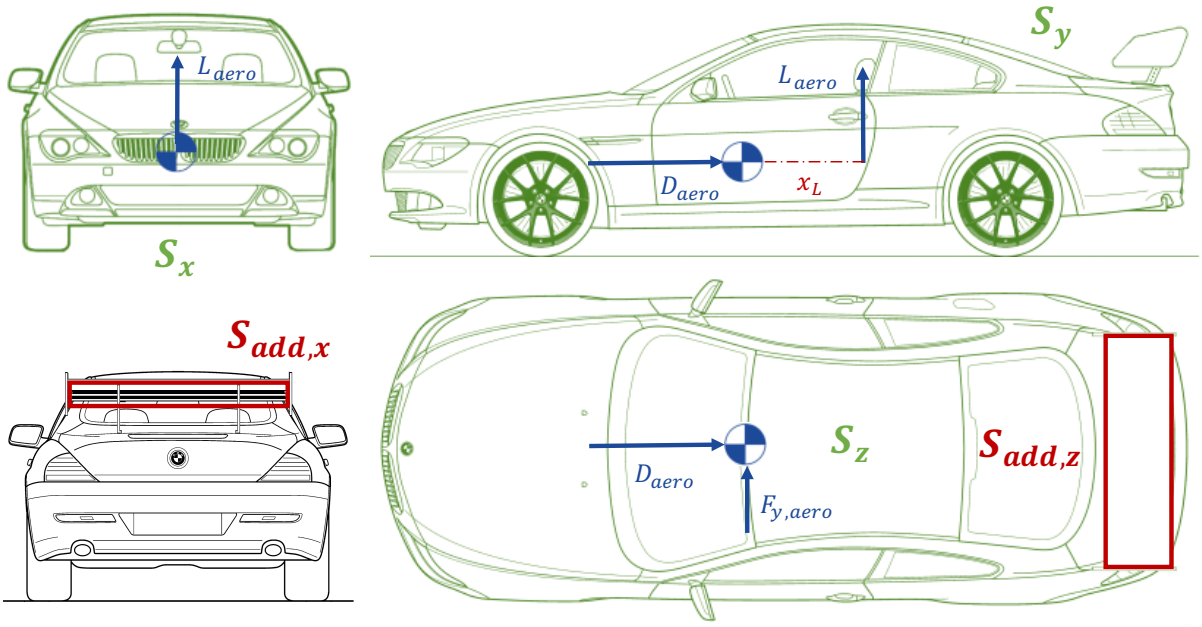

Figure 64: Illustration of the aerodynamic efforts applied on the car and reference areas

Drag

The aerodynamic drag D_{aero} [N] is thus the force applied by air (supposed incompressible of density $\rho_0 = 1.184$ [kg/m^3]) on the frontal surface of the car S_x [m^2]. Its intensity depends on aerodynamic profile of the car which is represented by the sole drag coefficient C_x [-] (the more streamlined profile, the lower the C_x).

$$D_{aero} = \frac{1}{2}\rho_0\, C_x\, S_x\, v_x^2 \tag{96}$$

If C_x [-] describes the profile, it is not true that its value is solely influenced by the body shape. Indeed, it should be noted that the drag is generally due to the bodywork for up to 70 [%] (40 [%] for the upper part and 30 [%] for the lower part, the sides not mattering), to the wheels for up to 15 [%] and to the air ventilation system up to 10 [%] (up to ±5 [%] for the rest) [26].

Lateral force

In rare situations, the car's movement is not purely longitudinal as the most extreme case would be drifting sideways, but also during quick changes of velocity (such as slaloms for instance). In that case, $\underline{v}$ has a non-zero v_y [m/s] component. The surface facing this component is then S_y [m^2] - as shown on Figure 64 - and subjected to lateral aerodynamic force $F_{y,aero}$ as defined by equation (97).

$$F_{y,aero} = \frac{1}{2}\rho_0\, C_y\, S_y\, v_y^2 \tag{97}$$

For obvious reasons of door access and vehicle track width, the lateral profile of the car is generally not optimized from an aerodynamic point of view, hence $C_y >> C_x$ [-]. C_y [-] being quite hard to find in manufacturers' specification sheets, it is here evaluated according to [27] as a function of the vehicle width / height ratio.

Lift

Defined in the same way, the aerodynamic lift L_{aero} [N] takes S_z [m^2] as reference surface.

$$L_{aero} = \frac{1}{2}\rho_0 \, C_z \, S_z \, v_x^2 \tag{98}$$

For normal passengers cars, the lift is generally positive, the boundary layer forming on top of the vehicle "sucking" it upwards. However, as for racing motivation, consequent aerodynamics "add-ons" such as wings and spoilers can dramatically reduce the C_z [-] and even making it negative, then pushing the cars on the road.

15.3 Aerodynamic "Add-Ons"

For the purpose of simplicity, all add-ons will be approximated by a flat wing of which the lift coefficient $C_{z,add}$ [-] can be adjusted by its angle of attack. This wing frontal area is designated by $S_{add,x}$ while its surface is given by $S_{add,z}$ [m^2] (cfr. Figure 64)
In simulation, this "virtual angle" and thus $C_{z,add}$ [-] is fixed beforehand and never adapted in running time.
Also, intelligent repartition (front spoiler and canards, rear wing, etc...) of add-ons along the car's bodywork can change the point of application of the lift at a virtual distance x_L [m] from the center of mass (see Figure 64).

The main problem of this technique for track engineers is that this lowering of overall C_z [-] is generally accompanied by an augmentation of the drag. Lots of research has been done on the subject proposing solutions such as segmentation of the wings to reattach the boundary layer on smaller chords. But all in all, keeping the approximation of flat wing in mind, the induced drag coefficient $C_{x,add}$ [-] is computed as:

$$C_{x,add} = \left(c_{drag} + \frac{1}{\pi \, e_{Osw} \, AR} \right) \, C_{z,add}^2 \tag{99}$$

Where c_{drag} [-] represents the drag compressibility coefficient (assumed to be 0 by applying the *Thin Airfoil Theory*); e_{Osw} [-] the Oswald's efficiency and AR [-] the aspect ratio (wingspan - mean chord ratio).

15.4 Black Box

Firstly, a certain number of dimensions and "natural" coefficients have to be fixed. Those are based on a second generation BMW 6-series E63 (2003-2010) for the simple reason that it is the bodywork used for the 3D animation of this simulation work. Those quantities are exposed as hypotheses in the box 65.

This *black box* simply needs X and Y components of the vehicle's velocity to compute all 3 aerodynamic efforts.
Optimization of the profile is done by virtually adding pieces of equipments in order to 1) decrease the lift or augment the aerodynamic support and 2) displace the point of application of the lift and so increase stability of the car subjected to pitch. All add-ons are approximated by a single flat wing of dimensions $S_{add,x} = 140\,x\,15$ [cm^2] and $S_{add,z} = 140\,x\,50$ [cm^2] (thus AR = 140/50 = 2.8).

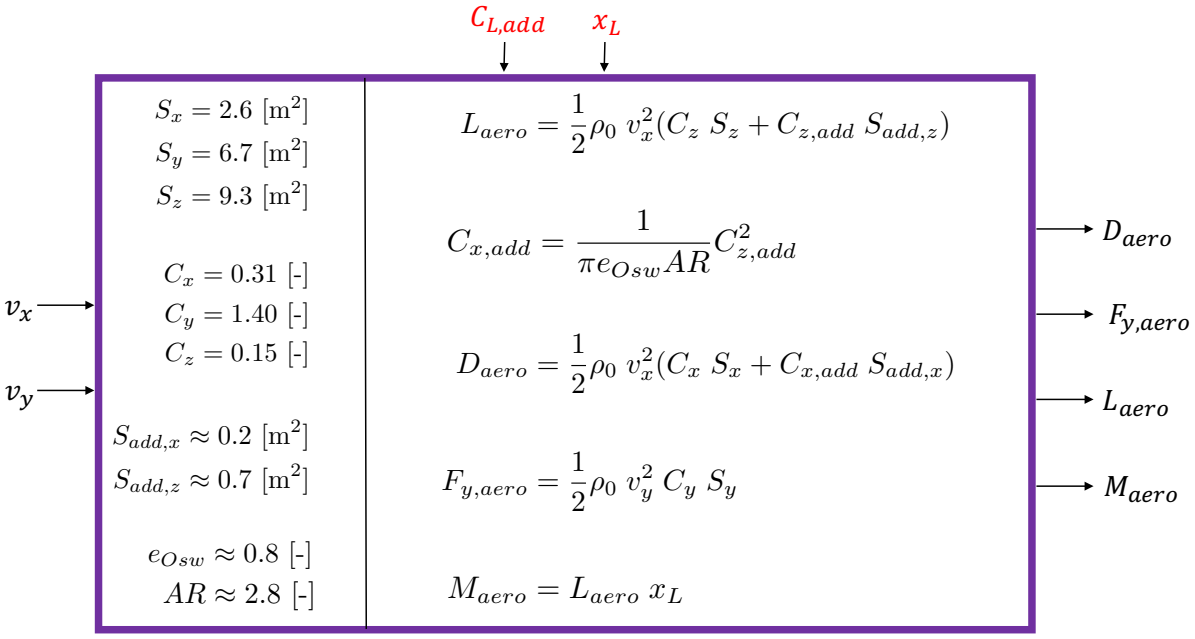

Figure 65: *Aerodynamics* black box

Part II

Performances Optimization

1 Introduction

The first part of this report was about presenting the different important models to consider in a global vehicle simulation.

The second phase of this work consists in the implementation of those models in the *Robotran* © environment. This means creating a module of two C language files (header + source file) for each of the powertrain / braking / aerodanymic part, that has to be sort of "transplanted" in the multibody template representing the purely mechanical "naked" chassis.
This system is thus edited in $MBSysPad$, its symbolic equations of motion generated by $MBSysTran$ and its interface with the C language compiler is assured via $MBSysC$. These are the three tools constituting the *Robotran* © suite.

This parametrized global simulator of the hybrid electric vehicle coded, the objective remains to study its performances on a reference track. This second part of the present report exposes the strategy adopted for such a study.
Firstly, its is important to have a clear definition of what is the traditional vehicle's performances study, its interests, but also its weaknesses. This is generally achieved with driving cycles (vehicle's longitudinal velocity versus time) predefined by the competent authorities but also very different from the reality of the average driver's behaviour. The *Driver* model as described in Part I, chapter 4 is not supposed to be perfectly simulating reality either but strives to mimic the attitude of a pilot without limitation of speed or traffic density.

A genetic optimization is then applied to the model with various objective functions regarding its fuel consumption and the lap time it requires on track. The process eventually elects the most suited set of sensitive parameters - highlighted in red in the first part of this report - for the desired use, i.e. the entered objective function.

2 Vehicle Performances

In order to fully apprehend the methodology for performances evaluation adopted in this work, certain highlights and definition must be introduced. This chapter makes a summary of how vehicle performances are usually characterized and of the procedure followed here.

2.1 Hypotheses and Limitations

Firstly, in order to expose the limitations of the simulator, some hypotheses have to be formulated:

1. The vehicle is made of the subsystems and components described in the Part I only
2. Though the motion considered is of the vehicle as a whole, rigid body characterized by its geometry, mass and inertia
3. Distribution of the subsystem's masses is uniform regardless of their individual dimensions
4. The test track makes a loop and is considered to be completely flat
5. Grade-ability is thus studied mathematically
6. The driving conditions are only track-related, and according to the desired performances in terms of fuel economy and/or lap time
7. No speed limit, traffic density, nor weather conditions were implemented

In practice, hybrid electric vehicles are made of a vast number of components that are not all reviewed in the modeling part of this work. However, for the sake of viable computation-time, only the most important parts of the powertrain and braking systems are elected. Those are represented as parametrized "*black boxes*" with electrical or mechanical input and output. Their inertiae are, as far as possible, taken into account but the processing load of generating equation for every gear, piston or even the clutches in the powertrain structure was far too heavy for a global vehicle simulation. Instead, the only "moving" parts are from the "naked" chassis: the steering four-bars mechanism, the four wheels and their respective axles, suspensions and the anti-roll bars.
The masses of the principal subsystems described are the heaviest; but again, they are only attributed to the center of mass of the vehicle, no spatial repartition was considered.

Regarding the driving conditions, some hypotheses have also been made. The track is a complete and rather simple loop along which no variation of the tire-to-ground friction coefficient μ_{ttg} [-] is registered (as if the road was made of various materials or if weather could change). The *Driver* reacts to it as described in Part I, chapter 4, without external limitations like speed limit or traffic density.

2.2 Braking Distance

Even though it is generally not documented in vehicles' datasheet, longitudinal deceleration from 100-0 [km/h] can be particularly interesting for 1) evaluating the braking performance of the vehicle or 2) observing the energetic quality of the regenerative braking in a HEV powertrain architecture.

2.3 Acceleration and Maximum Speed

Tractive force

If one recalls the very first equation of this report, it is obvious that the only direct lever that a powertrain engineer has on longitudinal acceleration performance is the tractive force F_x [N] applied by the motorized wheel on the ground:

$$a_x = \frac{1}{m}\left(F_{x,r} - R_{x,f} - R_{x,r} - mg\sin(\alpha) - D_{aero}\right) \tag{100}$$

$$F_{x,r} = \frac{\eta_{diff}\, i_{diff}}{R_e}\left(C_{etm} + \eta_{clutch}^2\, \eta_{gb}\, i_g\, C_{ice}\right) \tag{101}$$

The importance of a good choice of reduction ratios at the differential $i_{diff} = \omega_{sh}/\omega_w$ [-] and at the gearbox $i_g = \omega t/\omega_{sh}$ $(i_{g,1} > i_{g,2} > ... > i_{g,6})$ [-] appears in equation (101) as it limits the force transmitted

from the powertrain. Coupled to an intelligent gearbox logic, this can play a significant role in traditional performance evaluation via 0-100 [km/h] or 40-120 [km/h] acceleration.
Indeed, [27] highlighted a criteria for upshifting or not in order to minimize the acceleration time. On Figure 66, $1/a_x$ [1/(m/s^2] versus v_x [m/s] is displayed. If two curves intersect with each other, a gear change is optimal at the intersection. If not, it is preferable to push the gear up to its maximum rotation speed. Note that the lower limit to the acceleration time is realized for continuously variable transmissions (CVT).

For example, a simulation exercise lead on a 2010 Ford Mondeo 1.8 TDCi with gear change timings of 0.8 [s], gave the times shown in Table 11 for 40-120 [km/h] (finished in 4^{th} gear) acceleration.

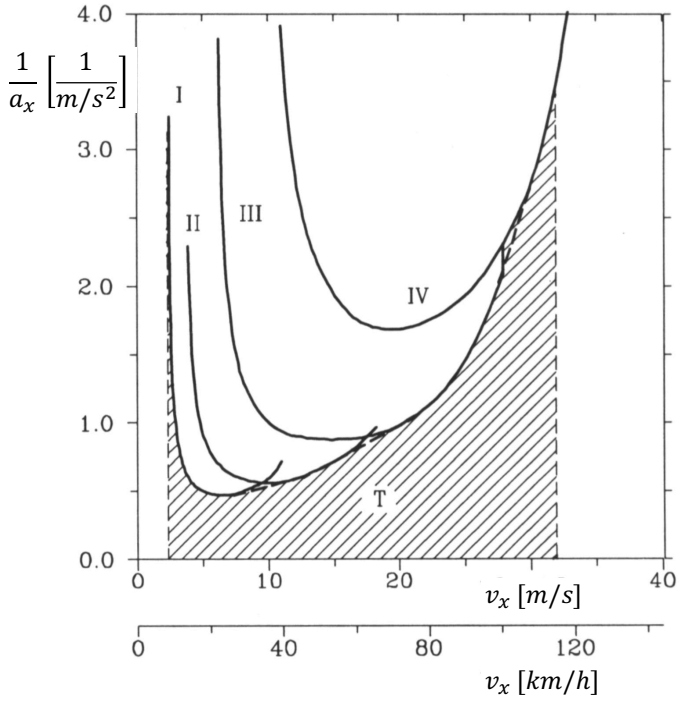

Figure 66: Up-shifting criteria for minimal acceleration time

Start in 2^{nd}	Start in 3^{rd}	Start in 4^{th}
13.029 [s]	12.795 [s]	14.150 [s]

Table 11: 40-120 [km/h] acceleration for a simulated 2010 Ford Mondeo 1.8 TDCi[8]

The gear ratios also have an impact on the vehicle speed via the transmission length R_e/i [m], and thus eventually on the vehicle maximum speed:

$$v_x = \frac{R_e}{i_{diff}}\,\omega_{sh} = \frac{R_e}{i_{diff}\,i_g}\,\omega_t \tag{102}$$

The vehicle's longitudinal performances are thus a compromise between acceleration via the maximum tractive force available at each gear, and maximum reachable speed. The solution generally adopted by manufacturers are shorter operating speed ranges for the first gears and thus quick acceleration at low speeds and then longer ranges for the last gears at which high cruise speed is more important than transitions.

Note that, as Figure 67 suggests, one can observe that the envelop of the tractive force curves for different gear ratios (I, II, ..., IV) is defining a constant power [28].

[8]Extract from A. WASLDORFF and T. MOND, Report for MECA0497 Vehicle Performance, P. DUYSINX, ULg, 2015

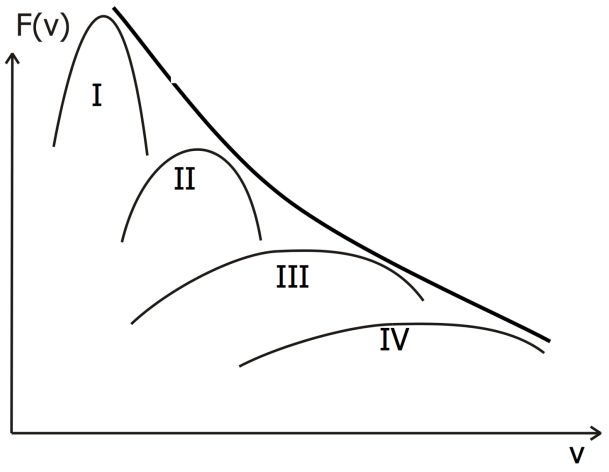

Figure 67: Tractive force curves at different gear ratios as a function of the vehicle speed

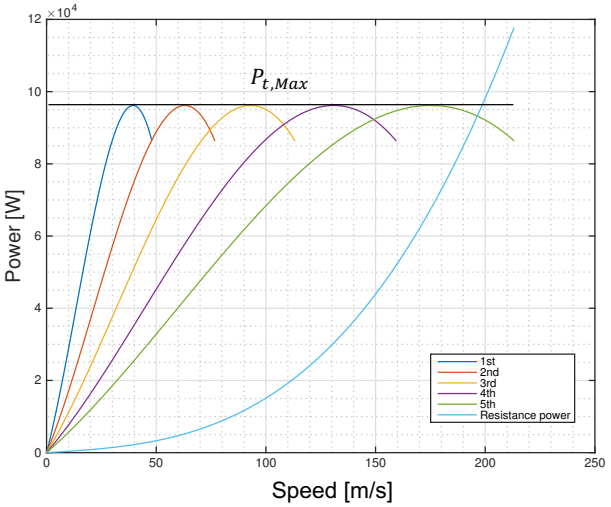

Figure 68: Tractive power versus vehicle speed for a simulated 2010 Ford Mondeo 1.8 TDCi[8]

Road resistance

From equation (100), one can also extract the road resistance:

$$R_{road} = R_{x,f} + R_{x,r} + mg\sin(\alpha) + D_{aero} \tag{103}$$

Which, by definition of the aerodynamic drag D_{aero} [N] varies as a quadratic function of the longitudinal velocity.

$$D_{aero} = \frac{1}{2}\rho_0\, C_x\, S_x\, v_x^2 \tag{104}$$

So, the job of the powertrain engineer is to dimension the ICE and the gearbox in coordination so that 1) enough power is produced to vanquish the road resistance at the desired maximum speed, 2) the ICE does not reach its breaker (around 7000 [RPM] for normal passenger cars) before meeting the road resistance curve (sign of under-dimensioning of the gearbox).
Figure 68 illustrates the tractive power regarding the vehicle speed at different gear ratios for a simulated 2010 Ford Mondeo 1.8 TDCi.

2.4 Grade Ability

Another way of evaluating the vehicle's performance is to observe its ability to overcome slopes.

Powertrain condition

Hill-starts indeed are not equal amongst any model and four-wheel drive eventually with electronic power split are probably the most suited for the job. Anyway, the vehicle simulated for the purpose of this work is rear wheel driven, so the interest is on the force transmitted on the rear wheel-axle. Also, the elected powertrain configuration allows to slide the clutch in order to reach maximum ICE output torque, but the ETM's rotor is itself directly linked to the motor shaft, and therefore, to the rotation speed of the wheels via the differential. In that case, its output torque in hill-start is the starting torque $C_{etm,0} = C_{etm}(\omega_{sh} = 0)$ [Nm].
The powertrain condition to maximum slope thus reads as:

$$F_{x,r,1,Max} \geq R_{x,f} + R_{x,r} + mg\sin(\alpha_{pwt}) \tag{105}$$

$$\text{with } F_{x,r,1,Max} = \frac{\eta_{diff}\, i_{diff}}{R_e}\left(C_{etm,0} + \eta_{clutch}^2\, \eta_{gb}\, i_{g,1}\, C_{ice,Max}\right) \tag{106}$$

$$\alpha_{pwt} \leq \arcsin\left(\frac{F_{x,r,1,Max} - R_{x,f} - R_{x,r}}{mg}\right) \tag{107}$$

Tire-to-ground condition

The maximum slope that a vehicle can overcome does obviously not depend only on the powertrain but also on the maximum transmissible force to the ground via a friction contact of coefficient μ_{ttg} [-]. The tire-to-ground condition to maximum slope for a rear wheel drive is given by equation (110), coming from static longitudinal equilibrium [28].

$$\mu_{ttg}\, W_r \geq mg(\sin(\alpha_{ttg}) + \varphi_r\ \cos(\alpha_{ttg})) \tag{108}$$

$$\text{with } W_r = mg\cos(\alpha_{ttg})\frac{b}{L} + mg\sin(\alpha_{ttg})\frac{h}{L} \tag{109}$$

$$\alpha_{ttg} \leq \arctan\left(\frac{\mu_{ttg}\ b/L - \varphi_r}{1 - \mu_{ttg}\ h/L}\right) \tag{110}$$

Recall that φ_r [-] is the rolling resistance coefficient on the rear (driving) axle.

The maximum slope that the simulated HEV can overcome is then obviously the minimum value rendered by those two conditions.

$$\alpha_{MAX} = \min(\alpha_{pwt}\ ;\ \alpha_{ttg}) \tag{111}$$

2.5 Fuel Economy

The final performance evaluation - and one that has along the years probably become the most important for the everyday driver - is fuel consumption and emissions. Indeed, fuel efficiency turns out to be the number one priority for car manufacturers, to the point that this pressure has led some to develop some schemes or tricks just to pass normalized bench test.

Driving cycles

In practice thus, fuel consumption and emissions of CO_2 or NO_x for instance are measured on bench tests reproducing regionally normalized driving cycles (note that bench tests do not simulate any slope). Those are standard travels where the vehicle longitudinal speed and acceleration are imposed. Figures 69 and 70 show the speed profile over time for the New European Driving Cycle (NEDC - last updated in 1997) and for the US Environment Protection Agency (EPA) Federal Test Procedure (FTP75).

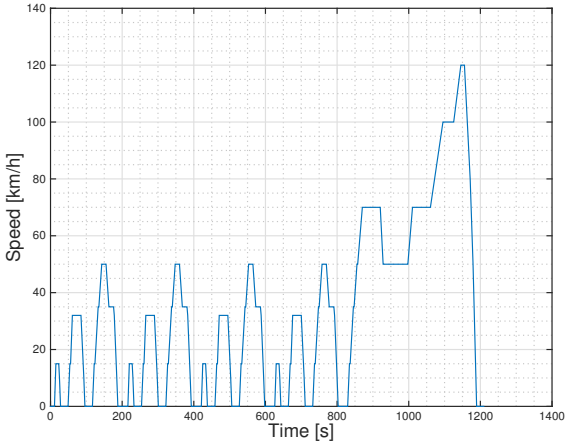

Figure 69: New European Driving Cycle

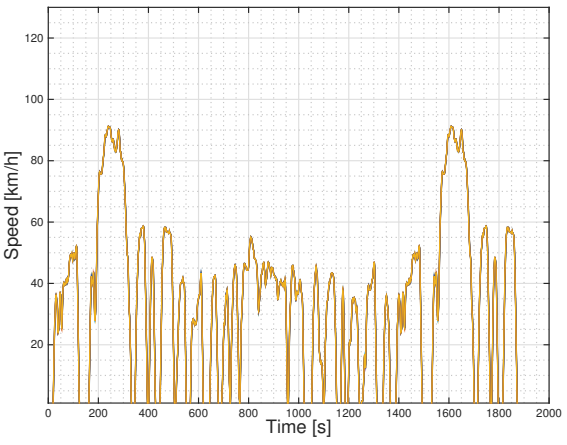

Figure 70: Federal Test Procedure 75

The NEDC is called a synthetic cycle, tailored from actual traffic speed and acceleration records which are then sorted and weighted according to their frequency and duration. The first four parts are supposed to represent urban driving and the last one extra-urban driving. A more realistic cycle is deduced directly from experimental observation of the traffic is the US FTP75. But illustrating urban driving only, the influence of aerodynamics effects at high speed is less perceptible. Other US driving cycle exist and are generally sorted by categories of weight making influence of the vehicle's mass on the fuel consumption also more difficult to identify.

A new Worldwide harmonized Light Vehicle Test Cycle (WLTC) should replace the NEDC in Europe by 2017, with 2 others classes defined by the vehicle's power-to-weight ratio. Figure 71 gives the speed profile for such a driving cyle.

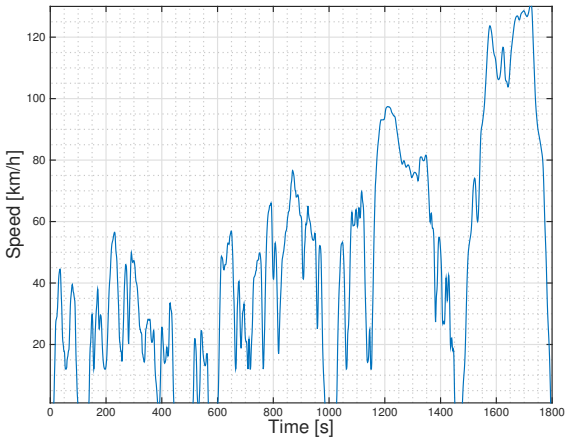

Figure 71: WLTC speed profile over time

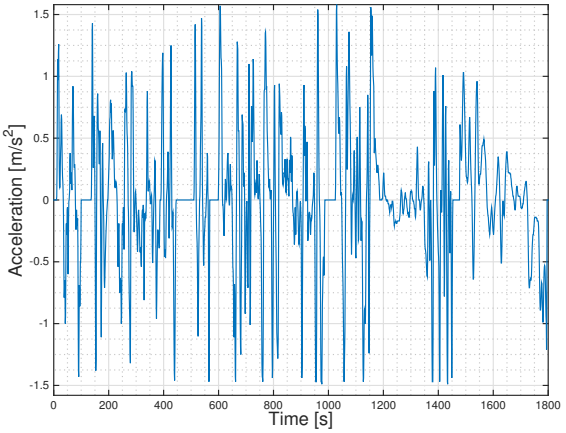

Figure 72: WLTC acceleration profile over time

Still, as Figure 72 suggests, acceleration over the WLTC are quite slow, rarely exceeding 1.5 [m/s^2] while everyday users often reach 2.5 to 3 [m/s^2]. These slow accelerations, more than being unrealistic, do not render appreciable results in terms of fuel consumption.
Moreover, in order to satisfy those poor acceleration's performances, a degrading mode of powertrain operation - keeping the ICE in favorable region of its BSFC but so offering small torque backup - is still envisageable for untrustworthy manufacturers.

2.6 Consumption of HEV

It becomes even more aberrant when it comes to the consumption of HEV. Indeed, in Europe, their consumption is evaluated in two different tests on the NEDC: the first in electric mode (gives consumption indicated by index 1 in the following) with a fully charged battery and the second in hybrid / thermal mode with a battery at minimum charge level (index 2).
Fuel consumption $\Delta V_{\phi,NEDC}$ [l/100km] is calculated via equation 112 [28]:

$$\Delta V_{\phi,NEDC} = \frac{L_{ovc}\Delta V_{\phi,1} + L_{av}\Delta V_{\phi,2}}{L_{ovc} + L_{av}} \tag{112}$$

Where $\Delta V_{\phi,1}$ and $\Delta V_{\phi,2}$ [l/100km] are the fuel consumption with a fully charged battery and at minimum SOC respectively. While $L_{av} = 25$ [km] is an arbitrary average distance between two battery recharges, L_{ovc} [km] is the distance covered before maximal battery depletion.
Such an evaluation function does absolutely not reflect the fuel consumption on the $4 \cdot 4.052 + 6.955 = 23.163$ [km] long NEDC in "real" application since current storage technology easily exceed that range with regenerative braking (and so $\Delta V_{\phi,1} = 0$ [l/100km]). Regenerative braking which also reduces significantly $\Delta V_{\phi,2}$ [l/100km] in the second test.

Note that electric consumption ΔE_{NEDC} [kWh/km] is also computed via equation 113:

$$\Delta E_{e,NEDC} = \frac{L_{fe}\Delta E_{e,1} + L_{av}\Delta E_{e,2}}{L_{fe} + L_{av}} \tag{113}$$

Where $\Delta E_{e,1}$ and $\Delta E_{e,2}$ [kWh/km] gives the electric consumption for a battery fully charged and at minimum SOC respectively. L_{fe} [km] is the vehicle's full electric range.

Finally, a last argument against the use of unrealistic driving cycles in the present performances study is that they all are evaluated over more than 1200 [s] of time. Recall that this is also a work of optimization, and the simulation of a fully parametrized vehicle for > 1000 [s] at each iteration would not be affordable in terms of computational load.

2.7 Test Track

The method adopted here is one generally used by high performance cars manufacturers. Speed and acceleration are evaluated as a lap time while fuel economy can be measured as the fuel energy needed to circle around a test track. This has significant advantages as the circuit can be designed to allow short simulation 'lap' time and experiment the dynamic characteristics of each considered model.
Indeed, a certain number of the optimization parameters (in red) modeled in Part I were track-oriented (suspensions' stiffness, braking repartition, gearbox logic, aerodynamic support, etc...).

Concerning fuel economy, if it was mentioned in the previous sections that consumption greatly depends on the driver, various behaviours can be adopted to approach the track. This gives the full justification for the forward-facing modeling endorsed in Part I. Recall that all the powertrain outputs are defined as coming from a decision (input) of the *Driver*'s box.
Moreover, it was described in Part I, chapter 4 that the model designed to mimic the operator's behaviour can be adapted by varying "aggressiveness" parameters. Following the importance attached to either pure performance measured by the lap time or to fuel economy (see chapter 3), the vehicle and the driver are optimized on track, and traditional timings like acceleration from 0-100 [km/h] or 40-120 [km/h], and maximum longitudinal speed computed. The track is then assumed to be a correct - and "non-cheating" - representation of the road following a more economic or sportive use.

As a first, non-optimal example, Figure 73 shows the track used to test a vehicle of which the model's parameters are given in Table 12.

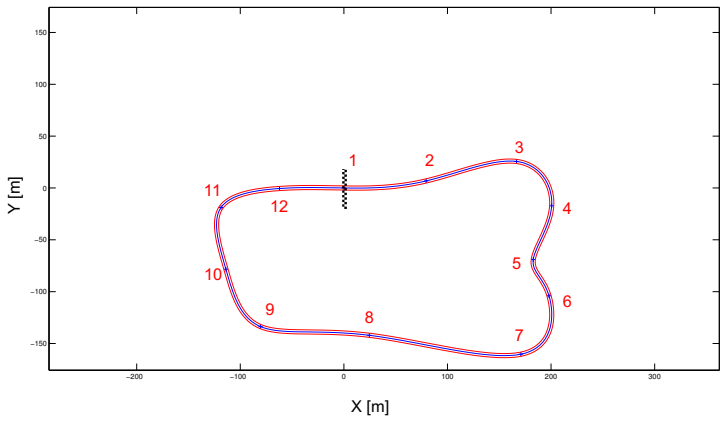

Figure 73: Reference track for dynamic performances testing

Driver	k_a	=	1.00	[-]
	k_{secu}	=	2.00	[-]
	k_v	=	0.75	[1/s]
	k_{turn}	=	15.0	[m]
ICE	$V_{cc,tot}$	=	2000	[cc]
	$P_{ice,max}$	=	90.51	[kW]
	$C_{ice,max}$	=	210.1	[Nm]
ETM	ω_b	=	2500	[RPM]
	$P_{etm,rated}$	=	156	[kW]
	$C_{etm,rated}$	=	595	[Nm]

Table 12: Global parameters' values of the HEV simulated

The results of speed profile and gear selection when the described HEV circulates around that track can be observed in Figure 74.

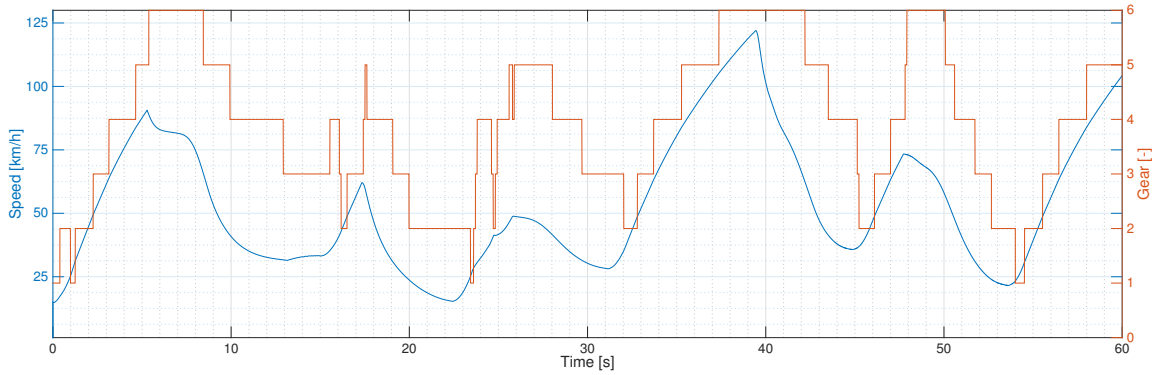

Figure 74: Vehicle's velocity and gear selection around the test track

The lap around the track is achieved in approximately 60 [s]. Even in this non-optimized model, gears

are selected to take advantage of the engine brake or to settle a base speed suited for quick acceleration if it is required by the *Driver*.

The instantaneous fuel consumption is shown in Figure 75 alongside with the acceleration.

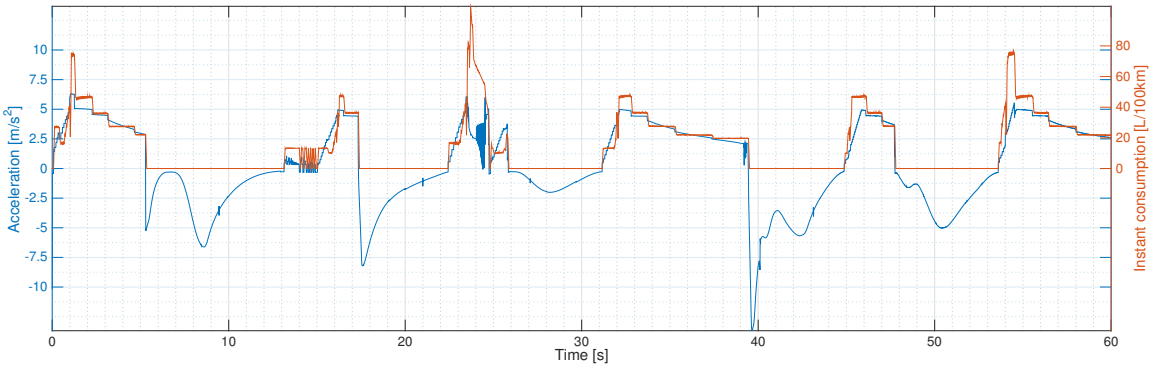

Figure 75: Vehicle's acceleration and instantaneous fuel consumption around the test track

The mean fuel consumption observed is around 15.79 [l/100km]. Recall that if it may appear as a quite high value for today's standard, this is the consumption of a non optimized 2.0 [l] atmospheric petrol engine with fixed ignition and valve timing, used without restrain by a sub-optimal *Driver*.

Because the *Driver*'s model was designed to be non predictive, no controller of speed was attributed to it. Therefore, around $t = 14[s]$, hesitation on the velocity to adopt in order to take corner between check-points 3 and 4 is observable resulting in oscillations between braking (negative acceleration) and accelerating.
Speaking of braking, degressive pedal pressure is applied according to the turn's curvature as the acceleration is firstly powerful and then decreases.
A peak in the fuel consumption is also observed around $t = 24$ [s] due to the triggering of the ESP. Indeed, arriving at the second corner of the chicane (between check-points 5 and 6 in Figure 73), the vehicle starts to slide when reaccelerating; the differential then switches in limited slip mode and ESP is on. This cause a quick deceleration without change in the ICE throttle (as if the *Driver*'s foot was still on the accelerating pedal), and the instantaneous consumption rises considerably.
These figures show appreciable dynamic excitations of the vehicle with hopefully more realistic results than the usual driving cycles. However, in this case, accelerations seem a little agressive for comparison with an everyday use. What is more, is the possible study of the vehicle's behaviour in cornering and eventually a pragmatic use of both engines.

Concerning their respective operating points, figures 76 and 77 display those on both motors' efficiency maps (BSFC for the ICE).

Here, one can observe the good functioning of the PSD as it optimizes the torque split for consumption minimization. Indeed, it is observed on Figure 76 that the ICE essentially stays in the highest efficiency operating region, i.e. where producing 1 [kWh] of thermal energy costs the least fuel. Of course, transitions are sometimes made in sub-optimal regions, typically as the engine starts, but all in all, sort of a "stairway" seems to lead to the top of the BSFC as the gears are changed.
As aforementioned, engine brake is also taken advantage of.

As far as the ETM is concerned, the region of best efficiency and highest torque output is vastly exploited. A security limiting the current to 95 [%] of its maximum value implemented in order to avoid overcharge seems respected, limiting the torque to 0.95 $C_{etm,rated}$ [Nm]. In generator mode, the ETM itself is no longer controlled by the PSD but by the *Brakes* box directly. The latter considers regenerative braking as "free" energy, thus regardless to its efficiency.

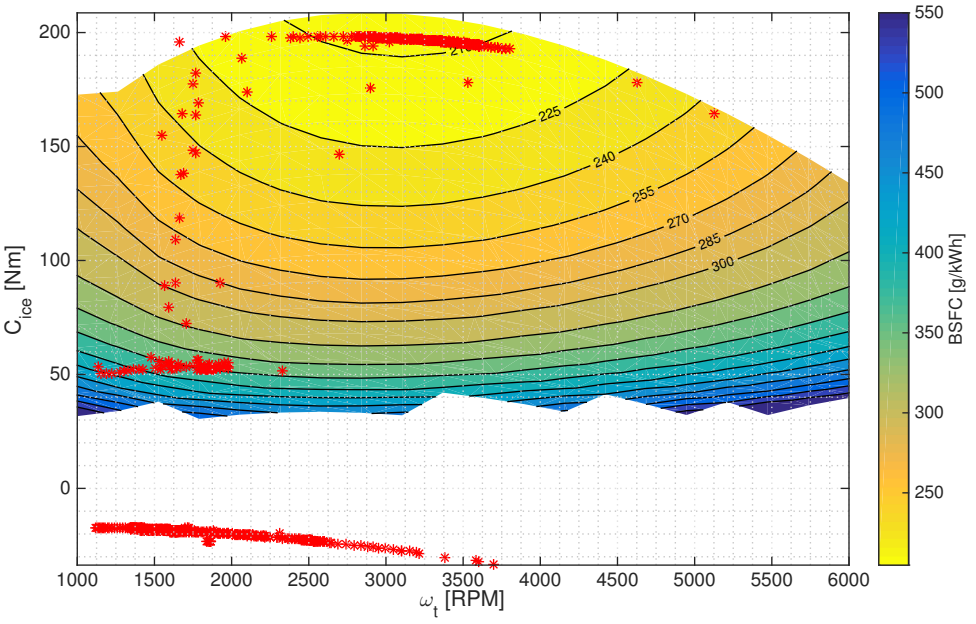

Figure 76: Example ICE BSFC and operating points on the test track

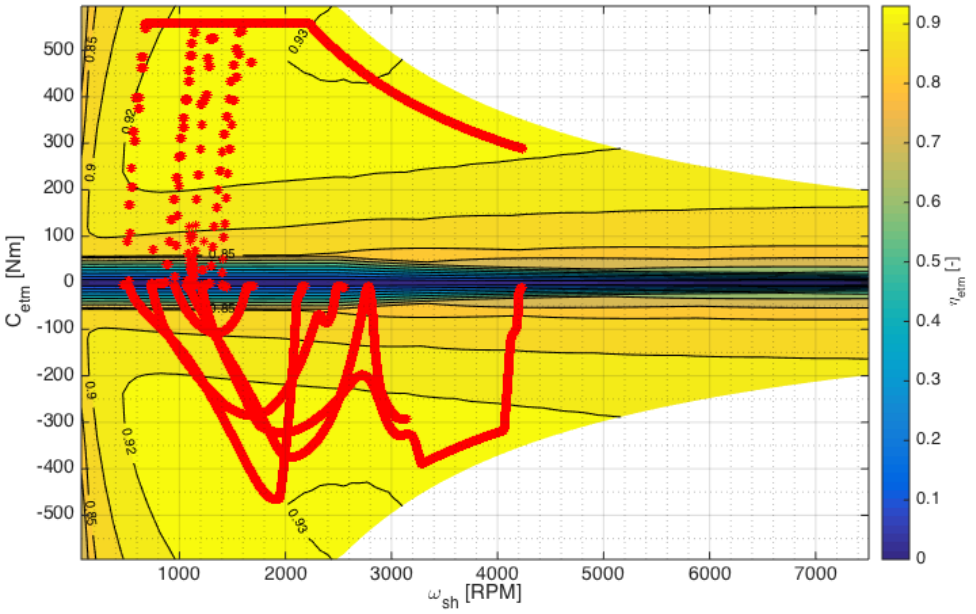

Figure 77: Example ETM efficiency map and operating points on the track

3 Global Optimization

After discussing the performances of vehicles and how to evaluate them, it is logic continuity to consider optimization regarding those performances. For this, a certain amount of parameters have been classified, and elected (in red) throughout the first part of this report. This chapter presents the methodology followed in order to process them and find the value most suited to minimize the global performance objective function.

3.1 Optimization Methodology

The global optimization methodology was originally designed by Aubain Verlé and presented as part of the ECCOMAS Thematic Conference on Multibody Dynamics that took place at the end of June 2015 in Barcelona (Spain) [5]. This chapter is just a synthesis of the process used in this work, not a new definition of it.

The goal of the method is obviously to minimize a global performance objective function evaluated around a reference track. For this, the loop shown in Figure 78 is repeated after each simulation or *trial* with a new genetically updated set of parameters $\underline{p_{optim}}$. Those are supposed to evolve and ultimately converge to their most suited value, i.e. minimizing the objective function.

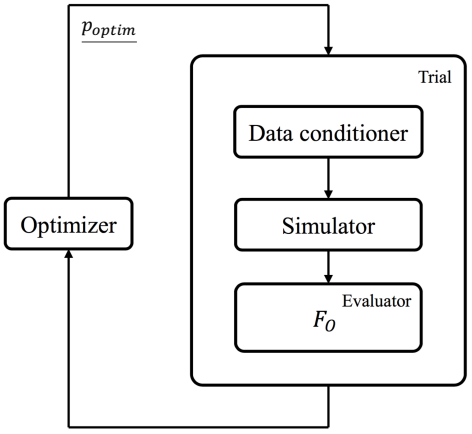

Figure 78: General optimization scheme [5]

A *trial* evaluates the objective function F_O in three main steps:

1. The **data conditioner** computes the values of non-optimized parameters in order to match some design contraints. For instance, some dimensions must be round numbers such as the number of cylinders constituting the ICE, or of permanent magnets in the ETM. Those are thus adapted from the continuous "floating" values recovered in $\underline{p_{optim}}$. The conditioner then forms an equivalent vehicle - possibly optimal - to be characterized by simulation.

2. The **simulator** runs the candidate vehicle on the reference track via a time simulation.

3. The **evaluator**, as its name implies, evaluate the objective function with data results from the simulation and, this way, characterizes the current candidate vehicle.

3.2 Optimizer

With 34s optimization parameters of different kinds, it is very unlikely that the system described in Part I will be convex as it stands. The algorithm elected to find the optimal solution is of non-deterministic evolutionary type and is called the Covariance Matrix Adaptation Evolution Strategy (CMA-ES) [29]. At each generation, this genetic algorithm selects N candidate vehicles or particles characterized by their corresponding vector of parameters $\underline{p_{optim,I}}$, and based on evolutionary analysis of the previous ones. Actually, the optimizer does not directly deal with $\underline{p_{optim}}$ but rather with a normalized, adimensionalized version $\underline{\tilde{p}_{optim}}$ of which components have value $\tilde{p}_{optim,i} \in [0\ ;\ 1]$ [-] defined as:

$$\tilde{p}_{optim,i} = \frac{p_{optim,i} - p_{optim,min,i}}{p_{optim,max,i} - p_{optim,min,i}} \tag{114}$$

Where the minimum and maximum values $p_{optim,min,i}$ and $p_{optim,max,i}$ have been chosen as range limits for the i^{th} optimization parameter.

The process is stopped when convergence is met. Convergence is defined either by the evaluated objective function's variation lower than a given threshold (10^{-2} here) or because the norm of $\underline{\tilde{p}_{optim}}$ [-] fluctuates below another given threshold (10^{-2} too).
Note that, experience has shown that better convergence is ensured by a number of particles $N >$ 2 size($\underline{p_{optim}}$).

3.3 Data Conditioner

Algebraic constraints

Algebraic relations are used to floor or round certain quantities in the parametrized model and also to assure symmetry of the chassis by copying data associated to the left part on to the right sided components (with possible change of sign).

Geometric constraints

If geometric adaptation of the suspension mechanism is considered in the dynamic performances optimization of the vehicle on track, some mechanical design constraints appear in order to ensure multibody loop closure. It was decided to restrict optimization to the non-multibody ("user") models and keep the car's chassis as it is.

3.4 Simulator

Multibody simulation

As aforementioned, the optimization methodology relies on multibody simulation of the modeled vehicle. This is achieved in the UCL's proprietary environment *Robotran* ©. Recall that the advantage of multibody simulation regarding "simpler" longitudinal study of performances, is to observe its inertia and the dynamic with which the vehicle take curves. The difficulty is to obtain an adaptative strategy of control so that the car stays on the track.

Firstly, the chassis' morphology (type of joints, suspension, steering mechanism, etc) is defined by preliminary mechanical design in $MBSysPad$, the graphical editor program of *Robotran* © suite. From this first description, movement equations can be generated by the software called $MBSysTran$ in order to provide symbolic C-function for the mass matrix $\mathbf{M}$ [kg], the dynamic vector of external forces $\mathbf{c}$ [N]; the constraints $\mathbf{h}$ and the jacobian matrix of constraints $\mathbf{J}$ to build the following differential algebraic equations (DAE) system:

$$\mathbf{M}(q)\,\ddot{q} + \mathbf{c}(q,\dot{q}) = \mathbf{Q}(q,\dot{q}) + \mathbf{J}^T\,\lambda \tag{115}$$

$$\mathbf{h}(q) = 0 \tag{116}$$

$$\dot{\mathbf{h}}(q,\dot{q}) = \mathbf{J}(q)\,\dot{q} = 0 \tag{117}$$

$$\ddot{\mathbf{h}}(q,\dot{q},\ddot{q}) = \mathbf{J}(q)\,\ddot{q} + \dot{\mathbf{J}}(q,\dot{q})\,\dot{q} = 0 \tag{118}$$

The system allows to find the joint forces $\mathbf{Q}$ [N] and resulting movement. q are the joint generalized coordinates of the multibody system (mbs).
With the best set of independent q_u and dependent coordinates q_v, the coordinate partitioning method is used to transform the previous DAE system into a reduced (red index) ordinary differential equations (ODE) system. The number of degrees of freedom of the mbs is given by the number of q_u. After some matrix manipulations, the reduced system is expressed as [1]:

$$\mathbf{M}_{red}\,\ddot{q}_u + \mathbf{F}_{red}(q_u,\dot{q}_u) = 0 \tag{119}$$

From that point, general equilibrium solution for $\mathbf{F}_{red}(q_u) = 0$ [N] can be found by the iterative Newton-Raphson (NR) method.

And then time simulation can begin following the scheme described in Figure 79. At each time-step, "The direct dynamics module is based on a time integration of the mechanical dynamics equations 119 and of the user model (Part I) state equations. The variables of this time integration are the independent coordinates q_u and the user model states z. A fixed time step Runge-Kutta method is used with a time step of $2 \cdot 10^{-4}$ [s]" [5].

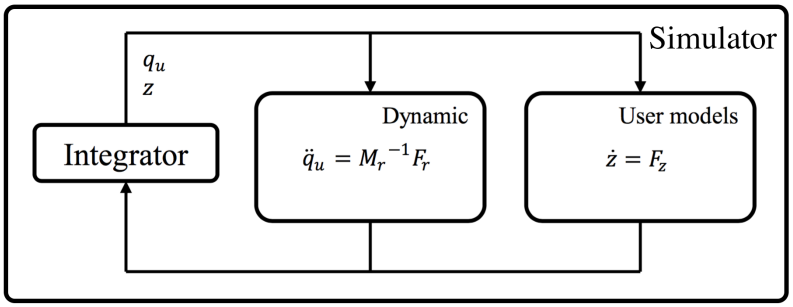

Figure 79: Multibody simulation scheme [5]

Reference track

The simulation is run on a reference track. This trajectory should be designed to excite the dynamic properties of the generated candidate vehicle as extensively as possible. However, as genetic optimization of multiple parameters can take quite a large number of trials, those should not take more than 1 [min] of "real" time each. So if the chosen circuit shown in Figure 80 appears simple looking like a patatoïd; because of its shortness (the test trajectory is only 900.21 [m] long), it is actually quite hard to maneuver, with straight lines for higher speed performances and sort of a chicane between check points 4 and 6.

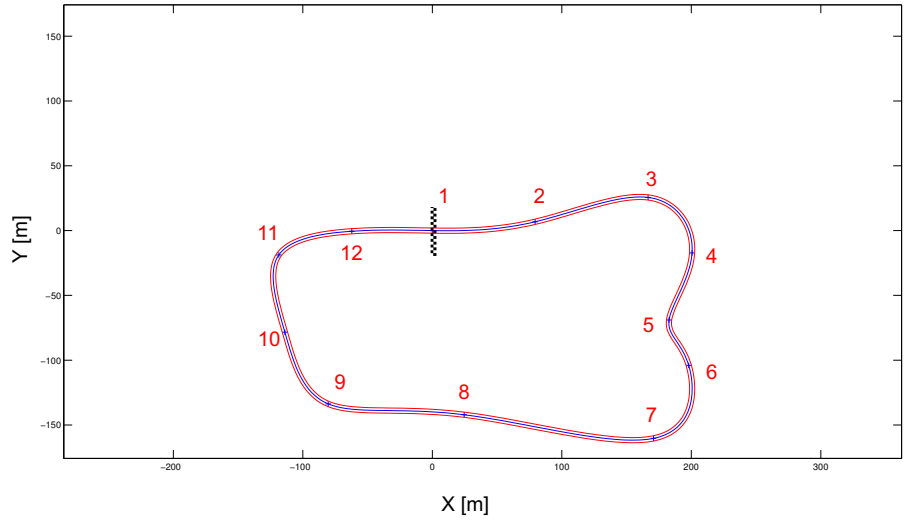

Figure 80: Reference track for dynamic performances testing

3.5 Evaluator

Passing the last check-point of the track, the simulation ends and the objective function can be evaluated. As introduced in the previous section, the **objective function** to minimize is clearly application-dependent. It represents a particular use for the hybrid vehicle assessing its quality criteria regarding dynamic performances via the lap time t_{lap} [s] and fuel economy via the energy consumption (thermal E_t and electric E_e [J]):

$$F_O = t_{lap} + \alpha_{F_O} \, s_{F_O} \sqrt{E_t + E_e} \tag{120}$$

Recall that the energy uses are expressed as:

$$E_t(t) = \int_0^{t_{lap}} LHV(\tau)\ \dot{m}_\phi(\tau) d\tau \tag{121}$$

$$E_e(t) = \int_0^{t_{lap}} E_{bat}\ \dot{SOC}(\tau) d\tau \qquad \text{with } E_{bat} = 3600 Q_{bat,0}\ U_{bat,0} \tag{122}$$

$s_{F_O} = 1.8 \cdot 10^{-2}$ [s/J] is an equivalence ratio between those and the lap time designed to shape and size the criteria to the same order.

The fact that the energy use $(E_t + E_e)$ [J] is attributed of an 1/2 [-] exponent comes from the relation - already suggested by Figure 75 - that the fuel consumption [l/100km] is quasi directly proportional to the acceleration [m/s^2]. Fuel consumption in [l] - which is equivalent to a quantity of energy in [J] via the LHV and fuel density - therefore is proportional to [m^2/s^2].

$$\frac{\Delta V_\phi}{\Delta x}\ [\text{l/m}] \propto a_x\ [\text{m/s}^2] \qquad \Longrightarrow \qquad \Delta V_\phi\ [\text{l}] \propto a_x\, \Delta x\ [\text{m}^2/\text{s}^2] \tag{123}$$

$$\Longrightarrow E_t = \rho_\phi\ \Delta V_\phi\ LHV\ [\text{J}] \propto a_x\, \Delta x\ [\text{m}^2/\text{s}^2] \tag{124}$$

The lap time, itself, for a fixed travel (900.21 [m]) is dependent of the mean speed [m/s] on the track. In consequence, the presence of the square root in (120) is justified for both terms to be of the same order [m/s].

Finally, to be complete in the definition of the objective function (120), α_{F_O} [-] itself determines the application that the *driver* and his HEV are destined to.

- $\alpha_{F_O} < 1$ [-] defines more sportive applications where energy consumption is less important than the output performance on the track
- $\alpha_{F_O} = 1$ [-] would be a measured application where the optimal solution is an economical but quick vehicle
- $\alpha_{F_O} > 1$ [-] stands for more economical applications where energy consumption is minimized regardless of the time to endure one lap

Also, it may appear that the candidate vehicle simply fails to reach the end of the track. Several situations have been identified for which the simulation has to be stopped and the objective function is chosen inversely proportional to the distance travelled and weighted so that it renders a worse quality vehicle than any that would be able to reach the finish line.
The possible reasons for simulation failure are:

- The vehicle eventually becomes uncontrollable because wheels are locked in braking or slide in accelerations. So the simulation ends if the vehicle deviates by more than 1 [m] from its predefined trajectory.
- Also related is the fact that the steering angle cannot take any value or else the mechanism would block. The rack-and-pinion gear displacement is thus limited $|\Delta_{rp}| \leq 7.5$ [cm] against an eventual demand by the steering controller in case of lane departure (sign of bad dynamic performances).
- The temperature reaches dangerous levels in the electric motor (the ICE model not having any thermal modeling). It is estimated that the temperatures in the windings $T_w \leq 500$ [°C] and in the permanent magnets $T_{PM} \leq 200$ [°C] are critical.
- Bakker tire-to-ground model is not valid at too slow speeds. Then, if the vehicle's velocity falls under 10 [km/h], the simulation is stopped because judged unrealistic.

Part III

Results and Discussion

1 Introduction

During the entire development of this work, it was believed that hybrid electric vehicles should not be parametrized loosely, regardless of their definitive application on the roads. For this, a global and rather complete HEV simulator (in the sense that it includes most of all sensitive subsystems) has been elaborated and a strategy to optimize it was recovered and adapted from another work led at the University.

In this last part, the objective thus remains to study the performances of optimized hybrid electric vehicles according to their respective use.
The methodology followed in order to achieve this parametrical study was firstly to elect differently parametrized vehicles each representing a potential and diversified use. As mentioned in Part II, the parameter defining this potential application is the weight attributed to energy use with regards to the lap time in the objective function of the optimization process. A sensitivity analysis on this precise bias was thus performed in order to elect three HEV on which thorough performances study would be interesting.

As expected, the global model proved to be very poorly convex and segmentation of the parametrical optimization was considered. After multiple iterations[9] on the various subsystems of the elected HEV, it was admitted that 3 optimal solutions to their particular use were found. Full characterization of those models are given in the respective chapters of this part.

Finally, conclusions were taken regarding optimal hybridization of the powertrain for various uses. Conclusions which are quite interesting to compare with the general tendency adopted by car manufacturers for what looks like an unrestricted energy transition in the way vehicles are propelled today.

[9]Computational resources have been provided by the Consortium des Équipements de Calcul Intensif (CÉCI), funded by the Fonds de la Recherche Scientifique de Belgique (F.R.S.-FNRS) under Grant No. 2.5020.11

2 Application Selection

After having built a global scheme of the hybrid electric vehicle with its most sensitive sub-systems, the idea, as mentioned previously, is to optimize it according to a specific use. As optimization on a set of multiple and various parameters can be quite a heavy-duty process, the idea was to select 3 different uses (i.e. 3 biases α_{F_O} [-]) for the vehicle.
In this objective of selection, the first step is to analyse the spectrum of possibilities that the modeled HEV offers. Indeed, in Part II, the variable weight α_{F_O} [-] was introduced to compare the two criteria for performance evaluation: lap time and energy use.

2.1 Parametrical Sensitivity Analysis

In order to provide noticeable performances' differences, 7 optimizations were performed online[9] with weights α_{F_O} [J/s] on a limited set of parameters: the total ICE displacement $V_{cc,tot}$ [cc], the minimum and maximum rotation speed at which gear changes are forced $\omega_{t,min}$ and $\omega_{t,max}$ [RPM] and the global dimensions of the ETM R_{os} [m], R_{ir} [m] and S_{Cu} [mm^2] for the outer stator radius, the inner rotor radius and the copper wires' section respectively.

$$\text{Optimization performed on } \underline{p_{optim}} = [V_{cc,tot}\ ;\ \omega_{t,min}\ ;\ \omega_{t,max}\ ;\ R_{os}\ ;\ R_{ir}\ ;\ S_{Cu}] \tag{125}$$

$$\text{with } \underline{\alpha_{F_O}} = [10^{-3}\ ;\ 10^{-2}\ ;\ 10^{-1}\ ;\ 1\ ;\ 10^{1}\ ;\ 10^{2}\ ;\ 10^{3}] \tag{126}$$

It would not be relevant to look for sensitivity regarding $\alpha_{F_O} < 10^{-3}$ [-] as variations of the second criteria (equivalent energy consumption) would fall under the threshold of 10^{-2} for the evaluation of the objective function.

Note also that, unfortunately, at first, no optimization of the *Driver*'s box could be completed because of its behavioural sensitivity on the track. Indeed, genetic trials on combinations of critical parameters such as security distance and maximal loading (braking or throttle), even with a limited range of authorized values, were simply prohibitive.

For the optimization processes that could be achieved, the results of criteria evaluation are shown in Figures 81 and 82 in terms of the objective function's bias α_{F_O} [-], the latter being presented in logarithmic values for better readability.

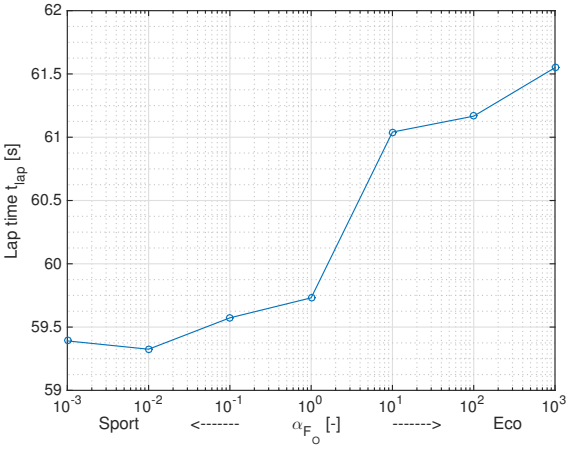

Figure 81: Lap time [s] vs α_{F_O} [-]

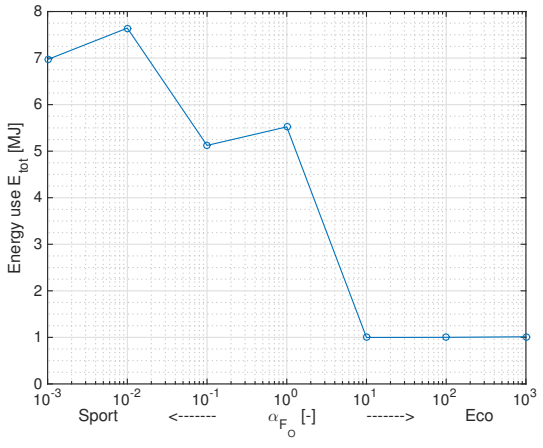

Figure 82: Energy use [MJ] vs α_{F_O} [-]

When observing those quite chaotic results, one can at least notice a tendency to saturation of the energy use in the region $\alpha_{F_O} > 10^2$ [-]. This is in fact due to limitations imposed on the electric motor/generator. Indeed, when fuel economy is fully privileged regarding the lap time performance, the optimizer proposes

a powertrain structure with maximum electric capability (as a motor but also as a generator). This capability is however limited by the maximum energy transfer (current) allowed at the non-optimized battery.

For the rest, the popular intuition that a more sportive use ($\alpha_{F_O} > 10^0$ [-]) - and therefore better lap-times - requires more energy and its opposite for economical use ($\alpha_{F_O} > 10^0$ [-]) seems respected. The general trend is thus: as α_{F_O} [-] is increased, the lap time follows while the energy use is reduced. Perhaps two outliers appear as an objective biased by $\alpha_{F_O} = 10^{-1}$ [-] relies on slightly less energy than $\alpha_{F_O} = 10^0$ [-]; and $\alpha_{F_O} = 10^{-3}$ [-] takes a little more time than $\alpha_{F_O} = 10^{-2}$ [-].

2.2 Hot Lap Energy Cost

What may be more interesting from an energetic point of view, is to approximate the consumption of a desired lap time.
The results of this first set of optimizations are interpolated with shape preservation and displayed on Figure 83 exposing the link between different vehicles energy uses to their respective lap time, for a same non optimized *Driver*.

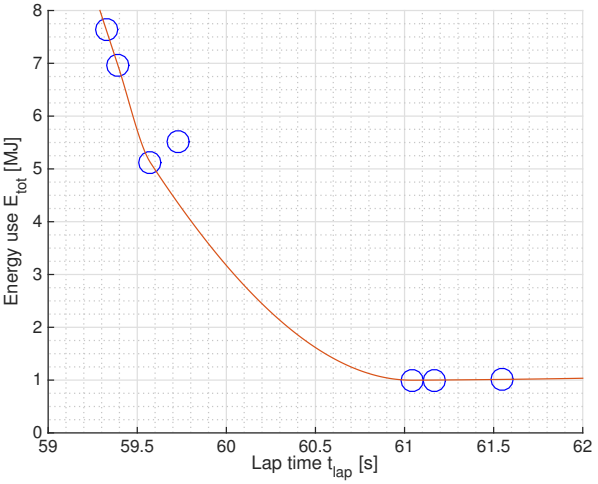

Figure 83: Lap time [s] vs. Energy use

The quickest lap times show quasi asymptotic behaviour of the consumption as it becomes, in relative, more and more energy costly to improve performances on a short track such as the reference circuit. On the other side, even when economy is limited by dimensioning factors (only one electric motor, battery size fixed), it is always possible to take more time to complete one lap.

Of course, the curve 83 would not be valid if a different driver was considered for each application.

2.3 Objectives selection

Taking in consideration the conclusions of the previous sections, it is time to make a careful choice of the objective function biases α_{F_O} [-]. For the sake of processing load and available time, it was decided that only 3 dedicated vehicles would be fully optimized.
Their respective application must be as distinct as possible, however feasible for a hybrid electric vehicle, and are defined in Table 13.

Use	Economical Use	Neutral Driving	Sportive Use
α_{F_O}	10^2	10^0	10^{-2}

Table 13: Chosen HEV application definitions

3 Common Values

3.1 Stiff Optimization Parameters

Before beginning the global optimization process, the first step was obviously to test each parameter individually following the methodology defined in Part II, chapter 3. However, some revealed to have a quite stiff behaviour in the genetic trials or simply to have far less influence on the dynamic vehicle performances than expected. All in all, varying their values resulted either by non-convergence of the objective function evaluation, or by crashing of the process. For those reasons, it was decided to fix them at functioning (though probably sub-optimal) values. Those values are given in Table 14 and are thus the same for any application mentioned below.
Some hypotheses were ultimately assumed to explain the failure of the model regarding those parameters.

1. The permanent magnet's thickness is supposed to influence the intensity of the magnetic B-field of the PM. However, e_{PM} [mm] being closely limited by the rotor's outer and stator's inner radii (for good dimensions of the coils), its influence on B_{PM} [T] is relatively small in comparison with that of the temperature profile in the motor (see Figure 112).
2. The number of slots per pole and per phase being fixed to $S_{pp} = 2$ [-], the number of pair of poles p [-] in the ETM's rotor has become particularly critical in the sizing of the statoric resistance. Indeed, if too small, without further limitation on the stator's dimension, the size of the slots can become pretty massive and the number of loops in the coils n_c [-] increases, boosting by the way the statoric resistance. The same phenomenon appears with p [-] too large as the slots are imposed very thin, therefore reducing the wires' cross section (see equation (129)).
3. The ETM's length l_r [mm], if too large can create problems in the air flow destined to cool the structure; if too small, more than being endangered by vibrations in the motor shaft, the ETM may not have sufficient "exchange surface" for the magnetic fields to create a sufficient torque.
4. In the ICE, it has been preferred to fix the valve timing before optimization in order to significantly reduce the complexity of the process. Indeed, optimal valve timings are speed related. However the engine speed is linked to the gearbox logic, differential, driver's decisions, etc., making fixed valve timings systems very difficult to optimize.
5. An adjusted braking can provide significant differences in the dynamic behaviour of the car on the track: for good or for bad. After multiple attempts (and failures) to limit the range of values possible for parametrical optimization of the braking system, it was decided to go for a better management, via the *Driver*, of a fixed arrangement rather than modify its sizing.
6. As the reference track is the same for all three applications, the differential repartition in torque vectoring mode is quite the same also.
7. Still concerning the reference track, being so short, the quasi straight lines do not allow high profile of speed (rarely exceeding 100 [km/h]), and the corners are all quite slow. Therefore the vehicle's dynamic behaviour is not noticeably influenced by aerodynamic add-ons.

ETM			ICE			
e_{PM} [mm]	p [-]	l_r [mm]	$\theta_{i,o}$ [°]	$\theta_{i,c}$ [°]	$\theta_{e,o}$ [°]	$\theta_{e,c}$ [°]
30	4	400	360	540	140	360
	Brakes		Differential	Aerodynamics		
	$R_{b,f}$ [mm]	$\frac{R_{b,r}}{R_{b,f}}$ [-]	k_{vec} [%/mm]	$C_{L,add}$ [-]	x_L [m]	
	200	1/2	1.07	-2.0	-0.05	

Table 14: Common HEV parameters for all application

What is more, the same chassis (1200 [kg]) has been considered for all three applications; with correction of the suspension and roll-bar stiffnesses based only on the vehicle's total mass. No optimization of the camber- and toe-angle were examined in this last part of the work.

4 Economical Use

The first HEV application under study here is perhaps the reason it has been introduced on the passenger's car market: fuel economy. Indeed, as already much repeated, the addition of an electric motor/generator in the powertrain structure facilitates optimal use of the traditional combustion engine and ultimately reduce its energy consumption for the same journey. This study is led on a vehicle parametrized by optimization of the objective function (120) biased ($\alpha_{F_O} = 10^2$ [-]) towards minimization of the energy use on the reference track.

4.1 Vehicle Specification

The results of the multi-parametrized optimization are given in Table 16 for an overall power-split:

Thermal		Electrical	
$P_{ice,max}$ [kW]	$C_{ice,max}$ [Nm]	$P_{etm,max}$ [kW]	$C_{etm,max}$ [Nm]
22.44 @ 5158 [RPM]	52.16 @ 2842 [RPM]	224.41	857.2

Table 15: HEV optimal power-split for economical use

First of all, it has to be noted, regarding Table 15, that the lower limit to the thermal use of the HEV has been reached. This means the *optimizer* would probably have proposed a still smaller ICE than a 500 [cc] mono-cylinder if it were allowed to. One can conclude that though this study concerns HEV, the optimal vehicle for total energy economy is fully electric. Keep in mind nevertheless that this is a work of simulation with hard hypotheses such as the "gratuitousness" of electricity (which is actually not free. But not the subject either). The ICE can thus be considered here as a mandatory auxiliary for the application that therefore does not need an ETM more powerful than 224.41 [kW].
The global optimization of the ETM size is also effectively limited by the battery weight. Supplying higher power indeed means a greater number of cells ultimately making the battery's weight critical for the performances of the vehicle on the track. The total mass of the HEV is indeed 2268 [kg] (53 [%] for the battery).
The optimized *Driver* is quite cautious circulating around the track; with light loading not exceeding 70 [%] of the maximum throttle, and starting to brake at twice the stopping distance at least. The differential and the gearbox logic have been manipulated to keep the powertrain structure at low speeds where the torque is maximized rather than the power output, assuring lower energy consumption but also less resources for sudden accelerations.

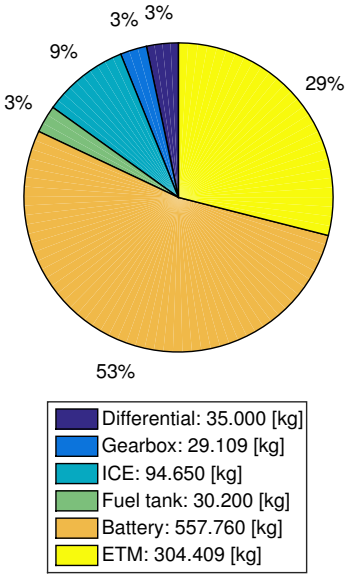

Figure 84: Repartition of the masses in the hybrid powertrain destined to an economical use

Driver					ETM		
k_a [1/s]	k_{max} [-]	k_{secu} [-]	k_{turn} [m]	k_v [1/s]	R_{ir} [mm]	R_{os} [mm]	S_{Cu} [mm^2]
0.5	0.7	1.0	15	0.75	73	183	7.45
	Battery		ICE		Differential		
	$U_{bat,0}$ [V]	$Q_{bat,0}$ [kAh]	$V_{cc,tot}$ [cc]	θ_s [°]	i_{diff} [-]	t_{diff} [%]	
	390.0	15.120	500	-15	3.2	29	
Gearbox							
$\omega_{t,min}$ [RPM]	$\omega_{t,max}$ [RPM]	$i_{g,1}$ [-]	$i_{g,2}$ [-]	$i_{g,3}$ [-]	$i_{g,4}$ [-]	$i_{g,5}$ [-]	$i_{g,6}$ [-]
1812	3005	3.5	2.2	1.7	1.3	1.05	0.95

Table 16: HEV parametrization for economical use

4.2 Performances Study

Pure performances

Test	$v_{Max} = 194.940$ [km/h]	0-100 [km/h]	40-120 [km/h]	100-0 [km/h]
Time [s]	25.065	9.1027	8.563	2.845
Distance [m]	871.331	116.721	185.168	39.517

Table 17: Pure performances test results

As an illustration, pure performances numbers are given in the Table 17 for longitudinal testing. The results are quite appreciable for a vehicle this heavy, greatly helped by the high starting torque of the ETM and its support to braking in generator mode.

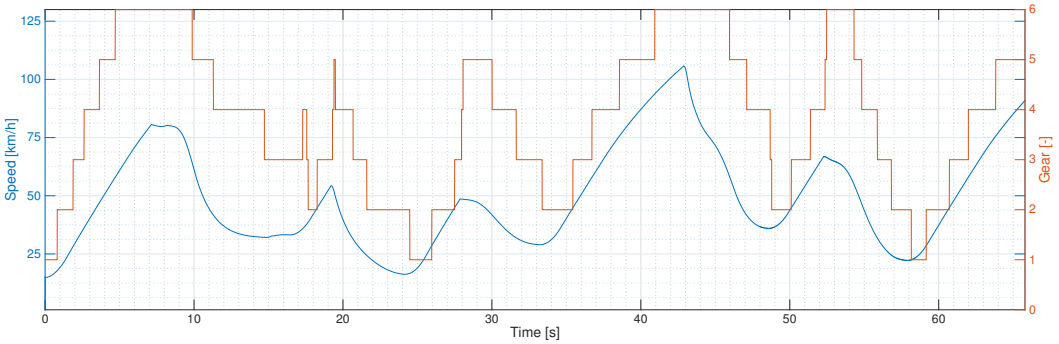

Figure 85: Eco HEV velocity and gear selection around the test track

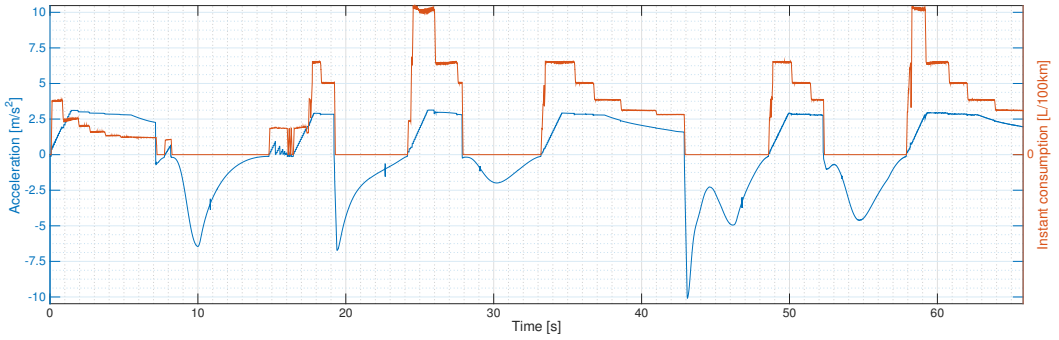

Figure 86: Eco HEV acceleration and instantaneous fuel consumption around the test track

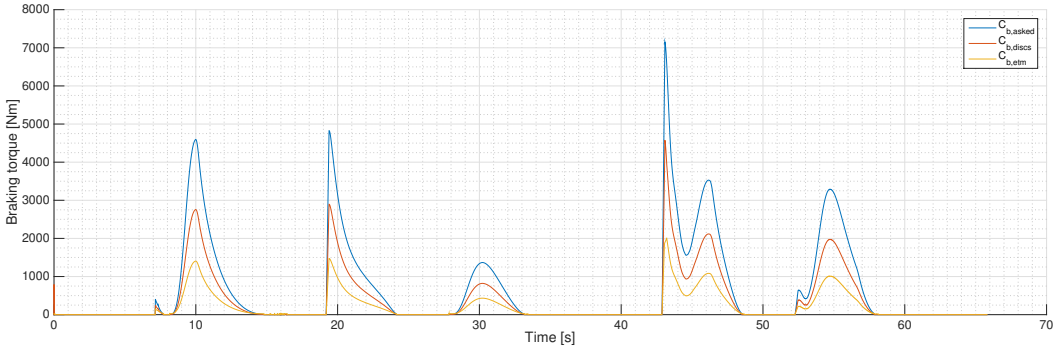

Figure 87: Eco HEV braking points on the test track

Reference lap

In Figure 85, one can observe a quite slow speed profile as one lap is completed in 65.795 [s]. Gears are changed accordingly and in order to keep the ICE in its best efficiency region (see BSFC 89). Around $t = 17$ [s], the progressive reloading ($k_a = 0.5$ [1/s]) make the gearbox controller hesitant whether demanded acceleration requires downshift or not.
A great deal of the braking load in Figure 87 is assured by the powerful ETM in generator mode, but the lightness of this load - due to the *Driver*'s cautious behaviour - makes total regenerative braking not exceed 0.75 [MJ] $\approx$ 0.208 [kWh]. Still, this represents 12 [%] of the total energy required to perform the reference lap in the given time.
The total energy use is 5.81 [MJ] = 1.614 [kWh] $\overset{eq}{=}$ 0.193 [l] of gasoline for a mean fuel and net electrical consumption of:

Fuel consumption	Electrical discharge
3.89 [l/100km]	1.244 [kWh/km]

Table 18: Mean energy uses around the test track

Electrical consumption appears high at first. This may be explained by the great variations of speed (ETM directly coupled to the wheels via the differential) and the fact that maximal throttle is at 0.7 [-] maintaining the ETM in sub-optimal regions of operation.

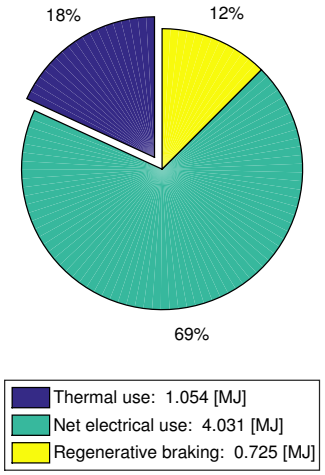

Figure 88: Repartition of the energy used to overcome one lap around the test track

Operating points

As suspected earlier, the whole powertrain is here optimized to be operated at low rotation speed. Regarding the thermal path (Figure 89), this translates in keeping the ICE in a high efficiency region around 3000 [RPM] and most of the time at full throttle. In the meantime, the electric motor assures transitions in an operating zone where its output torque is maximal. The *Driver*'s total demand never exceeding $k_{max} = 0.7$ [-], the ETM is not exploited at its full potential. At least not in motor mode because that is without mentioning regenerative braking climbing up to 600 [Nm] (1920 [Nm] on the rear wheel axle) for peak energy recovery around 3000 [RPM].

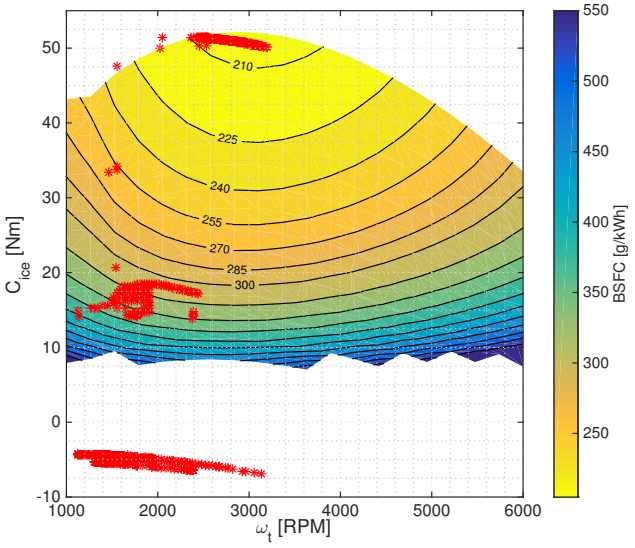

Figure 89: ICE BSFC with operating points around the track

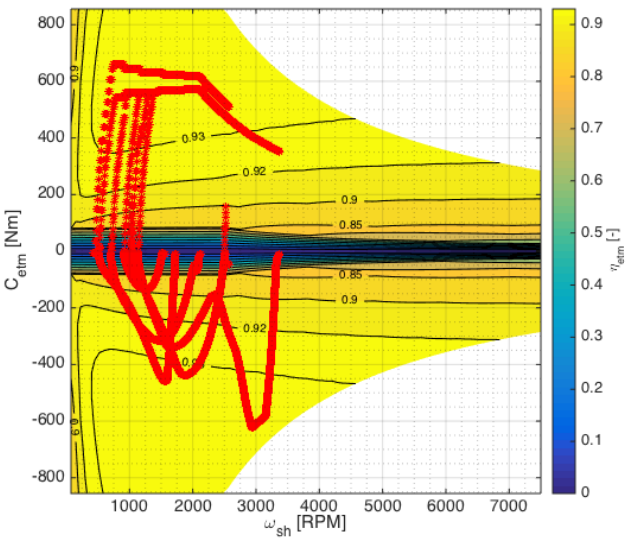

Figure 90: ETM efficiency map with operating points around the track

5 Neutral Driving

This second review concerns an "intermediary" vehicle destined to uses between economy and sportiveness. This "neutrality" is defined by non-bias ($\alpha_{F_O} = 1$ [-]) of the objective function.

5.1 Vehicle Specification

As the results shown in Table 19 suggest, the optimal repartition still favours the electrical solution by more than 2/3 of the total embedded power.

Thermal		Electrical	
$P_{ice,max}$ [kW]	$C_{ice,max}$ [Nm]	$P_{etm,max}$ [kW]	$C_{etm,max}$ [Nm]
71.91 @ 5158 [RPM]	167.5 @ 2842 [RPM]	168.18	642.4

Table 19: HEV optimal power-split for neutral use

As more importance is now attributed to the lap time than for economic use, the *Driver* is obviously a little more aggressive, pushing harder and quicker on the throttle. Also, the reduction of the security coefficients leads to some triggering of the ESP system (see Figure 94). Its use is actually preferred over that of the limited slip differential becoming quite redundant. Therefore the parameter t_{diff} [%] tuning the transfer of torque to the slower non-slipping wheel, is diminished. Speaking of the differential, its gear reduction ratio is also increased regarding its value in economic use. This means, at the same power output, more torque transmitted to the wheels at slower rotations. Gears operating range has increased and changes are globally less frequent (see Figure 92).
The vehicle's mass has decreased to a total of 2094 [kg] principally by reducing the battery capacity. Note that the operating voltage of the electrical path is still quite high with a DC bus at $1.5\,U_{bat,0} = 570$ [V] for optimal driving of the ETM.
What is also interesting to notice is that the ignition timing has been moved to keep the maximum torque output of the 4 cylinders 1.6 [l] ICE at the same rotation speed than in economic (and ultimately in sportive) use; supposedly optimal regarding the speed profile on the reference track.

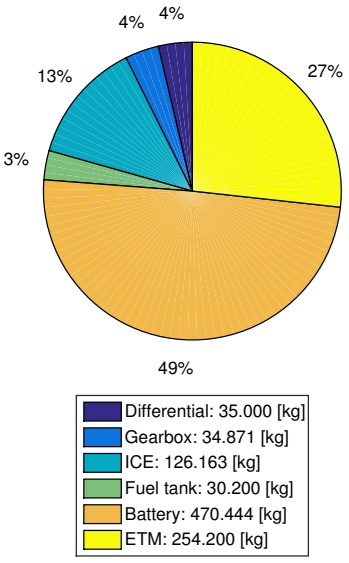

Figure 91: Repartition of the masses in the hybrid powertrain destined to a neutral use

Driver					ETM		
k_a [1/s]	k_{max} [-]	k_{secu} [-]	k_{turn} [m]	k_v [1/s]	R_{ir} [mm]	R_{os} [mm]	S_{Cu} [mm^2]
2.0	1.0	0.59	8.0	1.0	60	160	12.0
	Battery		ICE		Differential		
	$U_{bat,0}$ [V]	$Q_{bat,0}$ [kAh]	$V_{cc,tot}$ [cc]	θ_s [°]	i_{diff} [-]	t_{diff} [%]	
	380.0	12.753	1598	-11	4.5	6.0	
Gearbox							
$\omega_{t,min}$ [RPM]	$\omega_{t,max}$ [RPM]	$i_{g,1}$ [-]	$i_{g,2}$ [-]	$i_{g,3}$ [-]	$i_{g,4}$ [-]	$i_{g,5}$ [-]	$i_{g,6}$ [-]
2289	3704	3.5	2.2	1.7	1.3	1	0.8

Table 20: HEV parametrization for neutral driving

5.2 Performances Study

Pure performances

Test	$v_{Max} = 241.003$ [km/h]	0-100 [km/h]	40-120 [km/h]	100-0 [km/h]
Time [s]	59.599	5.853	10.225	2.627
Distance [m]	3167	87.688	293.004	36.484

Table 21: Pure performances test results

What is interesting to notice comparing the "neutral" HEV with the "economic" one, is that it is vastly quicker to perform 0-100 [km/h] but presents a relatively more concave acceleration profile as 40-120 [km/h] is achieved slower. Obviously, its reduced mass offers a great advantage in emergency braking.

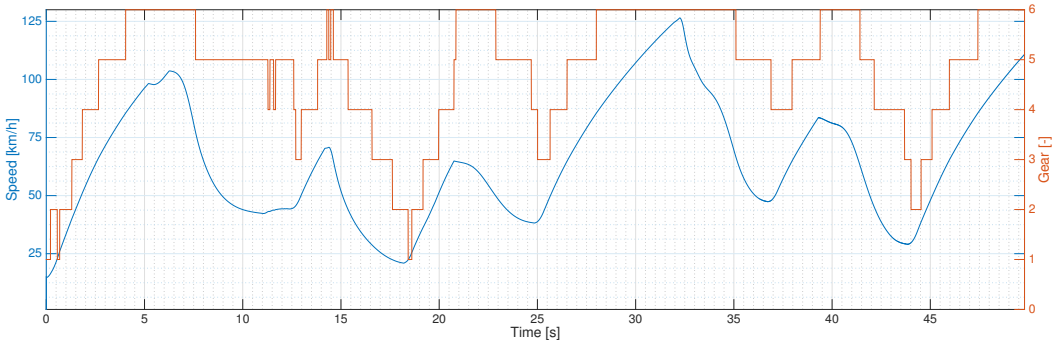

Figure 92: Neutral HEV velocity and gear selection around the test track

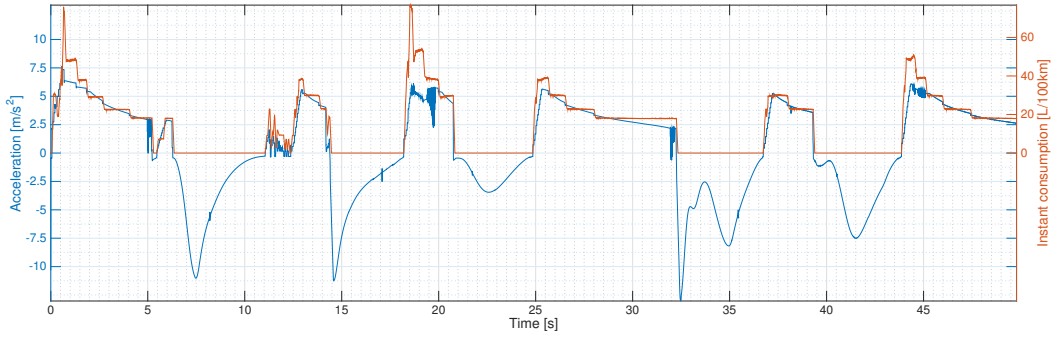

Figure 93: Neutral HEV acceleration and instantaneous fuel consumption around the test track

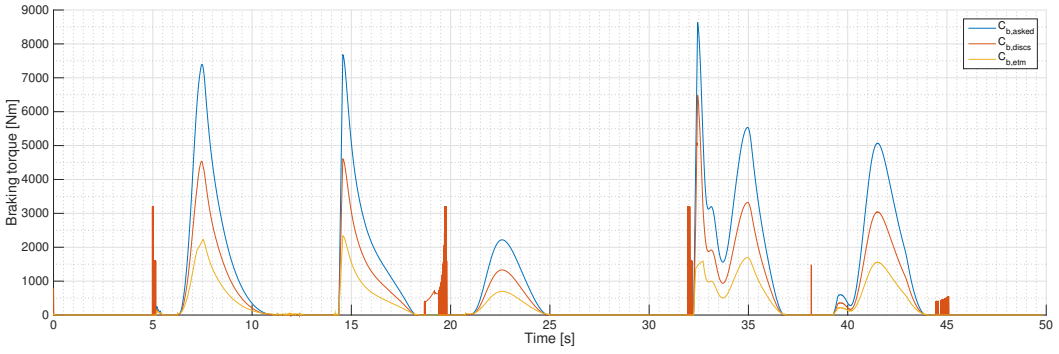

Figure 94: Neutral HEV braking points on the test track

Reference lap

Compared to Figure 85, the whole speed profile shown in Figure 92 has been shifted upwards. More than dropping the lap time to 49.795 [s], it had also a remarkable effect on the gear changes. For the corners' exits are now made at higher speed, there is no need to downshift in order to recover back-up torque for reacceleration anymore.
But this strategy has also the tendency to trigger the ESP as observable in Figures 93 and 94 but hopefully rarely for more than 0.5 [s].
From an energetic point of view, the ICE should now truly be counted as an integrated part of the powertrain. However, its use remains limited to 35 [%] of the total consumption: 10.893 [MJ] = 3.026 [kWh] $\stackrel{eq}{=}$ 0.362 [l] of gasoline. If one were to compare the mean consumption of both power path, one would find the results in Table 22

Fuel consumption	Electrical discharge
14.11 [l/100km]	1.858 [kWh/km]

Table 22: Mean energy uses around the test track

The advantage of hybridization becomes quite obvious when one compares those numbers to that of a traditional vehicle with a 2.0 [l] petrol engine "only". This one would virtually demand 7.01 [MJ] for completing one lap in 60.3 [s].

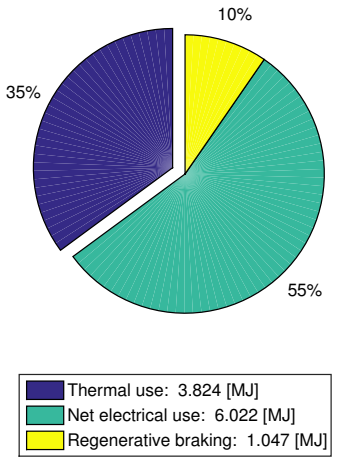

Figure 95: Repartition of the energy used to overcome one lap around the test track

Operating points

Concerning the points at which both engines are operated, the range is quite remarkably extended for the ICE as for the ETM confirming the well defined HEV intermediary status.

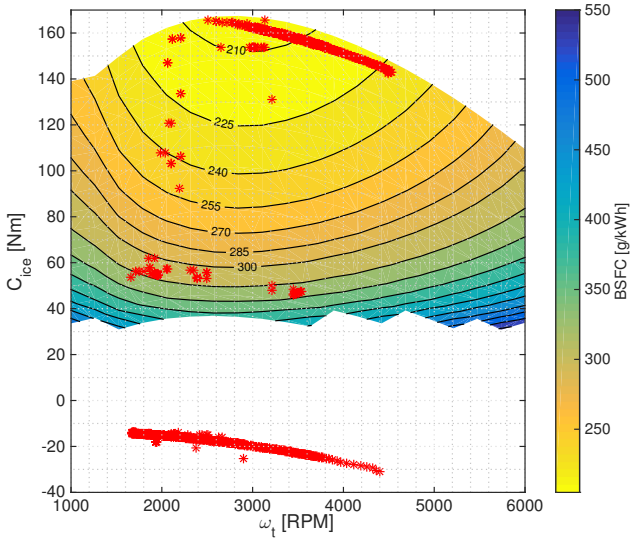

Figure 96: ICE BSFC with operating points around the track

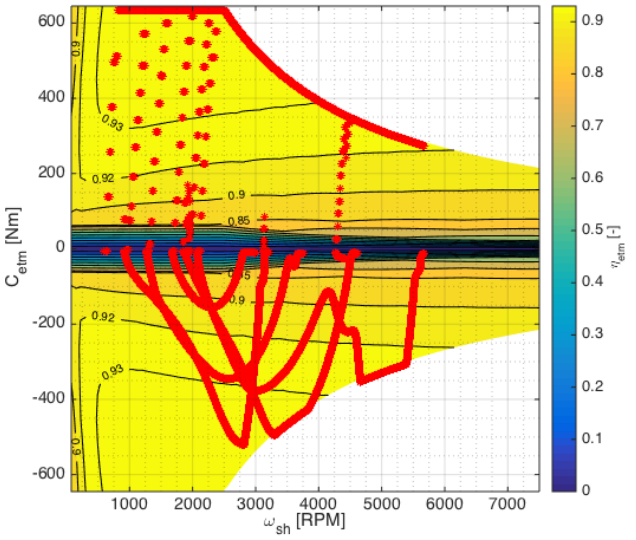

Figure 97: ETM efficiency map with operating points around the track

6 Sportive Use

For this last application, a more sportive HEV (destined to competition for example) was defined by optimization of the objective function biased with $\alpha_{F_O} = 10^{-2}$ [-]. This means quasi no regards to the consumption criteria compared to minimization of the lap time around the reference track.

6.1 Vehicle Specification

The results of the multi-parametrized optimization are given in Table 24 for an overall power-split:

Thermal		Electrical	
$P_{ice,max}$ [kW]	$C_{ice,max}$ [Nm]	$P_{etm,max}$ [kW]	$C_{etm,max}$ [Nm]
129.4 @ 5158 [RPM]	298.0 @ 2842 [RPM]	108.86	416.2

Table 23: HEV optimal power-split for sportive use

This is actually the only of the three fully optimized vehicles that embed more thermal than electrical power. The configuration is particularly favourable to a more lightweight structure. Indeed, this reorganization of the powertrain, as suggested by the pie-chart 98, shows a global mass reduction of more than 100 [kg] in comparison with the "neutral use" HEV, now decreased to a total of 1969 [kg].
This is achieved by assuring a greater part of the vehicle propulsion by thermal energy through a "light" yet more present (6 cylinders 2.8 [l]) internal combustion engine than for the two other applications considered. The battery capacity, i.e. number of cells and thus mass are reduced by 32 [%] because of the ETM power drop (also observable in the decrease of the open circuit voltage $U_{bat,0}$ [V])
Regarding other parameters, the sportive *Driver* is obviously the most agressive of the three; to the point that the limited slip differential has to help the ESP (see Figure 101).
Gear shifts are also made later than in the previous optimization results.
Finally, note that the ETM inner rotor has been decreased to the point that only a thin layer (4 [mm]) of magnetic steel is present in the rotor between the permanent magnets and the motor shaft.

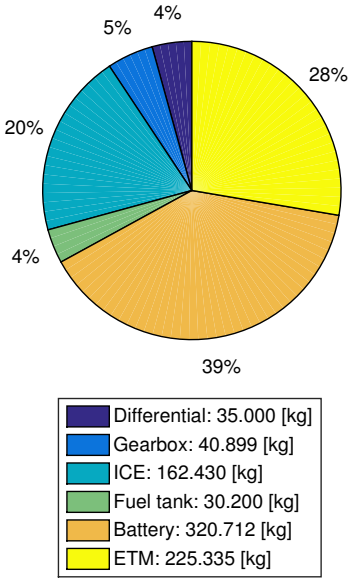

Figure 98: Repartition of the masses in the hybrid powertrain destined to a sportive use

Driver					ETM		
k_a [1/s]	k_{max} [-]	k_{secu} [-]	k_{turn} [m]	k_v [1/s]	R_{ir} [mm]	R_{os} [mm]	S_{Cu} [mm^2]
5.0	1.0	0.18	5.0	1.3	34	151	16.7
	Battery		ICE		Differential		
	$U_{bat,0}$ [V]	$Q_{bat,0}$ [kAh]	$V_{cc,tot}$ [cc]	θ_s [°]	i_{diff} [-]	t_{diff} [%]	
	240.0	8.694	2862	-15	4.5	10.0	
Gearbox							
$\omega_{t,min}$ [RPM]	$\omega_{t,max}$ [RPM]	$i_{g,1}$ [-]	$i_{g,2}$ [-]	$i_{g,3}$ [-]	$i_{g,4}$ [-]	$i_{g,5}$ [-]	$i_{g,6}$ [-]
2145	4185	3.5	2.2	1.7	1.3	1	0.8

Table 24: HEV parametrization for sportive use

6.2 Performances Study

Pure performances

Test	$v_{Max} = 227.615$ [km/h]	0-100 [km/h]	40-120 [km/h]
Time [s]	48.567	6.129	6.116
Distance [m]	2.407	92.109	145.95

Table 25: Pure performances test results

Intuition would want this sportive HEV to show the best longitudinal performance. But as Table 25 confirms, highest v_{Max} does not necessarily mean best lap time on the track. Also, due to slip of great amplitude at start, the 0-100 [km/h] acceleration takes more time here than for the "neutral" vehicle.

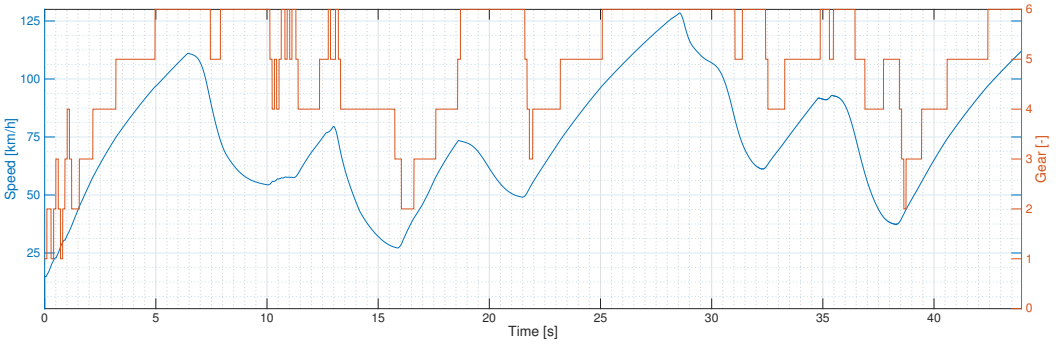

Figure 99: Sportive HEV velocity and gear selection around the test track

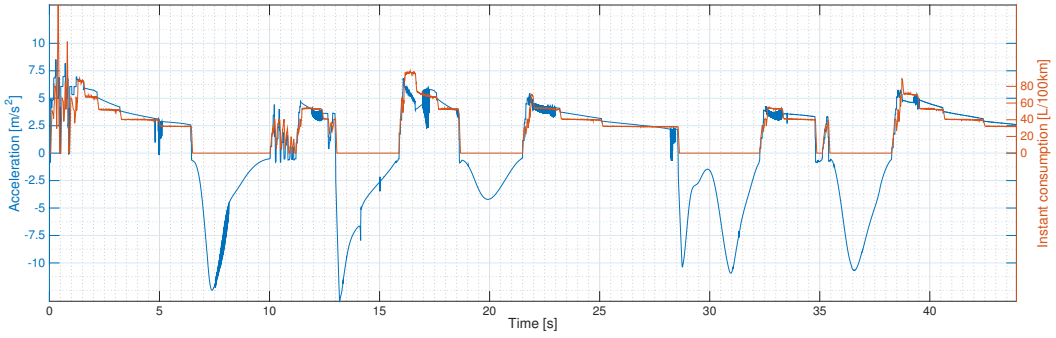

Figure 100: Sportive HEV acceleration and instantaneous fuel consumption around the test track

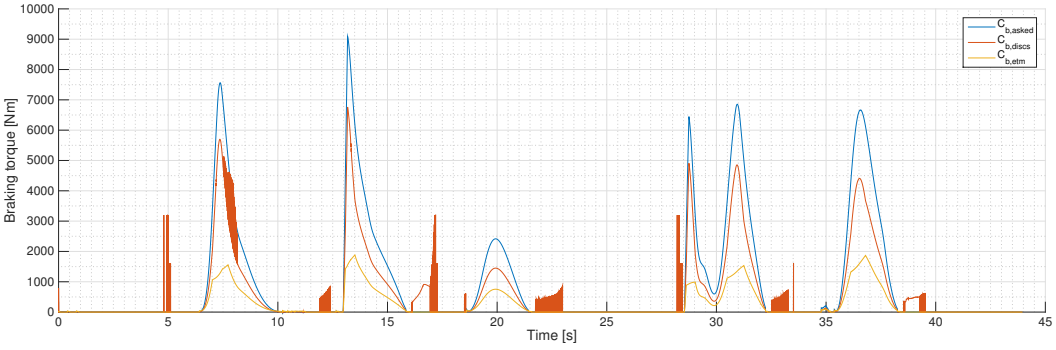

Figure 101: Sportive HEV braking points on the test track

Reference lap

The first thing noticeable in Figures 100 and 101 is the frequent triggering of the ESP to maintain the car on the track in curves, but also resulting in great amplitude variation of speed at the motor shaft, therefore creating hesitations in the gearbox controller (Figure 99). Together with a relatively slower 0-100 [km/h] acceleration, this vehicle clearly illustrates the importance of dynamic stability control for good performance on track, and a lap time of 43.936 [s].
From an energetic point of view, overall acceleration of the speed profile around the track and late braking points have significantly raised the total energy consumption, and yet not augmented the regenerative braking of such a small ETM. This indeed is now up to 12.231 [MJ] = 3.398 [kWh] $\stackrel{eq}{=}$ 0.406 [l] of gasoline for a mean fuel and net electrical consumption of:

Fuel consumption	Electrical discharge
27.44 [l/100km]	1.206 [kWh/km]

Table 26: Mean energy uses around the test track

This can appear quite high. But remember that the traditional numbers of fuel consumption are evaluated on non-realistic driving cycles and for engines far more advanced technologically than the one chosen for the purpose of this work. Finally, the vehicle has here been put to the test of minimizing a lap time around a reference track which is certainly not comparable to everyday use.

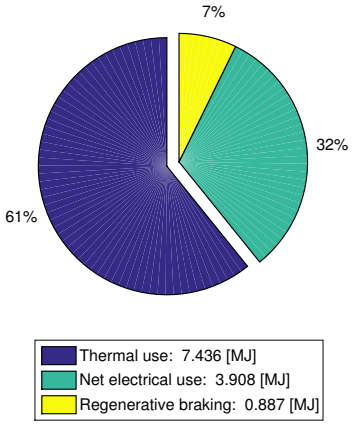

Figure 102: Repartition of the energy used to overcome one lap around the test track

Operating points

Finally, the best representation of this competition-oriented HEV is perhaps the powertrain operating points in Figures 103 and 104. The ICE is notably operated at higher speeds with less regards to the BSFC compared to the weight attributed to back-up torque for sudden acceleration. Still, full throttle maintains it in high efficiency region.
The same phenomenon is observable for the ETM where the range of operation has been extended towards higher rotation speed meaning the motor (and generator) is more often used in the maximal power region (or flux-weakening) than in neutral or economical use.

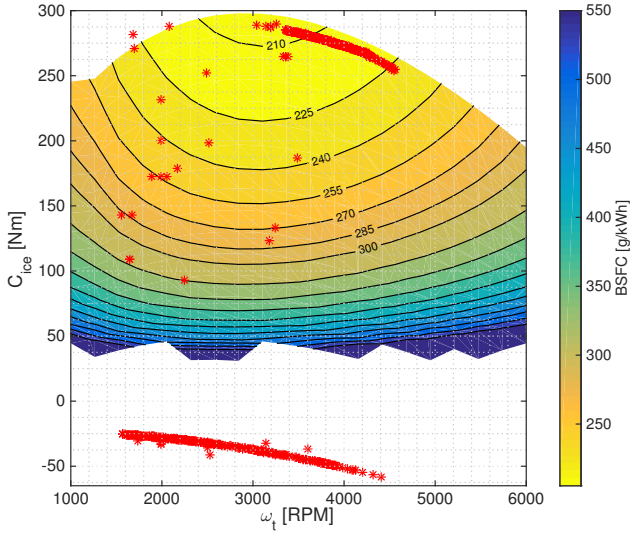

Figure 103: ICE BSFC with operating points around the track

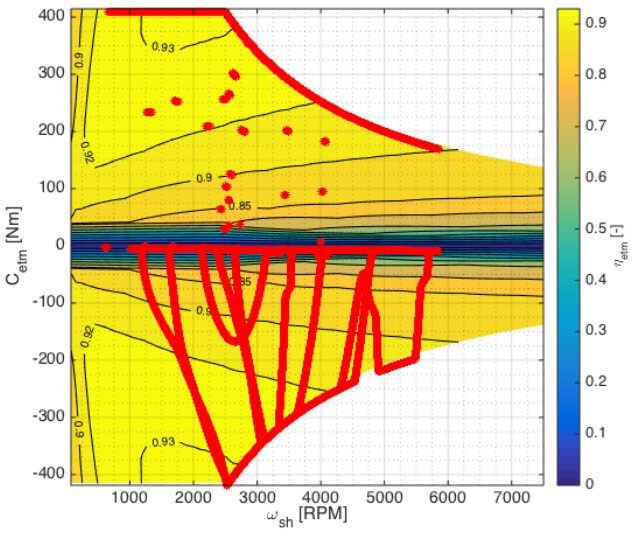

Figure 104: ETM efficiency map with operating points around the track

7 Critical Conclusions

Throughout this third part, the build HEV simulator has been put to the test and vehicles were optimized for certain precise applications. It is now time to step back an take conclusions of all those results.

More than being quite difficult to optimize because of the non convex tendency of the model and its great number of parameters, the results also suggest that a global optimum between all possible HEV application is near non-existent. Indeed, it could be observed that a constant trade-off was necessary between energy use and performance on the track.

Mass-to-power ratio

Moreover, todays technologies regarding electrical energy use makes HEV with a great deal of electrical embedded power very heavy.
As an illustration, results of the optimization processes lead in this part regarding thermal and electrical path masses are shown in Figure 105 while Figure 106 show the mass-to-power ratios of the studied vehicles.

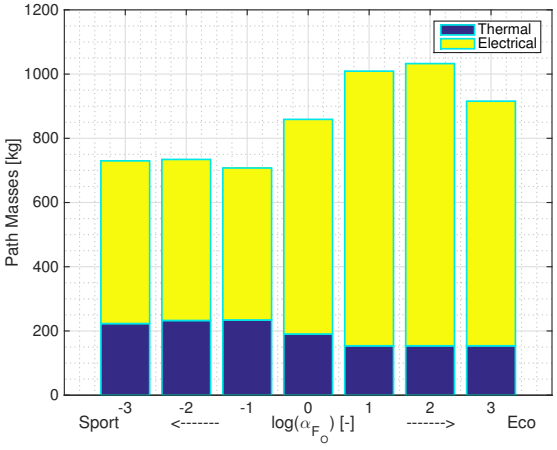

Figure 105: Path masses versus the car use

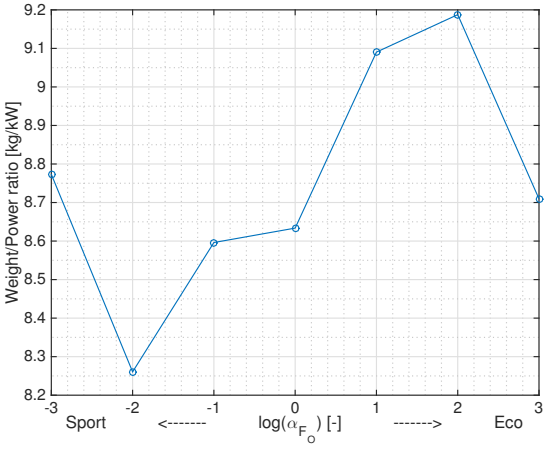

Figure 106: Mass-to-power ratio versus the car use

Except for two outliers that were already identified at the extremes of the plots, the tendency seems linear. A link can thus logically be assumed between mass-to-power ratio and vehicle performance (in terms of lap time or fuel economy).

Embedded power

Another remarkable results of that study is that, for a very basic hybrid electric vehicle (as the one modeled for the purpose of this work), power does not necessarily mean performance. Indeed, as the enlightened reader would have had noticed, and as Figure 107 better exposed, for all the very diverse applications studied, sort of regardless of the objective function bias, the global powertrain output is always nearly the same.

In fact, when crossing those results with the illustrations 105 and 106, it becomes quite clear that the same power is not at all administrated for the same uses. Indeed, for an "economical" application, the powertrain has the sole goal of propelling the car, moving its own (quite heavy due to large batteries) mass. As for a "sportive" HEV, less regards to the energy consumption has translated into a more lightweight vehicle, relying more on traditional fuel propulsion. In that case, power is allocated to pure performances rather than slow, but more economical, movement.

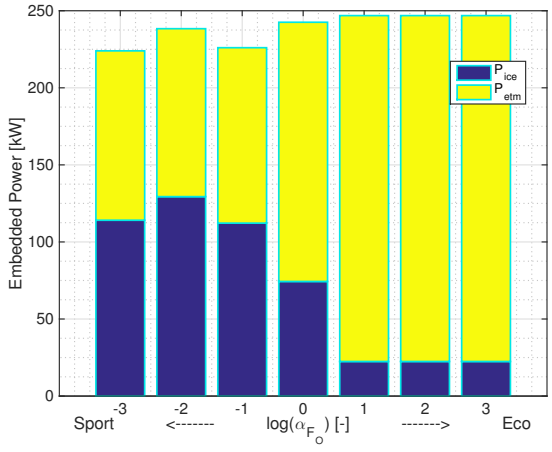

Figure 107: Embedded powers for the simulated HEV

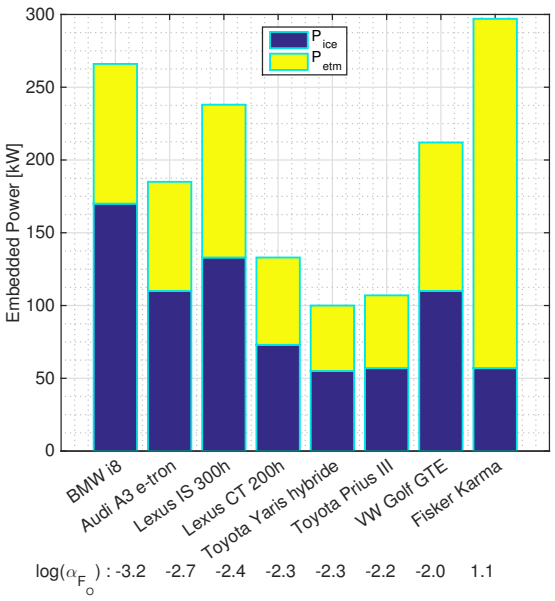

Figure 108: Embedded powers for existing cars

Comparison with the industry

Another interesting conclusion to draw from this research session is to compare the supposed optimal vehicle found to the general trend on the HEV market.
Ordered by their approximative objective bias are some real-life vehicles shown in Figure 108. What is funny to realize is that, except for the Fisker Karma, all those vehicles are considered as sportive in the definition of this work's objective, even small passenger's cars like the Toyota Yaris.
It might appear quite hard for students used to more theoretical university research to justify that trend but one must not be naive: if car manufacturers shift in what seems at first to be a more electrical way, it is precisely because it is trendy.
It was exposed in section how inappropriate are the current methods for fuel consumption evaluation, and this year's Volkswagen AG scandal just reinforced what could be a general conclusion regarding the market: if car manufacturers are making hybrid vehicle right now, it is not with the objective of reducing their car's energetic impact, it is because it gives them a good image.

General Conclusion

An underlying objective of this master thesis was to understand, critic and eventually expose best practice rules as to how conceive an hybrid electric vehicle.

The idea was at first to consider the vehicle in its entirety, bringing light to the importance of every aspect that makes a car more performant than another.
For this, a rather complete HEV simulator has been designed in C language for implementation in the *Robotran*© multibody simulation environment. Each of the sub-systems judged relevant after a consequent literature review, has been fully parametrized, highlighting key parameters for further use. For those who needed it, a dedicated controller has also been implemented, with focus on actual feasibility with existant technologies, rather than considering that, as in simulation, everything is perfectly measurable and reliable.
At first, the simulator showed promising results, in agreement with common intuitions and what was available in the scientific litterature.
The second phase of the job was to elaborate a representative strategy for vehicle performances evaluation and, hopefully, optimization. For this, rather than following a common use that has already shown its weakness, it was decided to go for an optimization of the dynamic (also in curves) performances of the car on a reference track. Of course, this demanded considerable computational resources and restriction had to be made regarding the time-simulation duration and a subset of parameters was elected for the first optimization processes. Concerning the methodology adopted, it had the advantage of a disposable and ready-to-use optimizer, perfectly suited for track and application-oriented optimizations. For that, the authors would like again to thank Aubain Verlé for its continuous support along the year.

Finally, the first optimized results were beginning to fall. A total of 7 vehicles were optimized on 6 key parameters for a same virtual driver; and 3 were further studied, in multiple iterations, extending the number of optimization parameters to 22.
And following those first results, conclusions could be drawn with perhaps the most impressive one being the importance of the electric path in the optimized hybrid powertrain. Indeed, for the vehicles tested, only one had > 50 [%] of thermal embedded power. When one knows that the hybridization trend in the car industry looks more like electrical auxiliaries, this is a bit odd. Of course, it has to be reminded that this is a work of pure simulation with hard assumptions and neglecting an infinite number of external parameters, but this was its first conclusion.
The second being that one cannot ignore the link between the vehicle's mass and its dynamic performances. This relation exposes perhaps the principal enemy for today's hybrid vehicles in sportive applications. Indeed, even if it seems to become mandatory in nearly every motorsport discipline, it has to be noted that electric storage hybridization for fuel economy always makes a trade-off against pure performances: and this trade-off is mass.

What is more, the importance to detail in the design of a car were noticed such as in the gearbox control, the differential reduction ratio and all parameters were outputted their physical value.
It was also observed the weight of the driver's skills and of electronic stability programs, but these may fall into another study more concerned by good advice for sportive driving than hybrid powertrain optimization.

Part IV

Appendices

A Electric Traction Motor

A.1 $dq0$ Transformation

Before entering in the details of the ETM model, it is necessary to familiarize the reader with the $dq0$ or direct-quadrature-zero transformation. This mathematical tool is particularly important for vector control of electric machines like a tri-phase PMSM drive for instance, as it no longer places the electric quantities in the tri-phase source (1;2;3) frame but directly in the 2-dimensional (direct d and quadrature q) frame of the motor in rotation.
The power-invariant matrix for the frame transformation is given by equation (127):

$$\underline{X_{dq0}} = \begin{pmatrix} X_d \\ X_q \\ X_0 \end{pmatrix} = \underline{P}(\theta) \cdot \underline{X_{123}} = \sqrt{\frac{2}{3}} \begin{pmatrix} \cos(\theta) & \cos(\theta - \frac{2\pi}{3}) & \cos(\theta + \frac{2\pi}{3}) \\ -\sin(\theta) & -\sin(\theta - \frac{2\pi}{3}) & -\sin(\theta + \frac{2\pi}{3}) \\ \frac{\sqrt{2}}{2} & \frac{\sqrt{2}}{2} & \frac{\sqrt{2}}{2} \end{pmatrix} \cdot \begin{pmatrix} X_1 \\ X_2 \\ X_3 \end{pmatrix} \tag{127}$$

And the inverse transformation 128 to recover tri-phase values from the $dq0$ ones:

$$\underline{X_{123}} = \begin{pmatrix} X_1 \\ X_2 \\ X_3 \end{pmatrix} = \underline{P^{-1}}(\theta) \cdot \underline{X_{dq0}} = \sqrt{\frac{2}{3}} \begin{pmatrix} \cos(\theta) & -\sin(\theta) & \frac{\sqrt{2}}{2} \\ \cos(\theta - \frac{2\pi}{3}) & -\sin(\theta - \frac{2\pi}{3}) & \frac{\sqrt{2}}{2} \\ \cos(\theta + \frac{2\pi}{3}) & -\sin(\theta + \frac{2\pi}{3}) & \frac{\sqrt{2}}{2} \end{pmatrix} \cdot \begin{pmatrix} X_d \\ X_q \\ X_0 \end{pmatrix} \tag{128}$$

The zero component of $\underline{X_{dq0}}$ being less important for the purpose of this study.

A.2 Motor Design

Stator windings

There are multiple design parameters that influence the performances of the PMSM. The stator windings' resistance is important to take into account as it is well known that metallic wires have the tendency to heat when conducting an electric current (of particularly high value for automotive power applications). If the small (recall that modulation is supposed to be perfect without introducing any noise) frequency effect (sum of the skin and proximity effects) is neglected, Z_s [Ω] only rises with the temperature of the windings T_w [°C] [14]:

$$Z_s(T_w) = \frac{\sigma_{Cu}(T_w)\, n_c\, l_{Cu}}{S_{Cu}} \tag{129}$$

Where S_{Cu} [m^2] is the wire's section whose minimum value is limited by the current that it is supposed to conduct (see appendix A.3 about *Thermal Modeling*). σ_{Cu} [$\Omega \cdot$ m][10] gives the copper resistivity and l_{Cu} [m] is the length of one turn in the coils:

$$\sigma_{Cu} = 1.68 \cdot 10^{-8}(1 + 0.003862(T_w - 20)) \tag{130}$$

$$l_{Cu} = 2(l_r + l_c) \tag{131}$$

$$\text{where } l_c = \sqrt{2R_{ms}^2\left(1 - \cos\left(\frac{2\pi}{m_{ph}}\right)\right)} \tag{132}$$

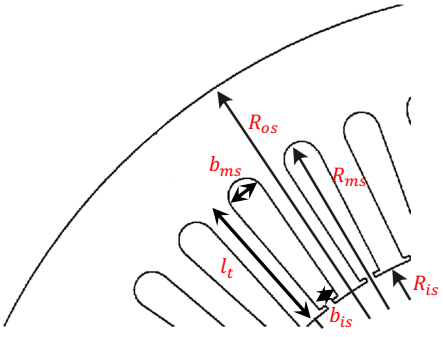

Figure 109: Stator dimensions

[10] Jocelyn PHILLIPS. Physics for Scientists and Engineers with Modern Physics (4th ed.). 1984

l_r [m] is the stator length (supposed to be the same as the rotor's), l_c [m] is the coil width approximated by the rule of cosine (Al-Kashi) for an inner stator yoke radius $R_{ms} = R_{is} + l_t$ [m]. $l_t = \frac{5}{7}(R_{os} - R_{is})$ [m] is the teeth's length arbitrarily fixed for good mechanical durability. Stator outer and inner radii R_{os} and $R_{is} = R_{or} + e_{ag}$ [m] (outer rotor radius $R_{or} = R_{ir} + e_{PM}$ [m]) stay dimensional performance parameters via the inner rotor radius R_{ir} [m] and the air-gap thickness $e_{ag} = 2$ [mm] (in order to accept relative motion due to the powertrain vibrations on the motor shaft).

For a number of slots $S = 2 \cdot 2p\ m_{ph}$ [-] (i.e. 2 slots per pole and per phase), each with the same base width b_{is} [m] as the teeth (each slot assumed to be a trapeze of larger base b_{ms} [m]), the number of turns n_c [-] in each coils constituting the stator windings can be approximated from the slots' area S_{slot} [m^2] with a slot-filling factor of 0.75:

$$n_c = \text{ floor}\left(0.75\frac{S_{slot}}{S_{Cu}}\right) \tag{133}$$

$$S_{slot} = (b_{ms} + b_{is})\frac{l_t}{2} \qquad b_{ms} = \sqrt{2R_{ms}^2(1 - \cos\left(\frac{2\pi}{2S}\right)} \qquad b_{is} = \sqrt{2R_{is}^2(1 - \cos\left(\frac{2\pi}{2S}\right)} \tag{134}$$

Various topologies have been envisaged in [6] to satisfy the conditions mentioned in Part I, section 8.1, and are exposed in Figure 110. Their performances were already observable on mappings 25 and 26.

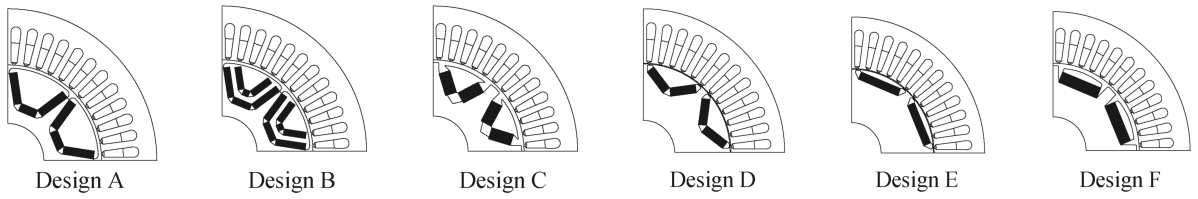

Figure 110: Topologies tested in [6]

Clearly, Design D appears as the most performant, offering better flux weakening - and thus longer range of quasi-constant power output - due to a large difference between direct and quadrature stator inductances L_d and L_q [H] respectively:

$$L_d = 0.49 \text{ [p.u.]} \tag{135}$$

$$L_q = 1.0 \text{ [p.u.]} \tag{136}$$

The "per unit" system referring here to the rated value of inductance L_{rated} [H]:

$$L_{rated} = n_c\ \mu\ A_c \tag{137}$$

In which $A_c = l_c\ l_r$ [m^2] is the surface area of one turn of coil and $\mu_0 = 4\pi \cdot 10^{-7}$ [N/A^2] the magnetic permeability of air.

Permanent Magnets

Even though it is not followed by design D, the permanent magnets disposition can be assumed to be surface mounted. This approximation eases the computation of Ampère's Law developed in equations (138), (139), (140) and (141), on a closed loop Γ, observable in Figure 111.

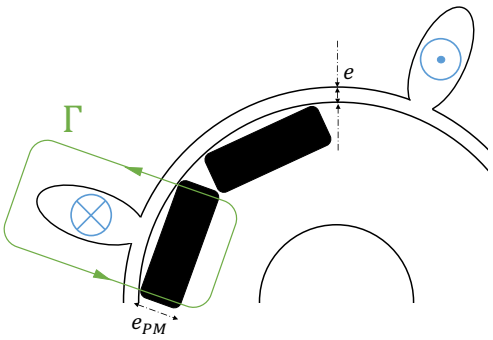

Figure 111: Ampère's Law application

$$\oint_{\Gamma} \underline{H} \cdot \underline{dl} = 2H_{ag}\, e_{ag} + 2H_{PM}\, e_{PM} = 0 \tag{138}$$

$$\text{In air, } H_e = \frac{B_{ag}}{\mu_0} \text{ and, for interface continuity, } B_{ag} = B_{PM} \tag{139}$$

$$\Leftrightarrow \frac{B_{PM}}{\mu_0}\, e + H_{PM}\, e_{PM} = 0 \tag{140}$$

$$\Leftrightarrow B_{PM}(H_{PM}) = -H_{PM}\, \frac{e_{PM}}{e_{ag}}\, \mu_0 \tag{141}$$

H_{ag} [A/m] and B_{ag} [T], H_{PM} [A/m] and B_{PM} [T] are respectively the magnetic H and B-$fields$ in the air-gap of thickness $e_{ag} = 2$ [mm], and those induced by the permanent magnets of thickness e_{PM} [m] (optimized for sufficient magnetic flux versus the total magnets' mass).
Equation (141) must then be crossed with the demagnetization curves (H_c [Am] and B_r [T] for coercitivity and remanence), characteristic of the selected permanent magnets and shown in Figure 112. N40UH are sintered Neodymium Iron Boron (NdFeB) magnets made by Eclipse Magnetics® . They present good performances for the operating temperatures of the motor.

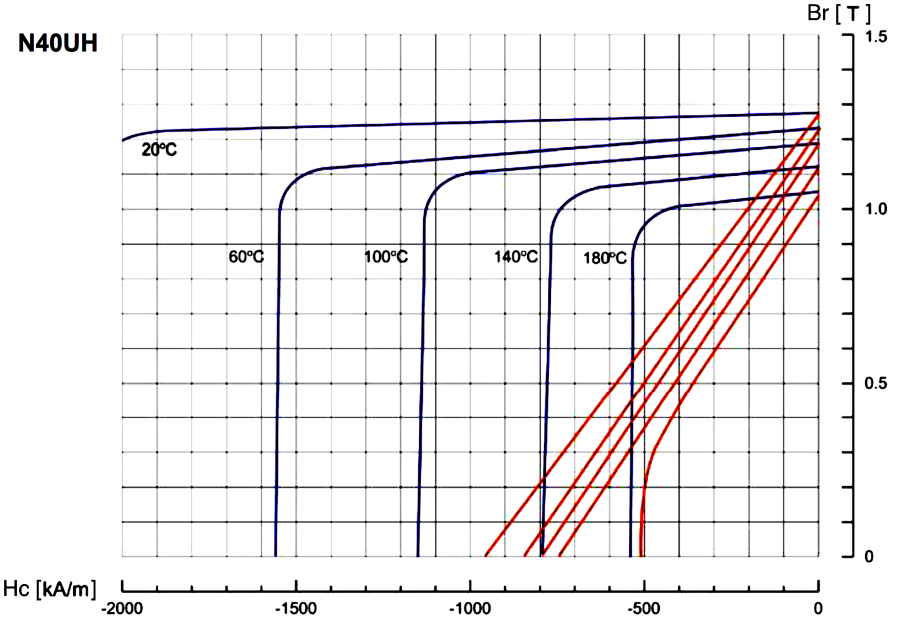

Figure 112: Demagnization curves for N40UH NdFeB permanent magnets

In simulation, those curves are fitted by two lines of slopes varying with the permanent magnets' temperature T_{PM} [°C], and with $H_c(B_r = 0\ ;\ T_{PM})$ and $B_r(H_c = 0\ ;\ T_{PM})$.
The intersection between equation (141) and those curves at the operating T_{PM} [°C] gives B_{PM} [T] and allows computation of the air-gap flux ϕ_{PM} [Wb] due to the permanent magnets:

$$\phi_{PM} = \frac{B_{PM}\, S_{PM}}{\lambda_0} \qquad \text{with} \qquad S_{PM} = \frac{2\pi(R_{is} - e_{PM})}{2p}\, l_r \tag{142}$$

Where the leakage coefficient $\lambda_0 = 1.3$ [-] was found experimentally for motors comparable to design D and S_{PM} [m^2] gives one magnet's operating surface.

A.3 Thermal Modeling

The thermal model presented in this section applies the methodology introduced in [17]. The necessity of such a model should be clear by now as it was mentioned that the performances of the motor depends at least of the temperatures in the windings T_w [°C] and in the magnets T_{PM} [°C].
The principle is to take advantage of the analogy that can be made between thermal and electrical behaviour and to build a thermal equivalent circuit of the PMSM where:

Electrical Circuit			Thermal Circuit		
Voltage	U	[V]	Temperature	T	[°C]
Current	I	[A]	Heat loss	Q	[W]
Electrical resistance	Z	[Ω]	Thermal resistance	Z	[°C/W]
Electrical conductivity	$1/\sigma$	[S/m]	Thermal conductivity	κ	[W/(°C · m]

Table 27: Electrical vs Thermal quantities comparison

The circuit used is shown on Figure 113.

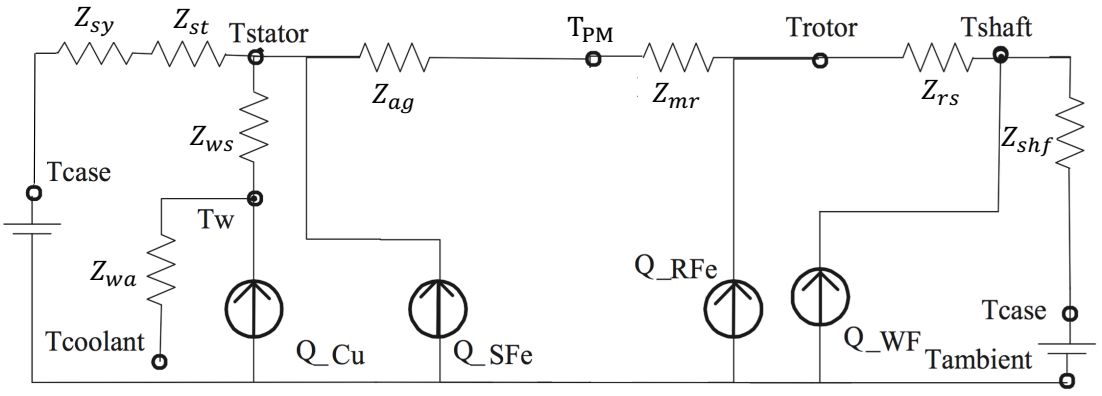

Figure 113: PMSM thermal equivalent circuit

Thermal Circuit Resolution

Assuming that thermal losses and resistances are correctly evaluated (see next subsections), the resolution of the thermal equivalent circuit proposed on Figure 27 gives the temperatures in the systems according to:

$$\frac{T_w - T_{stator}}{Z_{ws}} + \frac{T_w - T_{coolant}}{Z_{wa}} = Q_{Cu} \tag{143}$$

$$\frac{T_{stator} - T_{case}}{Z_{sy} + Z_{st}} + \frac{T_{stator} - T_w}{Z_{ws}} + \frac{T_{stator} - T_{PM}}{Z_{ag}} = Q_{S,Fe} \tag{144}$$

$$\frac{T_{PM} - T_{stator}}{Z_{ag}} + \frac{T_{PM} - T_{rotor}}{Z_{mr}} = Q_{R,Fe} \tag{145}$$

$$\frac{T_{rotor} - T_{PM}}{Z_{wr}} + \frac{T_{rotor} - T_{shaft}}{Z_{rs}} = 0 \tag{146}$$

$$\frac{T_{shaft} - T_{rotor}}{Z_{rs}} + \frac{T_{shaft} - T_{case}}{Z_{shf}} = Q_{WF} \tag{147}$$

By default, the case and coolant (air) temperatures will be the ambient one, approximately 27 [°C].
It also has to be noted that Eddy currents losses. Indeed, even though they can deteriorate the magnets on the long-term use, they do not increase their temperature much and are therefore not taken into account in this study.

Note also that this thermal model is computed in discrete time, and does not introduce any thermal inertia. Temperatures are simply computed following the actual thermal losses.

Thermal Losses

The **copper or Joule losses** Q_{Cu} [W] are simply computed following the current intensity $I_s = \sqrt{I_d^2 + I_q^2}$ [A] flowing in the stator windings:

$$Q_{Cu} = m_{ph}\ Z_s\ I_s^2 \tag{148}$$

In [14], the authors compute the **magnetic or iron losses** $Q_{S,Fe}$ [W] **in the stator**, using multiple experimental data depending on the selected electrical steel:

$$Q_{S,Fe} = m_{S,Fe}\ K_{Fe}\ f_s^{\varphi}\ B_{PM}^{\varepsilon} \tag{149}$$

$$\text{With} \qquad m_{S,Fe} = \rho_{Fe}\ V_{S,Fe} \qquad V_{S,Fe} = \pi(R_{os}^2 - R_{is}^2)l_r - V_{Cu} \qquad V_{Cu} = 2n_c(l_c + l_r)S_{Cu}\ \frac{S}{2} \tag{150}$$

Where V_{Cu} [m^3] is the total volume of copper wires constituting the coils, $m_{S,Fe}$ [kg] equals the total mass of iron (or electrical steel) used in the stator, ρ_{Fe} [kg/m^3] its density and $V_{S,Fe}$ [m^3] its total volume. For M400-50A Steel[11]:

$$K_{Fe} = 3.8 \cdot 10^{-3}\ \text{[J/T]} \qquad \varphi = 1.54\ \text{[-]} \qquad \varepsilon = 1.84\ \text{[-]} \qquad \rho_{Fe} = 7700\ \text{[kg/m}^3\text{]} \tag{151}$$

The **iron losses in the rotor** $Q_{R,Fe}$ [W] are computed in the exact same way as (149), except the volume of iron in the rotor is $V_{R,Fe} = \pi(R_{ir}^2 - R_{sh}^2)l_r$ [m^3] (where the motor shaft radius $R_{sh} = 3.0$ [cm]).

Finally, the **mechanical losses, i.e. the sum of windage and friction (+ ventilator) losses** Q_{WF} [W], according to [6] and [30] before them, can be evaluated as:

$$Q_{WF} = 2k_\rho\ R_{or}(l_r + 0.6\tau_p)v_r \tag{152}$$

$k_\rho = 10$ [(W $\cdot$ s^2)/m^4] is an experimental factor for small- and medium-sized machines. $\tau_p = \frac{2\pi}{2p}$ [rad] gives the pole pitch, and $v_r = \omega_{sh}\ R_{or}$ [m/s] is the surface speed of the rotor.

Thermal Resistances [17]

It is important to note that for this simplified thermal model, radiation is neglected due to its minor effect on the system's behaviour.
As these thermal resistances essentially depend on dimensional parameters, the rotor structure is illustrated in Figure 114.

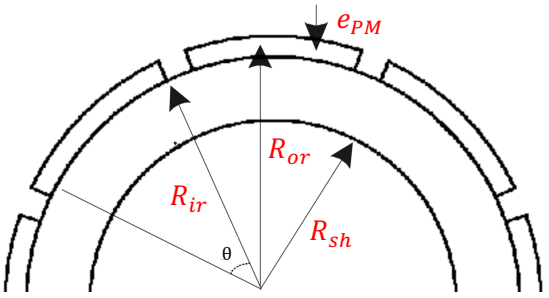

Figure 114: Rotor dimensions

For air-cooled machines, computation of the **air-gap convection thermal resistance** Z_{ag} [°C/W] requests monitoring of fluid mechanics effects:

[11] Cogent Power Ltd., Electrical Steel. Non Oriented. Fully Processed., datasheet

$$Z_{ag} = \frac{e_{ag}}{Nu\ \kappa_{air}\ A_{ag}} \quad \text{with} \begin{cases} Nu = 2 & \text{if } Ta \leq 41 \\ Nu = 0.212 Ta^{0.63} Pr^{0.27} & \text{if } 41 < Ta \leq 100 \\ Nu = 0.386 Ta^{0.5} Pr^{0.27} & \text{if } Ta > 100 \end{cases} \tag{153}$$

Where A_{ag} [m^2] is the air-gap cylindrical surface. Nu [-] is the Nusselt number of the air flow in the air gap, $Ta = \frac{4\omega_{sh}^2 R_{or}^4}{\nu_{air}}$ [-] and $Pr = \frac{\nu_{air}}{\alpha_{air}}$ [-] (α_{air} [m^2/s] the thermal diffusivity of air) its Taylor and Prandtl numbers respectively. The motionless thermal conductivity of air κ_{air} [W/(°C $\cdot$ m)], its kinematic viscosity ν_{air} [m^2/s] and its Pr [-] have been fitted on an engineering toolbox' data[12], varying with the air-gap temperature.

The **radial conduction thermal resistance of the rotor core** Z_{rs} [°C/W] is dimensionally computed as:

$$Z_{rs} = \frac{\ln(R_{ir}/R_{sh})}{2\pi\kappa_{rotor} l_r} \tag{154}$$

With a thermal conductivity of the rotor core $\kappa_{rotor} = 30$ [W/(°C $\cdot$ m)].

Concerning the **radial conduction thermal resistance of the poles** Z_{mr} [°C/W]:

$$Z_{mr} = \frac{\ln(R_{or}/R_{ir})}{2\pi\kappa_{PM} l_r} \tag{155}$$

The thermal conductivity of the magnets $\kappa_{PM} = 8.95$ [W/(°C $\cdot$ m)].

Neglecting the heat transfer from air to the shaft, the only contacts of the shaft are with the bearings and the rotor. The **thermal resistance of the shaft** Z_{shf} [degree C/W] is then evaluated as:

$$Z_{shf} = \frac{R_{sh,a} + R_{sh,b}}{2} \quad \text{where} \begin{cases} R_{sh,a} = \frac{1}{2\pi\kappa_{shf} l_r} + \frac{L_{bs}}{2\pi\kappa_{shf} R_{sh}^2} \\ R_{sh,b} = \frac{1}{4\pi\kappa_{shf} l_b} + \frac{L_{bs}}{2\pi\kappa_{shf} R_{sh}^2} \end{cases} \tag{156}$$

The motor shaft being made of highly martensitic steel for resistance to torsion efforts, its thermal conductivity $\kappa_{shf} = 30$ [W/(°C $\cdot$ m)][13]. The bearings, them have a thickness $l_b = 40$ [mm] and the distance between them and the centre of the rotor mean $L_{bs} = \frac{l_r + l_b}{2}$ [m].

The radial conduction thermal resistance of stator teeth Z_{st} [°C/W] is estimated as:

$$Z_{st} = \frac{\ln(R_{ms}/R_{is})}{2\pi\kappa_{Fe} l_r V_{F_e}/(V_{Fe} + V_{Cu})} \tag{157}$$

With thermal conductivity of the stator teeth (made in M400-50A steel) $\kappa_{Fe} = 28$ [W/(°C $\cdot$ m)].

The **stator yoke** being made of the same material, its **radial conduction thermal resistance** Z_{sy} [°C/W] is:

$$Z_{st} = \frac{\ln(R_{os}/R_{ms})}{2\pi\ \kappa_{Fe}\ l_r} \tag{158}$$

The slot-filling ratio being of 75 [%], the **conduction thermal resistance between windings and stator** Z_{ws} [°C/W] is evaluated as:

$$Z_{ws} = \frac{0.25 S_{slot}}{L_{slot} l_r \kappa_{Cu,Fe}} \qquad \text{with } L_{slot} = b_{is} + b_{ms} + 2\sqrt{\left(\frac{b_{is} + b_{ms}}{2}\right)^2 + l_t^2} \tag{159}$$

$\kappa_{Cu,Fe} = 0.408$ [W/(°C $\cdot$ m)] is the equivalent conductivity coefficient of the air and insulation material in stator slot, evaluated by simulation; while L_{slot} [m] is the stator slot section perimeter.

[12] The Engineering Toolbox, http://www.engineeringtoolbox.com/dry-air-properties-d_973.html, last checked 5/05/2016

[13] Dew-Stahl catalog, https://www.dew-stahl.com/fileadmin/files/dew-stahl.com/documents/Publikationen/Broschueren/015_DEW_RSH_GB.pdf

Finally, the loops constituting the windings must be a bit longer (this excess is taken as the same width of the bearings l_b [m]) than the stator to close. In such a disposition, they exchange some heat with adjoining air. The **convective thermal resistance between winding external to the stator and adjoining air** Z_{wa} [°C/W] can be computed as:

$$Z_{wa} = \frac{1}{h_{wa} S_{wa}} \quad \text{where} \begin{cases} h_{wa} = 15.5(0.29 v_{in} + 1) \\ S_{wa} = 2\pi R_{is}\ 2 l_b \end{cases} \tag{160}$$

h_{wa} [W/(°C $\cdot$ m^2] is the convection coefficient between the end winding of the stator and adjoining air and S_{wa} [m^2] the total surface of the winding external to stator. $v_{in} = 7.5$ [m/s] is the inner air speed for a fan with an efficiency of 50 [%].

B Internal Combustion Engine

Most of the modeling process described in this chapter is directly taken from the works of Pr. Hervé Jeanmart [20] (UCL) and Pr. Lino Guzzella [21] (ETH).

B.1 Engine Breathing

Volumetric efficiency

To present an internal combustion engine in its simplest way, one can describe it as a volumetric machine, swallowing gas and air in order to produce a useable work. This work obviously depends on the quantity of air that penetrates in a cylinder. To quantify the filling of the cylinder, the volumetric efficiency r [-] is defined as the ratio between the mass of air-fuel mixture m_{mix} [kg] and the maximum mass admissible in the cylinder if it was at normal conditions of pressure and temperature:

$$r = \frac{m_{mix}}{\rho_0 V_{cc}} \tag{161}$$

ρ_0 [kg/m^3] is thus the air density in normal conditions, and V_{cc} [m^3] the capacity of one cylinder.

$$T_0 = 298.15 \text{ [K]} \qquad p_0 = 101325 \text{ [Pa]} \qquad \rho_0 = \frac{p_0}{R_{air} T_0} = 1.1837 \text{ [kg/m}^3\text{]} \tag{162}$$

$$V_{cc} = \pi \left(\frac{B}{2}\right)^2 C \text{ [m}^3\text{]} \tag{163}$$

With $R_{air} = 287.1$ [J/(kg $\cdot$ K] the specific air constant, B [m] is one cylinder's bore and C [m] the stroke. Hybridization having also the objective of engine downsizing, C/B ratio is chosen at 0.8, which assures a slightly short stroke in order to, hopefully, achieve higher power density and engine speed.

So how does the quantity m_{mix} [kg] penetrates in those cylinders? This is what is called "engine breathing". Pressure p_{in} [Pa] in the intake manifold is controlled by the "*Driver*'s foot" via the throttle "butterfly" valve. Overpressure with air velocity in the manifold (according to the vehicle speed) not being taken into account; maximum p_{in} [Pa] is atmospheric p_0 [Pa] at full throttle ($k_t = 1$ [-]). As [31] suggested and also confirmed by tested "admission laws", a certain amount of inlet pressure is necessary at zero load ($k_t = 0$ [-]) in order to inject a sufficient quantity of fuel to vanquish part of the losses for a reasonable engine brake and stable idle. An acceptable admission law is given by equation (164) and can be adapted following the engine's dimensions:

$$p_{in} = (0.2 + 0.8 k_t)\,(p_0 - \Delta p_{in}) \tag{164}$$

Where $\Delta p_{in} = 1325$ [Pa] gives the amount of load losses in the intake manifold. From that point, fluid mechanics gives formula (165) to compute the mass flow $\dot{m}_{i-o}$ [kg/s] of a matter between states i and o on both sides of a nozzle throat (here, the inlet and exhaust valve sections):

$$\dot{m}_{i-o} = \rho_i c_i A^* \sqrt{\frac{2}{\gamma - 1}\left(\left(\frac{p_{nt}}{p_i}\right)^{2/\gamma} - \left(\frac{p_{nt}}{p_i}\right)^{(\gamma-1)/\gamma}\right)} \tag{165}$$

Where $\rho_i = \frac{p_i}{R_i T_i}$ [kg/m^3] is the density and $c_i = \sqrt{\gamma R T_i}$ [J/(kg $\cdot$ K)] ($R = 8.3145$ [J/(mol $\cdot$ K)] the universal ideal gas constant) the speed of sound in upstream conditions i.

Two different fluid are supposed to flow into and out of the cylinder: fuel-air mixture and combustion residual smokes. Both are supposed to behave as ideal gas and so to respect (166)

$$\gamma_i = \frac{c_{p,i}}{c_{v,i}} \qquad c_{v,i} = c_{p,i} - R_i \qquad R_i = \frac{R}{M_{m,i}} \tag{166}$$

R_i [J/(kg $\cdot$ K)] is the ideal gas constant for gas i ($i \in \{a, f\}$ for air-fuel mixture and smokes), $M_{m,i}$ [kg/mol] its molar mass and $c_{v,i}$, $c_{p,i}$ [J/(kg $\cdot$ K)] its specific heat capacity at constant volume or constant pressure respectively.

Air-fuel Mixture Properties

The heat capacity ratio$\gamma_a = 1.3$ [-] (instead of 1.4 for air in order to take into account the combustible presence in the mix), and is supposed constant in ideal gas conditions, .

$$c_{p,a} = 1244.1 \text{ [J/(kg} \cdot \text{K)]} \qquad c_{v,a} = 957 \text{ [J/(kg} \cdot \text{K)]} \qquad R_a = 287.1 \text{ [J/(kg} \cdot \text{K]} \tag{167}$$

are supposed constant for the operating temperature spectrum.

Smokes Properties

Concerning the smokes, their properties are evaluated according to the equation of combustion [32].

$$M_{m,f} = \frac{(1-\vartheta)M_{m,CO_2} + \vartheta\ M_{m,CO} + \vartheta\frac{y}{4}M_{m,H_2} + (1-\frac{\vartheta}{2})\frac{y}{2}M_{m,H_2O} + ((\frac{1}{\phi}-1)z + \frac{\vartheta}{2}(1+\frac{y}{4}))M_{m,O_2} + 3.76\frac{1}{\phi}z\ M_{m,N_2}}{(1-\vartheta) + \vartheta + \vartheta\frac{y}{4} + (1-\frac{\vartheta}{2})\frac{y}{2} + (\frac{1}{\phi}-1)z + \frac{\vartheta}{2}(1+\frac{y}{4}) + 3.76\frac{1}{\phi}z} \tag{168}$$

Where $z = 1 + \frac{y-2x}{4}$ to clarify the equation. The fuel type being gasoline assimilated to $CH_{1.8}$, $x = 0$ [-] and $y = 1.8$ [-].
But as the combustion is here supposed to be complete, no unburnt products of pyrolysis are present so that $\vartheta = 0$ [-]. Moreover, the air-fuel mixing system, such as a carburetor for instance, is supposed to achieve stoichiometric mix at all engine's load and speed, i.e. fuel richness $\phi = 1$ [-] (the only parameter for exhaust gas composition in this model). Those simplifications for the calculation of specific heat capacity gives:

$$c_{p,f} = \frac{M_{m,CO_2}c_{p,CO_2} + \frac{y}{2}M_{m,H_2O}c_{p,H_2O} + 3.76z\ M_{m,N_2}c_{p,N_2}}{M_{m,CO_2} + \frac{y}{2}M_{m,H_2O} + 3.76z\ M_{m,N_2}} \tag{169}$$

Noting those simplifications, only burnt products CO_2, H_2O and N_2 properties are needed:

M_{m,CO_2}	=	44	M_{m,H_2O}	=	18	M_{m,N_2}	=	28	[kg/kmol]
c_{p,CO_2}	=	1072.7	c_{p,H_2O}	=	2048.1	c_{p,N_2}	=	1089.6	[J/kg]

Table 28: Burnt products of combustion properties

Valve Breathing

p_{nt} [Pa] in (165) is the pressure at the nozzle throat and $A^*_{nt} = c_d A_{nt}$ [m^2] ($c_d = 0.6$ [-] a discharge coefficient) where A_{nt} [m^2] is its cross section area.

Obviously, this surface changes with time as the inlet and exhaust valves open and close alternatively and never instantly. The process of lifting a valve and resulting cross section is described as follows:

1. When the lift l is small, the minimal section is situated at the valve seat:

$$\text{if } l < \frac{w}{\sin(\varsigma)\cos(\varsigma)}, \qquad A_{nt} = \pi l \cos(\varsigma)\left(D_v - 2w + \frac{l}{2}\sin(2\varsigma)\right) \tag{170}$$

2. When the lift l increases, gas circulates through to the lateral section of a cylinder between the valve and its seat:

$$\text{if } l < w\tan(\varsigma) + \sqrt{\left(\frac{D_p^2 - D_s^2}{4D_m}\right)^2 - w^2}, \qquad A_{nt} = \pi D_m \sqrt{(l - w\tan(\varsigma))^2 + w^2} \tag{171}$$

3. When the lift reaches its highest values, the flow section is naturally the surface between valve port and stem:

$$\text{if } l \geq w\tan(\varsigma) + \sqrt{\left(\frac{D_p^2 - D_s^2}{4D_m}\right)^2 - w^2}, \qquad A_{nt} = \frac{\pi}{4}(D_p^2 - D_s^2) \tag{172}$$

Figure 115 permits better visualisation of the typical geometric parameters for the valves reunited in Table 29 (4-valves systems).

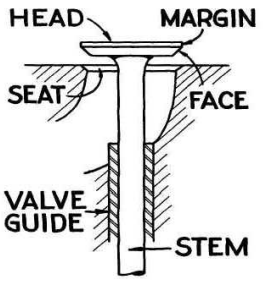

Figure 115: Valve schematics[14]

Inlet valve head diameter	[m]	$D_{v,i}$	$0.36B$
Inlet valve head diameter	[m]	$D_{v,e}$	$0.3B$
Valve seat diameter	[m]	D	$D_v/1.1$
Valve port diameter	[m]	D_p	$\approx D$
Valve stem diameter	[m]	D_s	$0.22D$
Seat angle	[°]	ς	30
Maximum lift	[m]	l_{max}	$0.12B$
Seat width	[m]	w	$0.05D/\cos(\varsigma)$
Mean seat diameter	[m]	D_m	$D_v - w$

Table 29: Typical geometric valve parameters

Inlet valves being larger as an engineering trick for better volumetric efficiency.
What remains to evaluate A_{nt}^* [m^2] is a so-called valve lift law for l depending of the cams' shape. It will be simplified here as a sinusoidal function:

$$l_j = \sin\left(\pi\frac{\theta - \theta_{j,o}}{\theta_{j,c} - \theta_{j,o}}\right) \tag{173}$$

Where θ [°] is a crank angle, $\theta_{j,o}$ and $\theta_{j,c}$ describing the opening and closing timing of the valve j ($j \in \{i, e\}$ for inlet and exhaust) in question.
A complete cycle being on 2 rounds of the crankshaft, the usual convention establishes that (cfr. Figure 116):

1. Admission is made between 360°-540°, i.e. $\theta_{i,o} \in [360°; \theta_{i,c}]$ and $\theta_{i,c} \in [\theta_{i,o}; 540°]$
2. Then comes the strokes of compression [540°;0°]
3. And expansion [0°;180°] (see next section)
4. Finally the exhaust between 180°-360°, i.e. $\theta_{e,o} \in [180°; \theta_{e,c}]$ and $\theta_{e,c} \in [\theta_{e,o}; 360°]$

Valve overlapping, i.e. exiting the hereby defined boundaries, being sometimes beneficial, the choice for timing values $\theta_{j,k}$ ($k \in \{o, c\}$) is let to an optimization process. Indeed, it is well known, for instance, that delaying admission closure $\theta_{i,c}$ [°] at the beginning of the compression stroke can increase volumetric efficiency r [-] at higher engine speed, taking advantage of the load losses in the intake manifold Δp_{in} [Pa] (see [20]).

Cylinder Mix

During the breathing phases (i.e. admission and exhaust), the mass m_c [kg] of gas inside the cylinder evolves as:

$$\frac{dm_c}{dt} = \dot{m}_{f,i} - \dot{m}_{r,i} + \dot{m}_{r,e} - \dot{m}_{f,e} \tag{174}$$

Mass of which a quantity $f_c(t) = m_f/m_c$ constitutes residual smoke.

$$\frac{dm_f}{dt} = f_i\dot{m}_{f,i} - f_c\dot{m}_{r,i} + f_e\dot{m}_{r,e} - f_c\dot{m}_{f,e} \tag{175}$$

Considering that there is no smoke in the intake manifold, but smoke only in the exhaust manifold, $f_i = 0$ [-] and $f_e = 1$ [-].
$\dot{m}_{f,j}$ [kg/s] and $\dot{m}_{r,j}$ [kg/s] represent the mass flow (in the logical order of the process, i.e. from intake manifold to cylinder and from inside the cylinder to exhaust) and reflow (the opposite) respectively, and

[14]Found on http://recoveryvehicles.tpub.com/TM-5-4240-501-14P/css/TM-5-4240-501-14P_277.htm, 18/04/2016

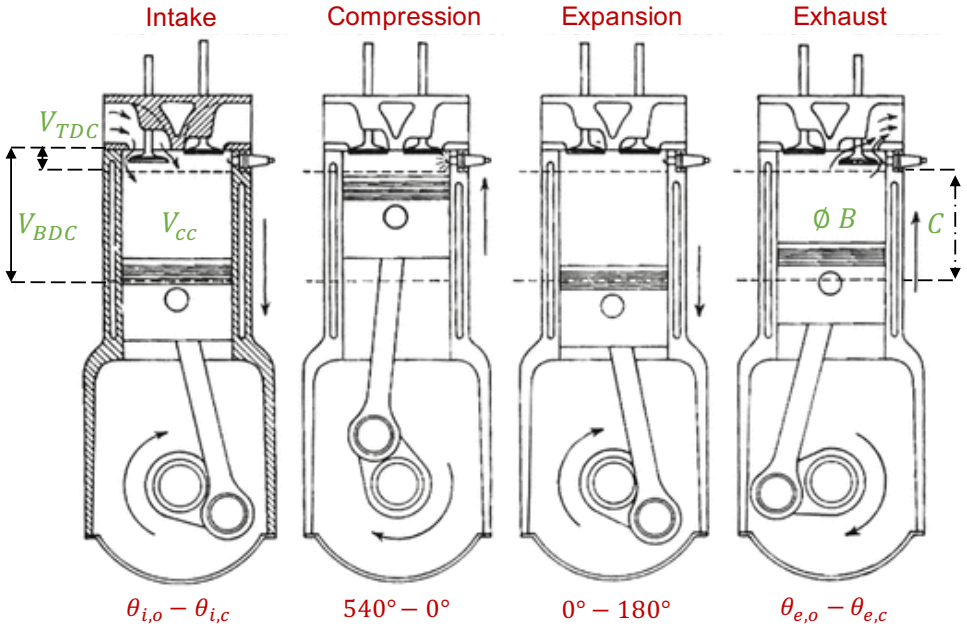

Figure 116: 4-Stroke ICE schematics

are obviously equal to 0 [kg/s] if valve j is closed.
Moreover, during admission, i.e. between $\theta_{i,o}$ and $\theta_{i,c}$:

$$\text{if } p_{in} \geq p_c \quad \begin{cases} \dot{m}_{f,i} = (165) \text{ of air-fuel with } p_{nt} = p_c,\ p_i = p_{in} \\ \dot{m}_{r,i} = 0 \end{cases} \tag{176}$$

$$\text{else} \quad \begin{cases} \dot{m}_{r,i} = (165) \text{ of cylinder mix with } p_{nt} = p_{in},\ p_i = p_c \\ \dot{m}_{f,i} = 0 \end{cases} \tag{177}$$

And during exhaust, i.e. between $\theta_{e,o}$ and $\theta_{e,c}$:

$$\text{if } p_c \geq p_{ex} \quad \begin{cases} \dot{m}_{f,e} = (165) \text{ of cylinder mix with } p_{nt} = p_{ex},\ p_i = p_c \\ \dot{m}_{r,e} = 0 \end{cases} \tag{178}$$

$$\text{else} \quad \begin{cases} \dot{m}_{r,e} = (165) \text{ of smokes with } p_{nt} = p_c,\ p_i = p_{ex} \\ \dot{m}_{f,e} = 0 \end{cases} \tag{179}$$

If p_{in} [Pa] is known via (164), $p_{ex} = 110000$ [Pa] is a bit higher than atmospheric pressure due to losses in the exhaust line. Finally, if the fresh air-fuel mixture and smokes are considered as ideal gases, p_c [Pa] inside the cylinder fluctuates as:

$$p_c = \frac{m_c\, R_c\, T_c}{V_c} \tag{180}$$

Where m_c [kg] is obviously found as an integration of (174). V_c [m^3] is the available volume in the cylinder which varies with rotation of the crankshaft [22]:

$$V_c(\theta) = \frac{V_{cc}}{2}\left(1 - \cos(\theta) + \beta - \sqrt{\beta^2 - \sin(\theta)^2} + \frac{2}{\tau - 1}\right) \tag{181}$$

With β [-], the ratio between rod length and the crank radius (i.e. half of the stroke's length), is taken at approximately 3 [-] to obtain a piston movement in the cylinder apparently uniformly accelerated.
The compression ratio $\tau = V_{BDC}/V_{TDC}$ [-] is here limited to 11 even though it maximizes efficiency. Indeed, higher ratios require several adjustments such as VVT, ignition timing delaying systems and high octane leaded gas to prevent knock (which would not be observable in this work as flame propagation is

not simulated).

The temperature T_c [K] inside the cylinder is still missing for computation of (180). For the assumed ideal gases mix:

$$c_{p,c} = f_c c_{p,f} + (1 - f_c) c_{p,a} \qquad c_{v,c} = f_c c_{v,f} + (1 - f_c) c_{v,a} \tag{182}$$

$$R_c = c_{p,c} - c_{v,c} \qquad \gamma_c = \frac{c_{p,c}}{c_{v,c}} \tag{183}$$

T_c [K] finally is computed via the differential equation:

$$\frac{dT_c}{dt} = \frac{\frac{dU_c}{dt} - \frac{dm_c}{dt} c_{v,c} T_c}{c_{v,c} m_c} \tag{184}$$

Where:

$$\frac{dU_c}{dt} = -p_c \frac{dV_c}{dt} + \dot{m}_{f,i} H_{in} - \dot{m}_{r,i} H_c + \dot{m}_{r,e} H_{ex} - \dot{m}_{f,e} H_c \tag{185}$$

Gives the variation of internal energy U_c [J], with $H_{in} = c_{p,a} T_{in}$ [J/kg] the enthalpy of the air-fuel mixture in the intake manifold (where $T_{in} \approx 300$ [K]), $H_{ex} = c_{p,f} T_{ex}$ [J/kg] the enthalpy of the smokes in the exhaust manifold ($T_{ex} \approx 1000$ [K] even though it is generally not cooled to prevent sulfuric acid condensation), and $H_c = c_{p,c} T_c$ [J/kg] the enthalpy of the ideal gas mixture in the cylinder.

All in all, this procedure allows to compute m_{mix} as the total mass of air mixture penetrated inside the cylinder at inlet valve closure $\theta_{i,c}$:

$$m_{mix} = (1 - f_c(\theta_{i,c})) m_c(\theta_{i,c}) \tag{186}$$

Of which a quantity m_ϕ [kg] is pure fuel:

$$m_\phi = \frac{m_{mix}}{1 + m_{a,1}/\phi} \tag{187}$$

$m_{a,1} = 14.7$ [$\mathrm{kg}_{air}/\mathrm{kg}_{CH_{1.8}}$] designating the ratio of air quantity regarding the fuel mass for stoichiometric combustion.

B.2 Compression and Expansion Strokes

In order to complete equation (75), there is still a need of a clear definition for the internal thermodynamic efficiency η_{ti} [-] which gives the transformation yield between thermal energy Q [J] and mechanical work W_m [Nm] or [J]:

$$\eta_{ti} \triangleq \frac{W_m}{Q} \tag{188}$$

The ICE being a volumetric machine, its mechanical work is expressed as:

$$W_m = \int_{0^\circ}^{180^\circ} p_c \, dV_c - \int_{540^\circ}^{0^\circ} p_c \, dV_c \tag{189}$$

W_m [Nm] being positive in expansion and negative in compression. The expansion work is obviously greater due to ignition of the air-fuel mixture contained in the cylinder.
The evolution of the pressure p_c [Pa] inside the cylinder is described as a function of the crank angle θ [°] [20]:

$$\frac{d\tilde{p}}{d\theta} = -\gamma_c \frac{\tilde{p}}{\tilde{V}} \frac{\mathrm{d}\tilde{\mathrm{V}}}{\mathrm{d}\theta} + \left(\frac{\gamma_c - 1}{\tilde{V}} \right) \left(\tilde{Q} \frac{\mathrm{d}\chi}{\mathrm{d}\theta} - \tilde{h} \left(1 + \varpi \tilde{V} \right) \left(\tilde{T} - \tilde{T}_{wall} \right) \right) \tag{190}$$

Where pressure p_c [Pa], volume V_c [m^3], temperature T_c and thermal energy Q have been adimensionalised according to their values at the beginning of intake:

$$\tilde{p} = \frac{p_c}{p_{in}} \qquad \tilde{V} = \frac{V_c}{V_{BDC}} \qquad \tilde{T} = \tilde{p}\,\tilde{V} = \frac{T_c}{T_{in}} \qquad \tilde{Q} = \frac{Q}{p_{in}\,V_{TDC}} \tag{191}$$

For which it is to be recalled that the volume at bottom dead center $V_{BDC} = V_{cc}\frac{\tau}{\tau-1} = \tau V_{TDC}$ [m^3] (see Figure 116).
$\frac{d\tilde{V}}{d\theta}$ [m^3/°] can easily be derived from formula (181).

The thermal exchange in separated in two parts: combustion and parietal exchange.

Combustion

Combustion is described by its progress χ [-]:

$$\chi(\theta) = \frac{1}{2}\left(1 - \cos\left(\pi\frac{\theta-\theta_s}{\theta_b}\right)\right) \qquad \frac{d\chi}{d\theta} = \frac{\pi}{2\theta_b}\sin\left(\pi\frac{\theta-\theta_s}{\theta_b}\right) \tag{192}$$

θ_s [°] designates the ignition timing, an optimization parameter possibly depending on the rotational speed ω_t [rad/s]. θ_b [°] is the angular duration of the combustion process. According to [32], and assuming a similar variation of pressure p_c [Pa] and temperature T_c [K] at all ω_t, without any aerodynamic perturbation from the piston, the flame velocity should be the same, and the time $t_b = 0.002$ [s] duration of the combustion conserved. In that case:

$$\theta_b = \omega_t\ t_b\ \cdot\ \frac{180}{\pi} \tag{193}$$

Parietal Exchange

Parietal exchange is expressed as a convective exchange of which adimensional coefficient $\tilde{h}$ is given by Woschni correlation (194):

$$\tilde{h} = \frac{h_w\ T_{in}(A_{TDC} - 4V_{TDC}/B)}{p_{in}\ V_{BDC}\ \omega_t} = \frac{h_w\ T_{in}\ \left(2\frac{\pi\ B^2}{4}\right)}{p_{in}\ V_{BDC}\ \omega_t} = \frac{2h_w\ T_{in}}{p_{in}\ \omega_t}\ \frac{\tau-1}{2\tau\ C} \tag{194}$$

Where h_w [W/(m^2 · K)] is determined empirically:

$$h_w = 129.8\ p_c^{0.8}\ B^{-0.2}T_c^{-0.55}\left(C_1\ u + C_2\ \frac{V_{cc}\ T_{in}}{p_{in}\ V_{BDC}}\ (p_c - p_m)\right)^{0.8} \tag{195}$$

In this expression, $u = 4\pi\omega_t\ C$ [m/s] designates the lineic speed of the piston, $C_1 = 2.28$ [-] while $C_2 = 0$ [-] in compression and $C_2 = 3.24 \cdot 10^{-3}$ in expansion. p_m [Pa] is the so-called *motoring* pression, obtained without combustion, and thus accompanied by a lighter parietal transfer, only due to the fluid compression:

$$\frac{dp_m}{d\theta} = -\gamma_c\frac{p_m}{\tilde{V}}\frac{d\tilde{V}}{d\theta} - \left(\frac{\gamma_c - 1}{\tilde{V}}\right)\left(\tilde{h}\left(1 + \beta\tilde{V}\right)\left(p_m\tilde{V} - \tilde{T}_{wall}\right)\right) \tag{196}$$

At last, in order to characterize the exchange surface, parameter ϖ [-] is introduced:

$$\varpi = \frac{4V_{BDC}}{B(A_{TDC} - 4V_{TDC}/B)} = \frac{4V_{BDC}}{B\ \left(2\frac{\pi\ B^2}{4}\right)} = \frac{4V_{BDC}}{2B\ V_{cc}/C} = 2\ \frac{\tau}{\tau-1}\ \frac{C}{B} \tag{197}$$

And assuming that the cylinders' walls are perfectly cooled, $\tilde{T}_{wall} = 1.3$, so that $T_{wall} = \tilde{T}_{wall}T_{in} = 390$ [K] at all time.

Bibliography

[1] J.-C. SAMIN and P. FISETTE, *Symbolic Modeling of Multibody Systems*. Dordrecht: Kluwer Academic Publishers, 2003.

[2] S. ONORI, L. SERRAO, and G. RIZZONI, "Adaptative equivalent consumption minimization strategy for hybrid electric vehicle," *ASME 2010 Dynamic Systems and Control Conference*, September 2010.

[3] Y. WANG, C. ZHANG, and Z. CHEN, "A method for state-of-charge estimation of li-ion batteries based on multi-model switching strategy," *Applied Energy*, vol. 137, pp. 427–434, January 2015.

[4] J. Y. WONG, *Theory of Ground Vehicles*. John Wiley & Sons, Inc., 3rd ed., 2001.

[5] A. VERLE and P. FISETTE, "A dynamic-based approach for road vehicle design: Application to a three-wheeler," *ECCOMAS Thematic Conference on Multibody Dynamics*, June 2015.

[6] K. KAMIEV, J. MONTONEN, M. PRABHAKARAN RAGAVENDRA, J. PYRHONEN, J. A. TAPIA, and M. NIEMELA, "Design principles of permanent magnet synchronous machines for parallel hybrid or traction applications," *IEEE Transactions on Industrial Electronics*, vol. 60, November 2013.

[7] M. EHSANI, Y. GAO, and A. EMADI, *Modern Electric, Hybrid Electric, and Fuel Cell Vehicles: Fundamentals, Theory, and Design*. Power Electronics and Applications Series, CRC Press, 2nd ed., September 2009.

[8] J. C. LIVENGOOD and J. D. STANITZ, *The Effect of Inlet-Valve Design, Size, and Lift on the Air Capacity and Output of a Four-Stroke Engine*. Washington, DC, United States: National Advisory Committee for Aeronautics, November 1943.

[9] P. DUYSINX, *MECA0492 - Vehicle Dynamics*. Sustainable Automotive Technologies, Université de Liège, 2015.

[10] K. YAMAGUCHI, *Advancing the Hybrid System*. Electric and Hybrid Vehicle Technology, 1996.

[11] A. SCIARRETTA, M. BACK, and L. GUZZELLA, "Optimal control of parallel hybrid electric vehicles," *IEEE Transactions on Control Systems Technology*, vol. 12, May 2004.

[12] C. MUSARDO, G. RIZZONI, Y. GUEZENNEC, and S. BENEDETTO, "A-ecms: An adaptative agorithm for hybrid electric vehicle energy management," *European Journal of Control*, vol. 11, pp. 509–524, June 2005.

[13] P. DUYSINX, *MECA0494-3 - Driveline and Braking Systems*. Université de Liège, 2015.

[14] N. BRACIKOWSKI, M. HECQUET, P. BROCHET, and S. V. SHIRINSKII, "Multiphysics modeling of a permanent magnet synchronous machine by using lumped models," *IEEE Transactions on Industrial Electronics*, vol. 59, June 2012.

[15] C. MI, M. A. MASRUR, and D. WENZHONG GAO, *Hybrid Electric Vehicles - Principles and Applications with Practical Perspectives*. Wiley Wiley & Sons, Ltd., 2011.

[16] E. HALL and J. BALDA, "A survey and comparison of characteristics of motor drives used in electric vehicles," *Vehicular Technology Conference, 2002. Proceedings. VTC 2002-Fall. 2002 IEEE 56th*, vol. 3, pp. 1500–1504, 2002.

[17] X. DING, M. BHATTACHARYA, and C. MI, "Simplied thermal model of pm motors in hybrid vehicle applications taking into account eddy current loss in magnets," *Journal of Asian Electric Vehicles*, vol. 8, June 2010.

[18] G. L. PLETT, "Extended kalman filtering for battery management systems of lipb-based hev battery packs - part 2. modeling and identification," *Journal of Power Sources*, vol. 134, pp. 262–276, January 2004.

[19] J. GYSELINCK, *Electrical Drives.* Variable-Speed SM and PMSM Drives, Université Libre de Bruxelles, 2015.

[20] H. JEANMART and J. MARTIN, *MECA2220 - Moteurs à Combustion Interne.* Université Catholique de Louvain, 2004.

[21] L. GUZZELLA and C. H. ONDER, *Introduction to Modeling and Control of Internal Combustion Engine Systems.* Springer, second edition ed., 2010.

[22] J. B. HEYWOOD, *Internal Combustion Engine Fundamentals.* Mechanical Engineering, McGraw Hill, 1988.

[23] MathWorks, "Modeling an automatic transmission controller."

[24] D. H. PARK, T. S. SEO, D. G. LIM, and H. B. CHO, "Theoretical investigation on automatic transmission efficiency," *Transmission and driveline systems symposium : efficiency, components, and materials*, no. 960426, pp. 49–62, 1996.

[25] D. MITRA, "Design estimation of aerodynamic angles of high speed cars," *International Journal of Engineering Science and Technology*, vol. 2(5), pp. 952–956, 2010.

[26] L. DUMAS, *Optimization and Computational Fluid Dynamics*, ch. 7, pp. 191–215. Springer, 2008.

[27] G. GENTA and L. MORELLO, *The Automotive Chassis*, vol. 2 - System Design of *Mechanical Engineering.* Springer, 2009.

[28] P. DUYSINX, *MECA0497 - Vehicle Performance.* Sustainable Automotive Technologies, Université de Liège, 2015.

[29] N. HANSEN, S. D. MULLER, and P. KOUMOUTSAKOS, "Reducing the time complexity of the derandomized evolution strategy with covariance matrix adaptation (cma-es)," *Evolutionary Computation*, vol. 11, pp. 1–18, Spring 2003.

[30] W. SCHUISKY, *Design of Electrical Machines (Berechnung Elektrischer Maschinen).* Springer-Verlag, 1960.

[31] P. S. KUO, "Cylinder pressure in a spark-ignition engine: A computational model," *Journal of Undergraduate Sciences*, vol. 3, pp. 141–145, Fall 1996.

[32] M. PAPALEXANDRIS and J. VANDOOREN, *MECA2160 - Combustibles et Combustion.* Université Catholique de Louvain, September 2007.

Rue Archimède, 1 bte L6.11.01
1348 Louvain-la-Neuve
Belgique

www.uclouvain.be/epl